The Dissertation Committee for Nicholas Aaron Estep Certifies that this is the approved version of the following dissertation:

New Frontiers in Microwave Metamaterials: *Magnetic-Free Non-Reciprocal Devices Based on Angular-Momentum-Biasing and Negative-Index Metawaveguides*

Committee:

Andrea Alù, Supervisor

Ranjit Gharpurey

Hao Ling

Gennady Shvets

Zheng Wang

New Frontiers in Microwave Metamaterials: *Magnetic-Free Non-Reciprocal Devices Based on Angular-Momentum-Biasing and Negative-Index Metawaveguides*

by

Nicholas Aaron Estep, BSEE; MSEE

Dissertation

Presented to the Faculty of the Graduate School of

The University of Texas at Austin

in Partial Fulfillment

of the Requirements

for the Degree of

Doctor of Philosophy

The University of Texas at Austin

August 2015

Dedication

To my wife, Suzanne, and our baby girl, Norah.

New Frontiers in Microwave Metamaterials: *Magnetic-Free Non-Reciprocal Devices Based on Angular-Momentum-Biasing and Negative-Index Metawaveguides*

Nicholas Aaron Estep, Ph.D.

The University of Texas at Austin, 2015

Supervisor: Andrea Alù

In this work, metamaterial concepts are applied to improve the design and realization of microwave components of a new generation. Conventional radiation sources, despite the mature and efficient development over the past century, maintain fundamental limitations. Slow-wave structures, such as backward-wave oscillators and traveling-wave tubes, function on the order of several operational wavelengths, leading to bulky architectures. Cherenkov radiation-based detectors are constrained to forward propagation, where the detection or diagnostic scheme may be damaged by energetic particles. Metamaterial concepts, specifically negative-index structures, provide new opportunities for these applications. In this context, we developed a detailed design of a negative-index metamaterial conducive to microwave generation. We experimentally validated a negative-index waveguide based on patterned plates of complementary split ring resonators. The design is conducive to interaction between particles and waves; it maintains a scalable negative-index band along with a longitudinal electric field

component for particle interaction. The sub-wavelength resonant nature of the metamaterial allows for a compact design.

In a different field of research, there is also significant need to squeeze the dimensions of microwave components. We have developed magnet-less, non-reciprocal, microwave circulators based on angular-momentum-biasing, which allow the realization of non-reciprocal devices that do not require magnets, and therefore lead to cheaper, lighter and significantly smaller devices. Angular-momentum-biasing, theoretically proposed recently in our research group, effectively mimics the collective alignment of electron spins seen in a ferromagnetic medium under a magnetic bias. Through spatio-temporal modulation, one can generate electrical rotation, leading to strong non-reciprocal response without magnetism. We have experimentally proven the theory on lumped element circulators and proposed transmission-line variations, providing over 50 dB of isolation in a range of frequency bands. This method provides efficient, easily tunable, fully integrable, compact devices that may revolutionize the future of integrated components. We have developed rigorous design principles that not only provide guidance for designs based on desired performance metrics, but also proves the passive nature of the concept. Furthermore, we have crafted mechanisms to enhance the bandwidth performance and improve linearity.

Table of Contents

List of Tables

List of Figures

Chapter 1 Introduction

The research presented in this work applies metamaterial concepts to address two crucial requirements in microwave systems: non-reciprocity and radiation generation and detection. The advancements in both categories will be developed and presented in the following sections.

1.1 Negative-Index Metamaterials For Coherent Radiation Generation

All naturally occurring dielectrics can be categorized as positive-index materials, in which the phase and the group velocity of a propagating wave are parallel. Negative-index (NI) materials are constructed from arrays of specially designed inclusions, permitting the manipulation of electromagnetic wave propagation. Of particular interest are the potential applications for reverse Cherenkov radiation (RCR), where highly energetic particles interact with a NI media. Unique prospects in wave-particle applications, such as coherent wave generation and detection, are grounded on a foundation of NI operation.

In the past decade, researchers have successfully proposed and realized negative-index propagation in a variety of composite materials loaded with periodic artificial inclusions [1]-[4]. NI structures, also known as left-handed materials (LHMs), are characterized by opposing vectors for phase and group velocity [5]. These metamaterials provide the opportunity for innovative applications for which conventional materials fail, such as the realization of super-resolving lenses, highly efficient antennas, and cloaking [6]-[10]. Examples and an illustration of NI media is shown in Fig. 1.

A common approach to realizing these metamaterials consists of embedding shunt wire elements and split-ring resonators (SRRs), that have been shown to provide bulk, homogenizable media with a NI band [1],[11]. NI behavior has also been achieved by loading conventional waveguides with resonant apertures, providing a natural transition for integration with microwave waveguide components [12],[13].

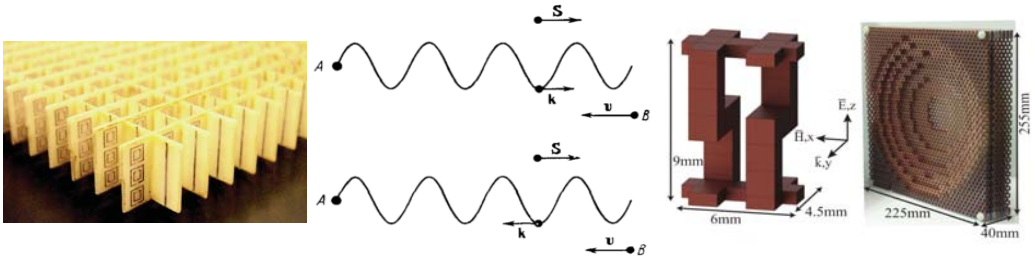

(*a*) (*b*) (*c*)

Figure 1: Negative index structures and phenomenon. (a) Bulk metamaterial from [1], (b) illustration of anti-parallel vectors for phase (*k*) and power (*S*) in NI medium [5], and (c) NI lens from [7].

The interaction of electron beams and electromagnetic waves plays a pivotal role in microwave generation and radiation detection. Compared to conventional materials, NI metamaterials provide interesting opportunities in this field: for microwave generation, NI materials can provide the necessary resonance far below the diffraction limit, for sizes much smaller than the operating wavelength, allowing for compact designs [14]. In addition, a charged particle moving through an NI medium experiences RCR, where the group velocity of the emitted electromagnetic wave and the velocity of the beam are in opposite directions [15]. For radiation detection purposes, an RCR detection scheme could reduce sensor damage caused by the radiation source. The backward wave

propagation allows the detector to be placed outside the radiation region, which is ideal for accelerator diagnostics. This condition is also attainable in periodically loaded structures supporting backward modes, but bulk metamaterials may provide unique opportunities for stronger interaction and a more compact integration.

A few constraints should be considered to maximize the e-beam interaction with an optimal NI metamaterial design. First, interaction between the beam and the metamaterial is achieved when the beam line and electromagnetic mode dispersion diagrams intersect. Additionally, the presence of a longitudinal electric field component in the guided mode is necessary for acceleration or deceleration of a non-undulating beam. Conventional NI designs based on quasi-TEM field patterns, such as loaded microstrip lines (i.e., [16]), fail to adhere with this requirement. Furthermore, an open, unimpeded path is necessary to allow an electron beam to propagate through the NI material freely, which is not achieved in many NI designs, such as fishnet periodic structures [17]. Finally, the use of planar technologies is usually preferred due to ease of fabrication, cost effectiveness and scalability.

In this work, we consider a negative-index metawaveguide (NIMW) design consisting of an infinite stack of conducting parallel plates loaded by etched-out complementary split-ring resonators (CSRRs), as originally proposed in [18], ideal for RCR applications. This structure supports a transverse magnetic (TM) NI mode with a strong longitudinal component of the electric field in the middle plane between neighboring parallel plates. In contrast to more conventional SRR-based metamaterials, which interact with the magnetic field in the transverse direction, CSRRs strongly interact with the transverse component of the electric field [16]-[19]. In the NI band,

therefore, the CSRRs' resonance leads to an effective negative permittivity ($\mathrm{Re}\{\varepsilon_{eff}\}<0$). The negative permeability ($\mathrm{Re}\{\mu_{eff}\}<0$) of the NIMW originates from the confinement of the TM mode below the cutoff frequency of the parallel plate waveguide [20], leading to the opportunity of combining negative-index propagation with longitudinal electric fields.

Although the NIMW is a promising design for RCR applications, there are some limitations that must be addressed. The considered design supports other (undesired) propagation modes in the same frequency band, leading to challenges in mode excitation. We will show that a properly tailored excitation is able to excite only the TM NI mode of interest. In addition, one potentially undesired effect of utilizing SRRs or CSRRs is their inherent bi-anisotropy [21],[22], which translates into magneto-electric effective constitutive parameters. Due to these bi-anisotropic properties, the NIMW characteristic impedance is complex and it depends on the direction of propagation [18], which may be a drawback in terms of proper matching with free-space or a feeding circuit.

A thorough analysis of the NIMW is provided, to include modal analysis, homogenization, scattering, and excitation. In addition, a transmission-line (TL) model is introduced to accurately predict the dispersion and impedance of the proposed metamaterial. Furthermore, a simplified NIMW structure was fabricated in order to validate the characteristics of the design. Finally, a tangible, finite NIMW tailored for electron beam coupling is simulated and source output parameters are provided.

1.2 Achieving Non-Reciprocity without Magnets

In order to realize non-reciprocity, a crucial task in electronic and optical applications, one must break time-reversal symmetry. Non-reciprocal devices play a

pivotal role in communication systems, from protecting coherent source generators from reflected signals, to cancelling cross talk between transmit and receive signal paths in antenna feeding networks [23]. Mobile communication protocols are constrained by the availability of non-reciprocal solutions, which are currently limited to half-duplex and duplex operations, whereas full-duplex modes would be highly desirable [24]. As seen in Fig. 2 (a) and (b), half-duplex operation must switch between transmit and receive mode, whereas duplex mode requires separate bands for transmit and receive signals. However, full-duplex (Fig. 2(c)) mode allows for simultaneous transmit receive operation, thus enhancing the available bandwidth. In order to enable full-duplex systems, one must find a compact, cost effective means of breaking time-reversal symmetry, and thus reciprocity.

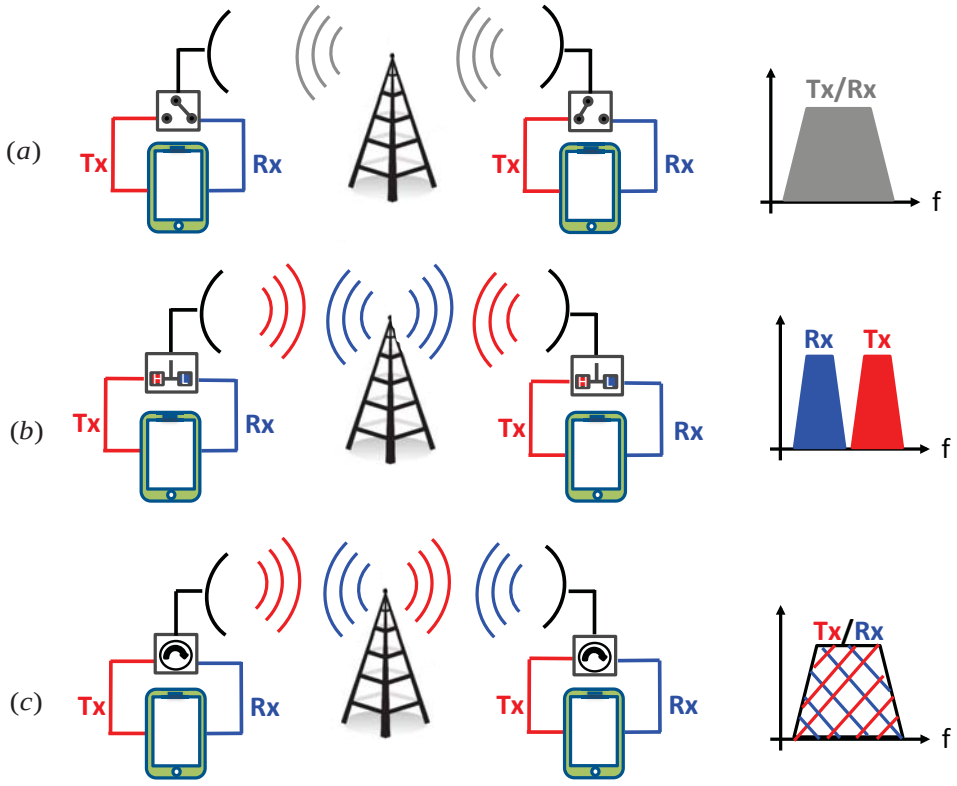

Figure 2: Enhancing two-way communication channels. (a) Half-duplex mode – must switch between transmit and receive mode. (b) Duplex mode – separate transmit and receive channels. (c) Full-duplex mode – Simultaneous transmit and receive, at same frequency band.

Onsager-Casimir's principle on reciprocity states that, in order to break the reciprocity of a linear system, it is necessary to bias it with a quantity that is odd-symmetric under time reversal [25]-[27]. Four quantities are known to satisfy this requirement: the magnetic field, the electric current, the linear momentum and the angular momentum.

For decades, the most common approach consisted in applying external magnetic fields to ferromagnetic media [23],[28]. In the absence of a magnetic field, electron spins in such materials are oriented in random directions and therefore the net magnetic activity is negligible. However, when biased with a static magnetic field [Fig. 3(a)], electron spins are aligned in the same direction (the direction of the magnetic bias) and are forced to rotate more easily (with less energy) in a particular direction [29]. As a result, circularly-polarized electromagnetic waves with opposite rotation directions interact differently with such media, and time-reversal symmetry (reciprocity) is broken. Magnetic biasing may provide a well-established means to break reciprocity, but contains innate limitations: the required ferromagnetic materials are unsuitable for complementary meta-oxide-semiconductor (CMOS) processing, since their lattice is incompatible with the lattice of metals and semiconductors, and they are based on external biasing devices, which increase size and weight. For these reasons, to date there has been little success in integrating magnetic-based devices. On the other hand, the integration of non-reciprocal devices is of tremendous importance, since it may eventually allow the realization of full-duplex communication systems and enhance the speed of wireless communications networks.

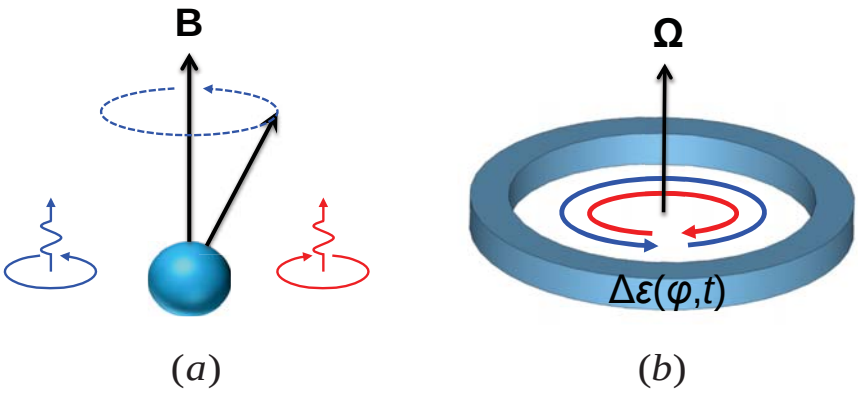

Figure 3: Non-reciprocity through biasing with (a) magnetic and (b) angular-momentum vectors [29].

Several alternatives to magnetic biasing were proposed in the past decades, the first one involving circuits with field effect transistors [30],[31]. Such approaches are fully compatible with integrated circuit (IC) technology, but they generally suffer from poor noise performance and strong non-linearity. More recently, [32]-[34] proposed a class of magnet-less non-reciprocal metamaterials based on transistor-loaded rings. Transistors force waves in the rings to travel in only one direction, thereby mimicking the electron spin precession in magnetized ferrites. These works were successful in realizing effective ferrite media, which, like real ferrites, can produce Faraday rotation or be used as substrates in microwave devices. However, they are also bound to the limitations related to power handling, nonlinearities, and noise sensitivity of previous transistor-based approaches. Transistor-based metamaterials were also presented in [35],[36], with similar limitations. Non-linearity was also studied as a potential path to magnet-less non-reciprocity, especially at optical frequencies [37]-[40]. However, such approaches usually

require strong input intensities and lead to significant signal distortion, in addition to being inherently dependent on the signal amplitude.

Linear, low-noise, and strong non-reciprocity can be achieved by spatiotemporal modulation of waveguides via appropriate electrical or acoustical signals, as recently discussed in [41]-[50]. However, the weak nature of electro-optical and acousto-optical effects, through which modulation can be typically achieved, leads to bulky devices, especially at optical frequencies. Furthermore, many of these works rely on a non-uniform modulation across the waveguide cross-section, significantly complicating the fabrication process.

Inspired by the Onsager-Casimir's principle and the physical mechanism that creates non-reciprocity in ferrites, Ref. [51] presented a new class of metamaterials that provide strong, low-noise, and linear non-reciprocity at the sub-wavelength scale through biasing with the angular-momentum vector. The main element of these metamaterials is a ring resonator, which, like the atoms of real materials, supports pairs of degenerate states with opposite angular momentum. Biasing the ring with the angular momentum vector lifts the degeneracy and produces non-reciprocity, much like a magnetic bias produces non-reciprocity in ferromagnetic materials (Fig. 3(b)). This concept was experimentally proven in acoustics by circulating air in a ring resonator, thereby demonstrating the first-ever acoustic circulator [52].

Since physical rotation is obviously impractical for electromagnetic devices, [51] proposed to realize effective electric rotation through appropriate spatiotemporal modulation. In particular, it was shown that the degeneracy of the l-th order modes of a ring (modes with azimuthal variation $e^{\pm il\varphi}$) can be lifted by modulating the permittivity

of the ring as $\Delta\varepsilon(\varphi,t)=\Delta\varepsilon_{\mathrm{m}}\cos(\omega_{\mathrm{m}}t-l_{\mathrm{m}}\varphi)$, where $\Delta\varepsilon_{\mathrm{m}}$, ω_{m} and $l_{\mathrm{m}}=2l$ represents the perturbation of the ring permittivity, the modulation frequency and the modulation azimuthal order, respectively. Such permittivity modulation leads to an effective rotation with angular velocity $\Omega_{\mathrm{m}}=\omega_{\mathrm{m}}/l_{\mathrm{m}}$. Contrary to the approaches of [41],[44],[45], the modulation in [51] is continuous across the transverse surface area of the ring, significantly relaxing manufacturing requirements. In addition, the use of a ring resonator significantly boosts the otherwise weak modulation effect, resulting in strong non-reciprocity at the sub-wavelength scale.

Chapter 2 Negative-Index Metawaveguide

2.1 Negative-Index Media and Reverse Cherenkov Radiation

To understand the impact of Cherenkov radiation, in particular RCR, we may develop the theory through classical electromagnetics. The flow of charged particles may be described as a charge moving along the *z* axis on the *x*-*y* plane as

$$\mathbf{J}(\mathbf{r},t)=\hat{z}qv\delta(z-vt)\delta(x)\delta(y)=\hat{z}qv\delta(z-vt)\frac{\delta(\rho)}{2\pi\rho}, \tag{2.1.1}$$

where $\delta(.)$ is the Dirac delta function. Here, a single charge, q, propagates with a velocity, v, along the z-axis. The geometry for the charged particle beam is shown in Fig. 4.

Assuming a time harmonic condition ($e^{j\omega t}$), the current may be represented in the frequency domain as

$$\mathbf{J}(\mathbf{r},\omega)=\hat{z}qv\delta(x)\delta(y)\frac{e^{-j\frac{\omega}{v}z}}{|v|}=\hat{z}\frac{qv\delta(\rho)}{2\pi\rho}\frac{e^{-j\frac{\omega}{v}z}}{|v|}. \tag{2.1.2}$$

The inhomogeneous Helmholtz wave equation for the electric vector potential is found as

$$\nabla^2\mathbf{A}(\mathbf{r},\omega)+k^2\mathbf{A}(\mathbf{r},\omega)=-\mu\mathbf{J}(\mathbf{r},\omega), \tag{2.1.3}$$

---

[53] Authors: N.A. Estep, A.N. Askarpour, S. Trendafilov, G. Shvets, and A. Alù.
Author Contributions: N.A.E. and A.N.A developed theory. N.A.E. conducted calculations, theoretical modeling, and analysis. S.T. provided guidance with simulations. G.S. advised the research and A.A. directed and supervised the work.
[65] Authors: N.A. Estep, A.N. Askarpour, and A. Alù.
Author Contributions: N.A.E. and A.N.A developed theory, N.A.E. performed the experiments and analysis, and A.A. directed and supervised the work.

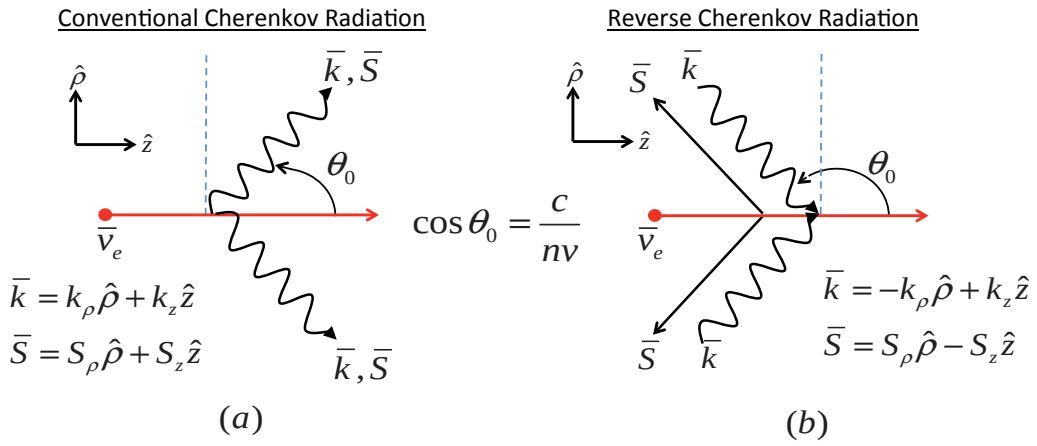

Figure 4: Cherenkov radiation for conventional and negative index media**.** When the velocity of a charged particle is greater than the phase velocity of the surrounding medium, the particle responds by emission of Cherenkov radiation. In natural material, the radiation forms a cone in the direction of the charged beam. In NI materials, the power of the radiation is outwards and away from the beam.

where ***A*** is the electric vector potential and ***J*** is the current density. Since the charge in (2.1.1) only has a *z* component, the wave equation is expressed as

$$\nabla^2 A_z(\mathbf{r},\omega) + k^2 A_z(\mathbf{r},\omega) = -\hat{z}\frac{\mu(\omega)qv\delta(\rho)}{|v|}\frac{e^{-j\frac{\omega}{v}z}}{2\pi\rho} \tag{2.1.4}$$

and further reduced to

$$\left(\nabla_t^2 + \frac{\partial^2}{\partial z^2}\right)A_z + k^2 A_z = -\frac{\mu(\omega)qv\delta(\rho)}{|v|}\frac{e^{-j\frac{\omega}{v}z}}{2\pi\rho}. \tag{2.1.5}$$

Assuming A_z in (2.1.5) is the solution of the form

$$A_z = \mu \frac{qv}{|v|} e^{-j\frac{\omega}{v}z} g(\rho), \tag{2.1.6}$$

then the partial differential equation in (2.1.5) may be solved as

$$\begin{aligned} \nabla_t^2 g(\rho) + k_\rho^2 g(\rho) &= -\frac{\delta(\rho)}{2\pi\rho} \\ k_\rho^2 &= \frac{\omega^2}{v^2}\left[\frac{n^2 v^2}{c^2} - 1\right]. \end{aligned} \tag{2.1.7}$$

The dispersion relationship is then defined as

$$k_\rho^2 = k^2 - \frac{\omega^2}{v^2} = k^2 - k_z^2. \tag{2.1.8}$$

The solution to (2.1.7) is dependent on the index of refraction, *n*, as

$$g(\rho) = \begin{cases} \frac{1}{4j} \mathrm{H}_0^{(2)}\left(k_\rho \rho\right) & n > 0 \\ \frac{-1}{4j} \mathrm{H}_0^{(1)}\left(k_\rho \rho\right) & n < 0 \end{cases}, \tag{2.1.9}$$

where the proper choice of Hankel function ensures causality. The solution to the vector potential for the represented source in (2.1.2) is of the form

$$A_z(\mathbf{r}, \omega) = \frac{qv}{|v|} \mu(\omega) g(\rho, \omega) e^{-j\omega\frac{z}{v}}. \tag{2.1.10}$$

From the electric vector potential, the magnetic field may be found by taking the curl as

$$\mathbf{H} = \frac{1}{\mu}\nabla \times \mathbf{A} = -\hat{\phi}\frac{qv}{|v|}h(\rho,\omega)e^{-j\omega\frac{z}{v}}$$
$$h(\rho) = \frac{\partial}{\partial\rho}g(\rho) = -k_\rho \begin{cases} \frac{1}{4j}\mathrm{H}_1^{(2)}(k_\rho\rho) & n > 0 \\ \frac{-1}{4j}\mathrm{H}_1^{(1)}(k_\rho\rho) & n < 0 \end{cases}. \tag{2.1.11}$$

Finally, the electric field outside the source region may be found in a similar fashion as

$$\begin{aligned}\mathbf{E} = \frac{1}{j\omega\varepsilon}\nabla \times \mathbf{H} &= -\hat{\rho}\frac{e^{-j\omega\frac{z}{v}}q}{\varepsilon(\omega)|v|}h(\rho,\omega) \\ &-\hat{z}j\omega\frac{1}{v|v|\varepsilon(\omega)}q\left[\frac{n^2v^2}{c^2}-1\right]g(\rho,\omega)e^{-j\omega\frac{z}{v}}.\end{aligned} \tag{2.1.12}$$

When only considering the z component of the electric field, its value may be found directly from the vector potential as

$$E_z = -\frac{jk_\rho^2}{\varepsilon(\omega)\mu(\omega)\omega}A_z. \tag{2.1.13}$$

It can also be seen that when the velocity of the beam is lower than the relative wave velocity in the media, k_ρ becomes entirely imaginary. This results in the evanescent form of the Hankel function, consistent with a field pattern where Cherenkov radiation is not present. The choice of *g(ρ)* in (2.1.9) provides the mathematical selection for either forward or backward Cherenkov radiation.

The Poynting vector for the induced Cherenkov radiation may be found by taking the cross product of the electric and magnetic field

$$\mathbf{S} = \frac{1}{2}\mathbf{E}\times\mathbf{H}^* = \frac{1}{2}\frac{q^2}{v\varepsilon(\omega)}\left(-j\omega\frac{1}{v}\left[\frac{n^2v^2}{c^2}-1\right]g(\rho,\omega)h^*(\rho,\omega)\hat{\rho}+\left|h(\rho,\omega)\right|^2\hat{z}\right). \quad (2.1.14)$$

In both positive and negative index media, assuming Cherenkov radiation, the k_z component of the wavenumber follows the direction of the beam propagation and k_ρ is positive or negative dependent on the selection of (2.1.9). The general condition for Cherenkov radiation and the related cone angle is found by

$$v^2 > \frac{c^2}{n^2}, \quad \cos\theta_0 = \frac{c}{nv}. \quad (2.1.15)$$

In order to further understand the relationship between the beam and the surrounding media, the above development was extended in a Matlab code. Fig. 5 shows the electric field (E_z) lines due to a single electron in a lossless, dispersion-less medium of $n = 2$. When the velocity of the electron is below the condition in (2.1.15), the Hankel term is imaginary. This is the case when a charge travels at $v = 0.4c$, as seen in Fig. 5(a). However, when the electron is moving at $v = 0.9c$, the Cherenkov condition is met, leading to conventional Cherenkov radiation, as represented by Fig. 5(b). The field profiles in Fig. 5 are for a single snapshot in time.

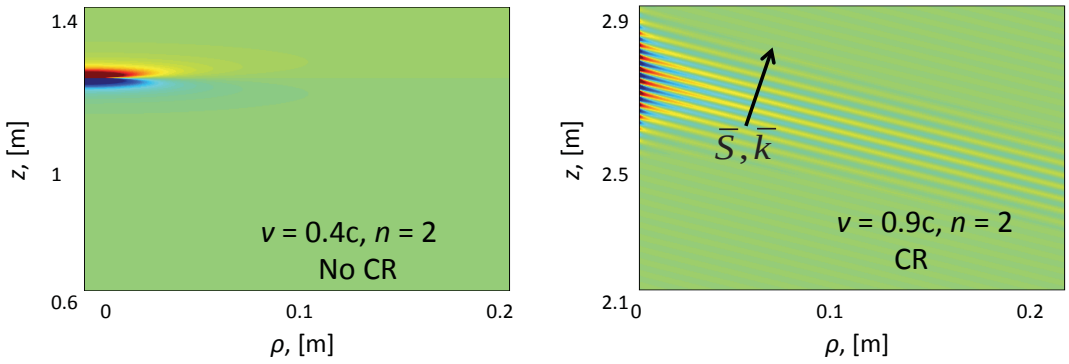

Figure 5: Tangential electric field (E_z) due to traveling electron in a conventional medium**.** Snapshot at 10 ns, with the particle at $z = 0$ for $t = 0$. The charged particle is along the z axis, with the location dependent on the relative speed. (a) Below the Cherenkov threshold, the fields due to the electron are localized and evanescent. Charge at 1.2 m at snapshot. (b) Above the limit, the electron prompts Cherenkov radiation, with the cone angle dependent on the index of refraction and the speed of the particle. Charge at 2.7 m at snapshot.

Now we consider the case when the moving electron is propagating through a NI material. Assuming Drude and Lorentz dispersion models for ε_{eff} and μ_{eff} respectively (NI band between 5.2 to 5.5 GHz), we obtain RCR for a fast moving electron of $v = 0.9c$. As shown in Fig. 6, the electromagnetic energy is flowing away from the electron in z, with the phase flowing in the opposing direction as the Poynting vector.

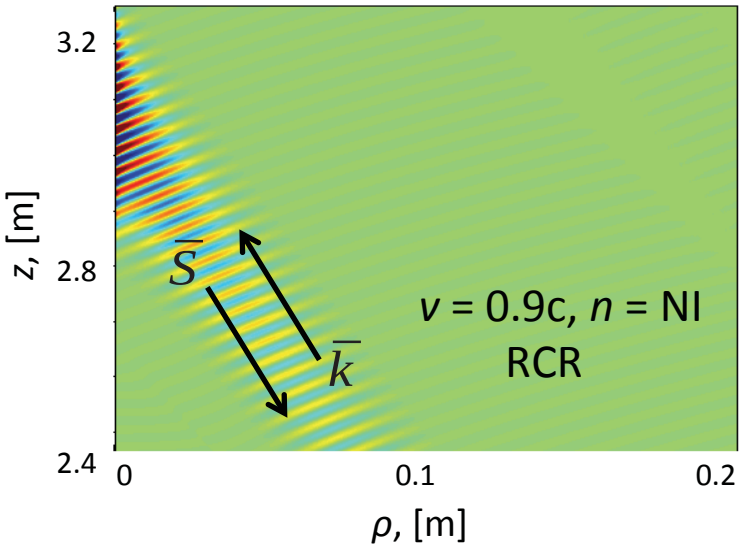

Figure 6: Tangential electric field (E_z) due to traveling electron in a dispersive, NI material**.** Snapshot at 10 ns, with the particle at $z = 0$ for $t = 0$. The charged particle is along the z axis, with the location dependent on the relative speed. The RCR leads to the electromagnetic energy power flow leading away from the electron. Charge at 2.7 m at snapshot.

The unique circumstances of RCR have implications in radiation detectors and coherent sources. Since the energy of the Cherenkov radiation is propagating away from the charged particle beam, the sensors and detection equipment may be easily shielded or positioned to avoid damage from the radiation. Additionally, the backward wave propagation may be used in a similar sense as a backward wave oscillator. The instability of the reverse travelling wave interacts with the opposing electron bunch, leading to coherent electromagnetic source. A particular metamaterial conducive for both these applications will be presented in the following section.

2.2 NIMW GEOMETRY AND MODAL SOLUTION

The geometry and unit cell of the NIMW that we consider is shown in Fig. 7(a), with geometry parameters indicated in the caption and consistent with the metamaterial originally proposed in [18]. The NIMW was simulated in CST Microwave Studio™ assuming periodic boundary conditions in all directions around the unit cell shown in Fig. 7(b) [53]. The dispersion diagram for wave propagation along the x direction is shown in Fig. 8 around the design frequency, showing that the structure supports a backward (NI) TM and a positive-index transverse electromagnetic (TEM) mode. The confinement of the TM fields and the effect of periodically loaded CSRRs result in the NI propagation band (black line) between 5.5 to 5.2 GHz ($kd \approx 0.9$): this sub-cutoff TM mode is responsible for a broad effective negative permeability, while the CSRR resonances result in a narrow negative permittivity region that opens the NI passband.

In addition to the TM NI mode, a TEM mode is found in the frequency band of interest. The TEM solution represents conventional plane-wave propagation in the empty parallel-plate waveguide, showing minimal coupling with the CSRR loads. This mode (blue line) crosses the frequency band in which the NI mode of interest is supported, and therefore should be properly considered when exciting the structure (Section 2.6). Because the two modes have different reflection symmetries with respect to the x-y plane, the modes' crossing disappears when the symmetry of the problem is reduced by introducing, for example, a finite propagation wavenumber crossing the plates $\beta z \neq 0$. We assume $\beta z = 0$, i.e., the waves propagate entirely in the x-y plane, which is the preferred condition for maximal coupling with an electron beam traveling between any two neighboring plates.

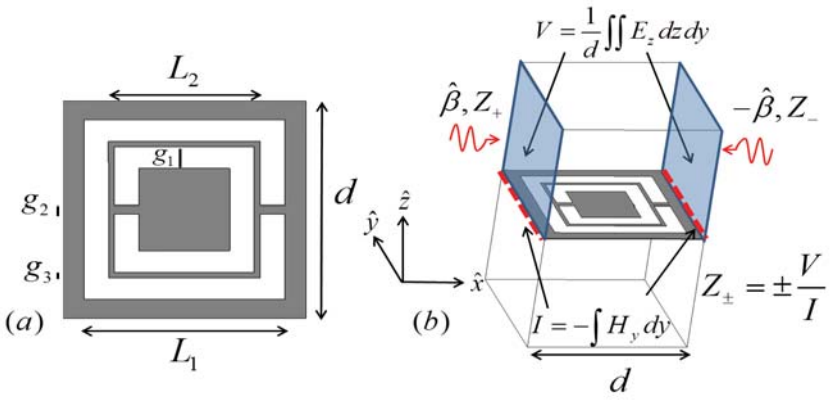

Figure 7: NIMW geometry originally proposed in [18] and further investigated in [53]: (a) CSRR inclusion and (b) unit cell in the periodic structure. The integration area for computation of the potential V and the integration path for calculation of the current I are in panel (b). The CSRR dimensions are: d = 8 mm, L_1 = 6.6 mm, L_2 = 4.6 mm, g_1 = 0.8 mm, g_2 = 0.3 mm, and g_3 = 0.2 mm. Plate thickness (t) is 0.05 mm and cell height (h) is 12.8mm.

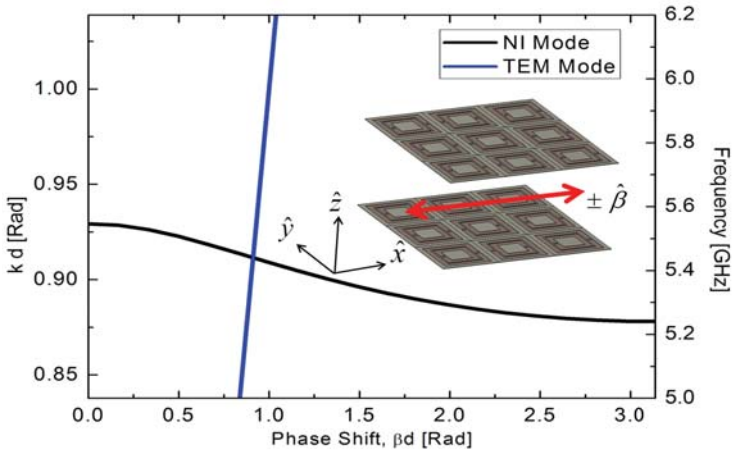

Figure 8: NIMW dispersion diagram for the metamaterial geometry of Fig.7, obtained using full-wave simulations, for propagation along x. In addition to the TM NI mode, a TEM mode is supported within the same frequency band. The inset is a rendering of the NIMW geometry, which is infinitely periodic in all directions [53].

Fig. 9 shows the transverse electric and magnetic field amplitude and phase for the NI mode propagating along x on the plane $x = -d/2$ (highlighted in the inset) for $\beta_x d = \pi/4$. As seen in the contour plots, both transverse electric and magnetic field distributions are odd functions of z and even functions of y. The amplitudes increase near the CSRR plate, confirming strong field interaction with the resonator within the NI band.

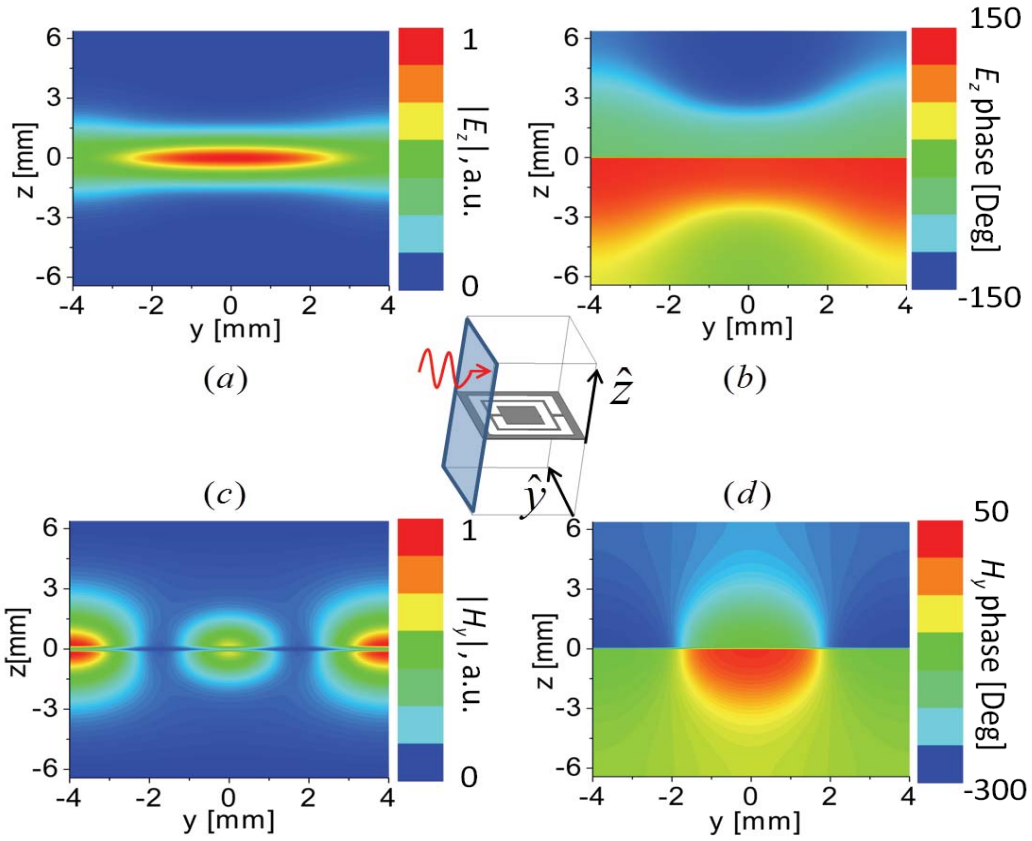

Figure 9: Field distribution for the TM NI mode propagating along x, for $\beta_x d = \pi/4$. Transverse electric field E_z (a) magnitude and (b) phase at the entrance plane of the unit cell of Fig. 7, for forward (x = -d/2) propagating modes. Corresponding transverse magnetic field H_y (c) magnitude and (d) phase. The phases are unwrapped for smooth visualization [53].

Next, we investigate the dependence of the modal dispersion on the angle of propagation inside the metamaterial, by sweeping the angle of propagation in the *x*-*y* plane. The corresponding iso-frequency contours ($\omega(\beta_x,\beta_y)$ = constant) are shown in Fig. 10. A completely isotropic structure would produce perfect circles, but the inherent asymmetries in the CSRR NIMW produce an anisotropic response, despite the long wavelength regime we are operating in [19].

By analyzing the gradients of the dispersion diagram (arrows in Fig. 10), we can compute the group velocity components $v_{x,y}^{g} = \delta\omega / \delta\beta_{x,y}$ and we conclude that the structure supports backward-wave NI propagation for all directions in the *x*-*y* plane. It is possible to improve the isotropy of the response in various ways: in the following, we show that proper optimization may shift down the frequency of operation for a fixed period (Section 2.5, which makes the array granularity effectively smaller and the response more isotropic. Also, we have explored the possibility to rotate the CSRRs in superlattices to improve the array symmetry, which indeed improves the overall isotropy. This however comes at the price of an overall reduced bandwidth.

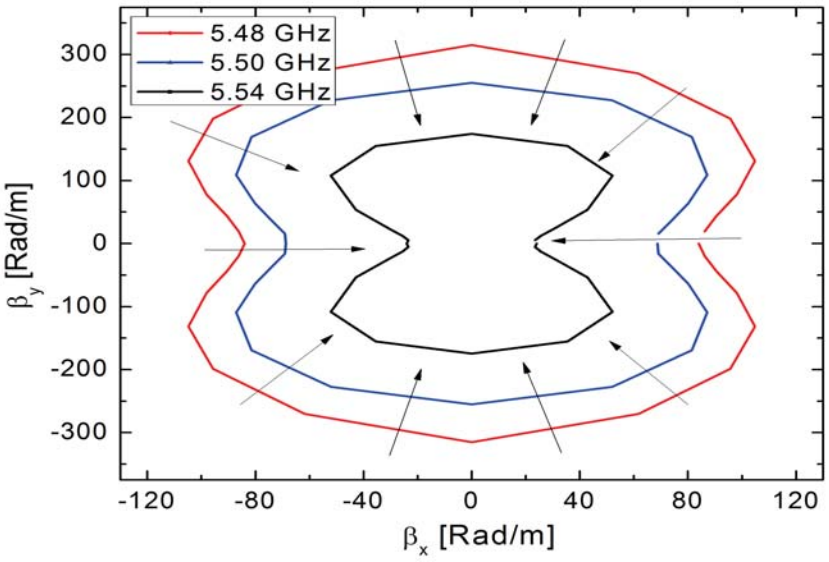

Figure 10: Iso-frequency contours for the NIMW design of Fig. 7. The contours show the values of propagation constant for different neighboring frequencies in the NI band [53].

2.3 HOMOGENIZATION AND TRANSMISSION-LINE THEORY

Assuming a general bi-anisotropic form for the homogenized constitutive relations of this metamaterial, we use Tellegen's formalism to relate electric **E** and magnetic **H** fields to the electric and magnetic flux densities (**D**, **B**):

$$\mathbf{D} = \underline{\underline{\varepsilon}} \cdot \mathbf{E} + \underline{\underline{\xi}} \cdot \mathbf{H}, \qquad \mathbf{B} = \underline{\underline{\mu}} \cdot \mathbf{H} + \underline{\underline{\zeta}} \cdot \mathbf{E} \tag{2.3.1}$$

where the four constitutive tensors fully describe the wave interaction with the periodic array. The effective permittivity ε and permeability μ tensors take into account the electric and magnetic response of the structure, whereas the coupling tensors (ξ, ζ) describe the magneto-electric coupling. For TM propagation in the x direction, the field

vectors have relevant components $\mathbf{E} = \hat{x}E_x + \hat{z}E_z, \mathbf{H} = \hat{y}H_y$. The CSRR magneto-electric coupling for CSRRs oriented as in Fig. 7(b) is generated between the transverse components $\hat{z}E_z$, $\hat{y}H_y$ as shown in Fig. 10, and therefore (2.3.1) can be written in scalar form as

$$D_z = \varepsilon_0 \varepsilon_{eff} E_z + \frac{j\xi_0}{c} H_y, \qquad B_y = \mu_0 \mu_{eff} H_y - \frac{j\xi_0}{c} E_z, \tag{2.3.2}$$

with ξ_0 and c representing the magneto-electric coupling constant and the speed of light in free space, respectively, while ε_{eff}, μ_{eff} are the components (ε_{zz}, μ_{yy}) of the effective constitutive tensors. Helmholtz's wave equation in such material yields

$$E_z \left(\beta_x^2 - \frac{\omega^2}{c^2} \left(\varepsilon_{eff} \mu_{eff} - \xi_0^2 \right) \right) = 0, \tag{2.3.3}$$

where the propagation constant β_x and corresponding index of refraction n are found as

$$\beta_x = \pm \frac{\omega}{c} \sqrt{\varepsilon_{eff} \mu_{eff} - \xi_0^2}, \qquad n = \pm \sqrt{\varepsilon_{eff} \mu_{eff} - \xi_0^2}. \tag{2.3.4}$$

For passive materials, the proper root selection in (2.3.4) is $\mathrm{Im}\{n\}<0$.

The corresponding characteristic impedance, defined as the ratio of transverse electric and magnetic eigen-modal fields, depends on the propagation direction, as expected for bi-anisotropic materials [22],[53],[54]:

$$Z_{\pm} = \frac{\mu_{eff} \eta_o}{(n \pm j\xi_0)} \tag{2.3.5}$$

where $\eta_o = \sqrt{\mu_o/\varepsilon_o}$ is the free-space impedance and the plus and minus signs indicate propagation along the positive and negative *x*-axis, respectively. This form of bi-anisotropy, caused by the inclusion asymmetry, is typically undesirable, as it makes the design, modeling and impedance matching of the metamaterial more challenging.

We may evaluate the characteristic impedance by averaging the fields in the modal solution shown in Fig. 9. As discussed in [18], and schematically depicted in Fig. 7(b), the effective voltage and current for the NIMW may be evaluated as

$$V = \frac{1}{d}\int_{-d/2}^{d/2}\int_{t/2}^{h/2} E_z \, dz dy, \quad I = -\int_{-d/2}^{d/2} H_y \, dy. \tag{2.3.6}$$

The first integral is taken on a plane normal to the direction of propagation covering the upper half of a unit cell in the transverse direction. Since the NI mode is odd about *z*, we only integrate over half the plane of the unit cell. The second integral is defined over a line in the *y* direction just above the metal plate. Voltage and current integration domains are shown in Fig. 7(b). The transverse plane is selected based on the direction of propagation ($x = -d/2$ for Z_+ and $x = +d/2$ for Z_-). The calculated impedance, defined as the ratio *V/I*, is a function of the phase shift $\beta_x d$ in the NI band. The real (blue line) and imaginary (red line) terms for the complex impedance for forward propagation, as extracted from our simulations, are shown in Fig. 11. For reciprocal periodic media, Z_+ and Z_- form a complex conjugate pair (not shown in the figure) and, in the absence of bi-anisotropy and assuming lossless inclusions, they become equal and purely real, i.e., the imaginary part of *Z* would disappear.

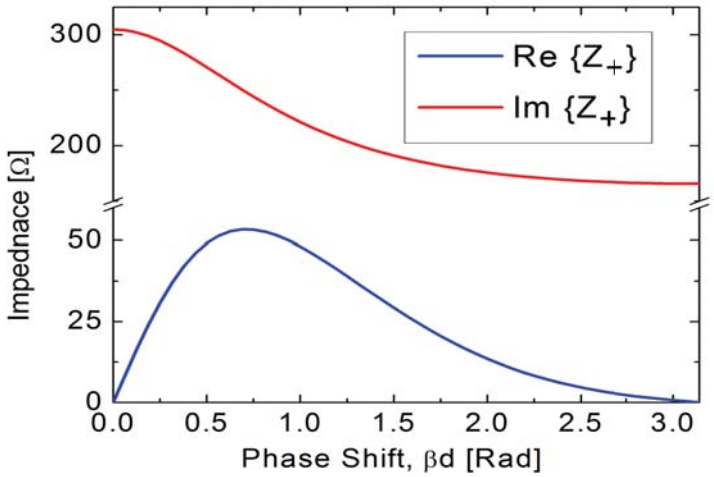

Figure 11: Effective impedance (Z_+) for the CSRR design of Fig. 7. The forward and backward wave impedances are conjugate matched to each other, showing the bi-anisotropic nature of the metamaterial under analysis [53].

By combining (2.3.4) and (2.3.5), we can define the relevant constitutive parameters of the metamaterial as a function of its secondary parameters β_x and $Z_\pm$:

$$\begin{aligned}
\varepsilon_{eff} &= \frac{2n}{Z_+ + Z_-}\eta_o = \frac{c\beta_x}{\omega}\frac{2}{Z_+ + Z_-}\eta_o \\
\mu_{eff} &= \frac{2\,n\,Z_+Z_-}{Z_+ + Z_-}\frac{1}{\eta_o} = \frac{c\beta_x}{\omega}\frac{2\,Z_+Z_-}{Z_+ + Z_-}\frac{1}{\eta_o} \\
\xi_0 &= -jn\frac{Z_+ - Z_-}{Z_+ + Z_-} = -j\frac{c\beta_x}{\omega}\frac{Z_+ - Z_-}{Z_+ + Z_-}.
\end{aligned} \tag{2.3.7}$$

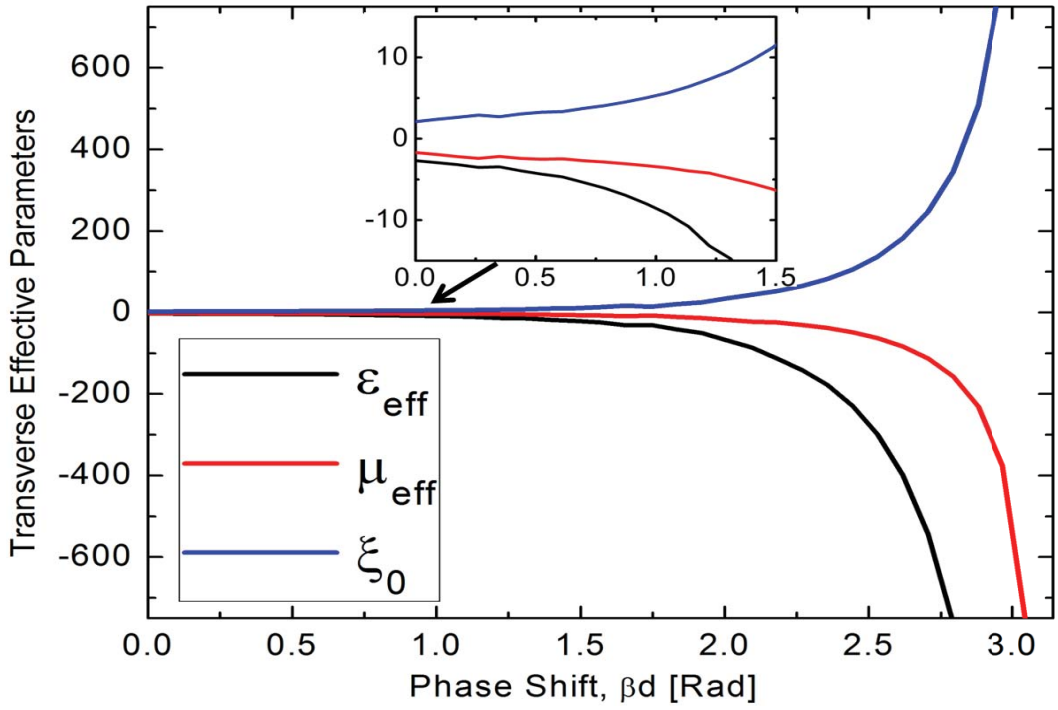

Figure 12: Effective constitutive parameters for the homogenized NIMW of Fig. 7. The inset illustrates the constitutive parameters for small phase shifts [53].

From the calculated characteristic impedance ($Z_{\pm}$) and the wave number β_x, the effective constitutive parameters were extracted, as shown in Fig. 12. The extraction method confirms that the CSRR structure behaves as a NI metamaterial, with Re$\{\varepsilon_{eff}, \mu_{eff}\}<0$ within the frequency band of interest. The effective permeability is relatively flat throughout the band, confirming the fact that the response is due to the sub-cutoff nature of the TM mode. The effective permittivity displays a more dynamic variation in frequency, which is attributed to the CSRRs. The magneto-electric coupling coefficient has a significant relative value, confirming the strong bi-anisotropic nature of wave propagation in the homogenized NIMW.

2.4 NIMW TRANSMISSION-LINE THEORY

In this section, we extract the primary parameters of the metamaterial under analysis from circuit theory and full-wave simulations, with the goal of defining its equivalent TL model. We start from the unloaded parallel-plate waveguide [shown in Fig. 13 (a)]: its TM mode is well modeled by the circuit configuration in Fig. 13(b), in which a series impedance takes into account the effect of the longitudinal electric field E_x and the transverse magnetic field H_y, and a shunt admittance is associated with the transverse electric field E_z. As common in TL analysis, in this circuit model and the more sophisticated ones developed in this section the current in the series branch is directly related to the transverse magnetic field propagating in the structure, while the voltage drop across the shunt branch corresponds to the tangential electric field. The wavenumber and line impedance can be obtained using the exact TM field analysis [23]:

$$\beta_x = \sqrt{\omega^2 \varepsilon_o \mu_o - \left(\frac{\pi}{h}\right)^2}, Z_{TM} = \frac{V}{I} = \frac{\beta_x h}{\pi \omega \varepsilon_o d}. \tag{2.4.1}$$

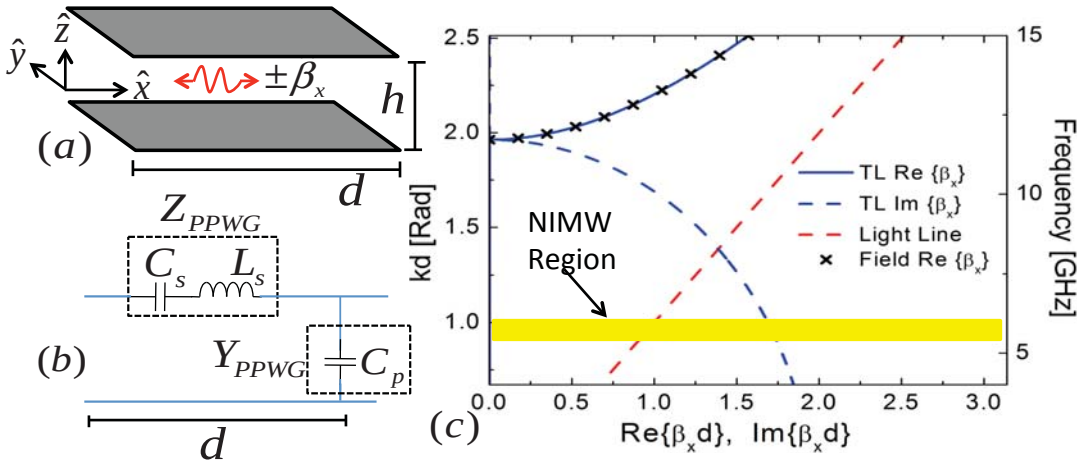

Figure 13: TL model for an empty parallel-plate waveguide (TM propagation), and corresponding modal dispersion [53]. (a) Unloaded waveguide geometry, (b) TL model and (c) dispersion diagram.

The corresponding TL model shown in Fig. 13(b) consists of a distributed series impedance Z_{PPWG} and shunt admittance Y_{PPWG}. Over a finite sub-wavelength period d, their values can be obtained by requiring that $-Z_{PPWG}\,Y_{PPWG} = 4\sin^2(\beta_x d/2)$ and that the ratio between Z_{PPWG} and Y_{PPWG} corresponds to the product of the forward and backward Bloch impedances [23], giving

$$Z_{PPWG} = \frac{\left(1-e^{-j\beta_x d}\right)h\beta_x}{\pi\varepsilon_0\omega d}, \qquad Y_{PPWG} = \frac{\left(e^{j\beta_x d}-1\right)\pi\varepsilon_0\omega d}{h\beta_x}. \tag{2.4.2}$$

For small values of kd, the relationships in (2.4.2) reduce to the conventional expressions $-Z_{PPWG}Y_{PPWG} = (\beta_x d)^2$ and $Z_{PPWG}/Y_{PPWG} = Z_{TM}^2$. The series impedance can be represented as a series LC resonator (L_s and C_s) and the shunt admittance is equivalent to a capacitor (C_p). As expected, an increase in plate spacing h leads to a decrease in C_p and

L_s, while C_s increases. Alternatively, an increase in width or period d causes an increase in C_p and L_s and a corresponding decrease in C_s.

The TL model in Fig. 13(b) acts as a high pass filter above $c/(2h)$, which is consistent with the cut-off of the TM mode and with the fact that the series branch of the circuit model below the cut-off frequency is mainly capacitive, leading to a non-propagating C-C TL [55]-[57]. Above the cutoff frequency, the series inductor dominates, leading to a conventional L-C TL with real propagation constant. The dispersion relation and impedances predicted by the circuit model of Fig. 13(b) exactly match the dispersion relation and impedances from field analysis, as expected and as seen in Fig. 13(c). The frequency window of interest to us is highlighted by the yellow region in Fig. 13(c), and is below the cut-off frequency of the waveguide, consistent with the previous discussion. In this region, β_x, as well as Z_{PPWG} and Y_{PPWG}, are purely imaginary.

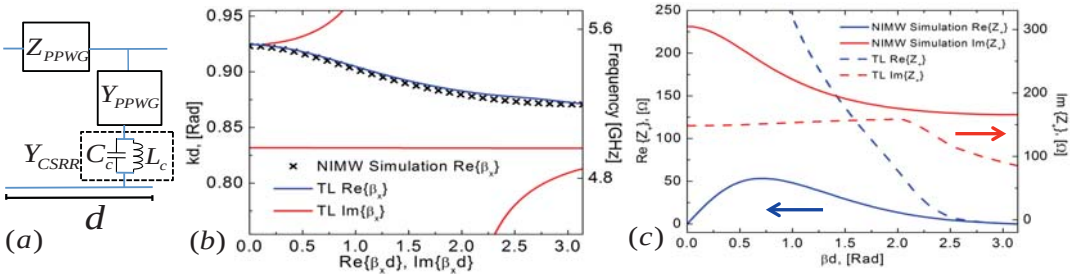

Figure 14: TL model of the NIMW neglecting magneto-electric coupling in the CSRR [53]. (a) TL circuit model, (b) Real and imaginary part of the propagation constant, and (c) real and imaginary parts of Z_+, obtained from full wave simulation. The CSRRs are represented here by an LC resonator in the circuit model.

The presence of a CSRR aperture can now approximately be taken into account in the TL model, as discussed in [16], by including an LC resonator (Y_{CSRR}) in the parallel

branch, as shown in Fig. 14. A passband is revealed below the TM cutoff frequency, associated with the CSRR resonance, which is consistent with our eigen-modal analysis. The additional shunt resonator introduces an inductive response, converting the *C*-*C* TL below cut-off into a *C*-*L* NI TL [58],[59]. For the shunt branch to be inductive, the following condition should be satisfied:

$$\frac{1}{\sqrt{(C_c + C_p)L_c}} < \omega < \frac{1}{\sqrt{C_c L_c}} \tag{2.4.3}$$

which is consistent with [60]. The bandwidth identified in (2.4.3) necessarily includes the NI band and is inherently limited by the geometry of the parallel-plate waveguide. As noted previously, as the plate separation increases, C_p decreases, effectively reducing the available bandwidth of the NI mode.

Condition (2.4.3) is necessary, but not sufficient to sustain the NI passband. A more stringent condition on the circuit parameters may be derived considering that the lower (ω_l) and higher (ω_h) frequencies of the NI propagation band are directly controlled by the total series impedance (Z) and shunt admittance (Y) of the circuit model shown in Fig. 14(a) calculated at $\beta_x d = \pi$ and $\beta_x d = 0$, which translates into $ZY|_{\omega_l} = -4$ and $ZY|_{\omega_h} = 0$. The capacitance and inductance values in the LC resonator can be found in closed-form using the above conditions and (2.4.2) as

$$C_c = -\frac{4\pi\varepsilon_0 d\left(1 - e^{j\beta_x^{(l)} d}\right)\omega_l^2 e^{j\beta_x^{(l)} d}}{j\beta_x^{(l)} h\left(1 + e^{j\beta_x^{(l)} d}\right)^2\left(\omega_h^2 - \omega_l^2\right)}, \quad L_c = \frac{1}{C_c \omega_h^2}, \tag{2.4.4}$$

where $\beta_x^{(l)}$, a purely imaginary term, is the wavenumber in the empty parallel-plate waveguide, calculated using (2.4.1) at $\omega = \omega_l$. With the relationships provided in (2.4.4), the circuit elements modeling the CSRR in Fig. 14 (C_c, L_c) can be easily identified. The calculated values for the example at hand are L_c = 0.506 nH and C_c = 1.65 pF. The corresponding dispersion graph for the TL model is shown in Fig. 14(b), and it closely follows the full-wave band diagram in the propagating NI region, validating our TL analysis.

The model in Fig. 14(a) is obviously approximate, as it assumes that the CSRRs only interact with the transverse electric field; for this reason, it cannot capture the inherent bi-anisotropy of the unit cell highlighted in the previous section, which arises from the CSRR asymmetry in the direction of propagation. While this model can well capture the dispersion features of the metamaterial, it cannot describe the characteristic impedance, as can be seen in Fig. 14(c). With the goal of accurately capturing all the physics of NIMW propagation within a simple TL model, we introduce the improved circuit configuration in Fig. 15.

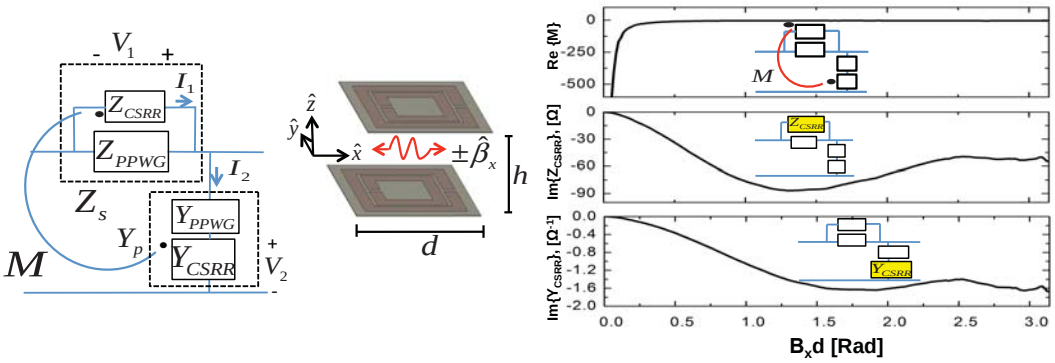

Figure 15: A more accurate TL model allows for the accurate prediction of dispersion and impedance of the proposed metamaterial [53]. The mutual coupling M is defined between Z_{CSRR} and Y_{CSRR}.

Here, we load the series branch with an additional impedance (Z_{CSRR}) to take into full account the interaction of the CSRR with the transverse magnetic field (current), i.e., to model the non-negligible magnetic response of the loading inclusion, and a coupling coefficient M between Z_{CSRR} and Y_{CSRR} that models the bi-anisotropic effects arising in the CSRR, associated with the inherent asymmetry within the unit cell in the direction of propagation. This asymmetry is well-known to produce magneto-electric coupling within the inclusion, associated with its bianisotropic nature and consistent with earlier works for split-ring resonators [21].

In terms of currents and voltages in the unit cell, as indicated in Fig. 15, the coupling term introduces the following equations:

$$\begin{aligned} V_1 &= Z_{CSRR} I_1 + M Z_{CSRR} I_2 \\ I_2 &= Y_{CSRR} V_2 - M Y_{CSRR} V_1 \end{aligned}, \tag{2.4.5}$$

which ensure that reciprocity is satisfies in the two branches of the circuit. We note that the mutual coupling term used here differs from the more conventional definition, as used, e.g., in [55]. This is done in order to simplify the relationship with the magneto-electric coupling coefficient of the homogenized metamaterial. The proposed TL unit cell is characterized by the secondary parameters [23]

$$
\begin{aligned}
4\sin^2\left(\beta_x d/2\right) &= \frac{-Y_p Z_s}{1+MY_p Z_s\left(1+M\right)} \\
Z_+ &= \frac{Z_s}{2}\left(1+2M+j\cot\left(\beta_x d/2\right)\right) \\
Z_- &= -\frac{Z_s}{2}\left(1+2M-j\cot\left(\beta_x d/2\right)\right),
\end{aligned}
\tag{2.4.6}
$$

where Y_p and Z_s are the total admittance and impedance in the shunt and series branches, and $\beta_x d$ is the phase shift across each unit cell.

The forward and backward impedances are different, due to the mutual coupling coefficient, capturing the structure's bi-anisotropy. This model holds to a good degree around the NI band, for which the interaction with the CSRR is strong and resonant. In the case of lossless elements, all the impedance and admittance values are imaginary, and the mutual coupling coefficient is real.

Fig. 15 shows the new TL parameters numerically extracted using (2.4.6) as a function of phase shift in the NI band (the other parameters are obtained from the results in Fig. 13 and Fig. 14). All parameters are dispersive, but they are fairly constant other than at the edges of the band of interest, and they can precisely and accurately model the wave propagation in the metamaterial. By combining (2.3.7) and (2.4.6), we can identify

the relationship between the mutual coupling coefficient M and the effective magneto-electric coupling coefficient ξ_0:

$$\xi_0 = -\frac{\beta_x d}{kd}\frac{(1+2M)}{\cot(\beta_x d/2)}. \tag{2.4.7}$$

It is of special interest to analyze this model in the range for which $\beta_x d \ll 1$, on the edge of the NI band. We notice in Fig. 15 that in this region M diverges, a necessary condition to maintain a finite value of magneto-electric coupling, as predicted in Fig. 12, even if Z_s and Y_p tend to zero in the same limit. In this limit (2.4.5) implies $V_1 = I_2 = 0$, i.e., the TL unit cell corresponds to an ideal short-circuit connection between entrance and exit, consistent with a zero phase propagation. It should also be mentioned that the singularity of the coefficient M is consistent with the usual constraints on the coupling coefficient between two reactive elements: in the notation of (2.4.5), we simply require that $\mathrm{Im}[Z_{CSRR}]/\mathrm{Im}[Y_{CSRR}] > 0$ to ensure that the mutual coupling between reactive elements is consistent with energy requirements, independent of M.

Previous TL models, like the one in Fig. 14, have successfully predicted the modal dispersion, but not the line impedance of similar metamaterial geometries [12],[16]. With the primary parameters introduced in Fig. 15, on the contrary, we are able to fully capture the propagation properties of the proposed NI parallel-plate metamaterial within a TL model, which closely matches full-wave simulations. Before closing this section, we notice that in [56] a 3-D loaded waveguide metamaterial was described using a sophisticated transmission–line model, resulting in a negative index band. However, the

unit cell inclusions in that design were not inherently bi-anisotropic, leading to an alternative description of the mutual coupling term than the one presented here.

2.5 Unit Cell Optimization and Elimination of Bi-anisotropy

After having successfully analyzed the original unit cell design shown in Fig. 7, we can apply the insights provided by the TL model to design a modified unit cell that increases the bandwidth and shifts the NI band to lower frequencies for a given period [53],[61]. The optimized unit cell design parameters are outlined in the caption of Fig. 16. We fixed the height of the plate spacing (h) for ease of future experimentation with particle beams. When the inside metallic patch is enlarged (g_1 is reduced), the spacing between the inside metal patch and the middle ring is decreased, resulting in an increased capacitance (C_c) in the TL model of Fig. 14. By decreasing the outside aperture, a similar effect prompted an increased C_c. However, the reduction of the effective radius on the outer loop led to a decrease in TL inductance (L_c). This result is analogous to the effects of a changing radius on inductance on an isolated current loop [62]. It was decided to maintain the outer aperture width, since the decrease in inductance leads to a higher resonant frequency. By adjusting the two apertures, we can increase the product of C_c and L_c, thereby reducing the resonance frequency of the inclusion. In addition to the apertures, the metal connections between the resonators (g_2) were examined. The effective inductance and capacitance vary with the size of g_2, but their product (C_cL_c) remains relatively constant. Unlike the apertures, the width of the metal connections only affected the bandwidth, not the high frequency pole (ω_h). By tuning g_2, we increase L_c, and thereby reduce the lower frequency pole, as shown in (2.4.3).

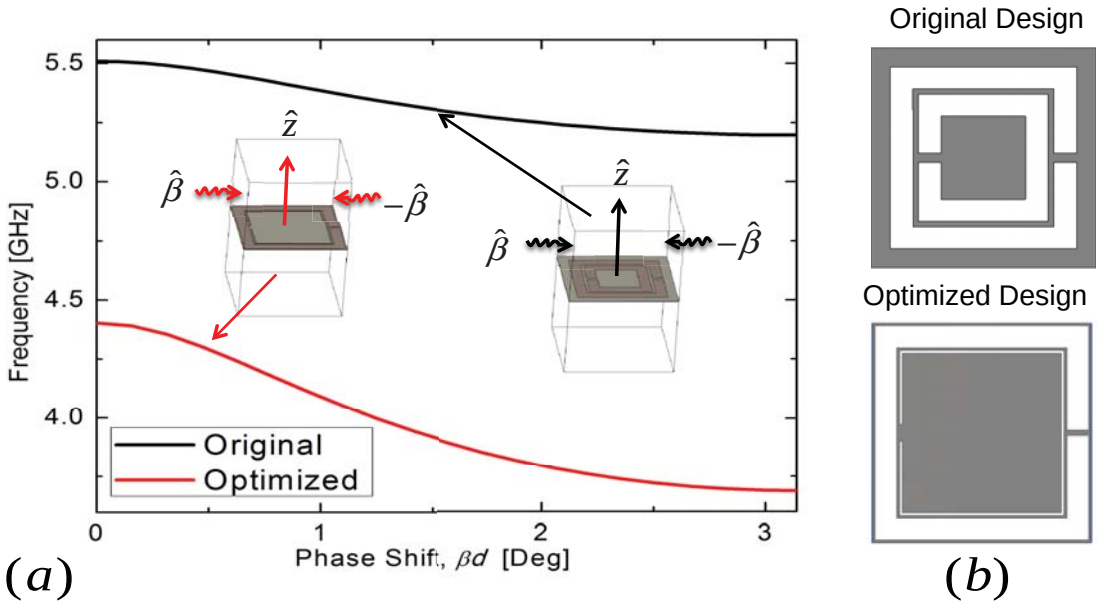

Figure 16: Optimization of the CSRR structure to reduce the frequency of operation and increase the bandwidth [53]. (a) Black and red lines show the dispersion diagram of the original and optimized designs, respectively. The unit cells are shown as insets. The optimized parameters are: $d = 8$ mm, $L_1 = 7.8$ mm, $L_2 = 6.2$ mm, $g_1 = 0.1$ mm, $g_2 = 0.6$ mm, and $g_3 = 0.1$ mm. Plate thickness (t) is 0.05 mm. (b) Graphical display of original and optimized unit cell.

With the above analysis, we optimized the CSRR parameters in order to maximize the bandwidth of operation: when the aperture and inner resonator (g_1, g_3) is reduced to 0.1mm and the difference between L_1 and L_2 remains constant, the NI mode spans a broader range of frequencies from 4.4 to 3.7 GHz around the normalized wavenumber $kd \approx 0.74$. Fig. 16(a) illustrates the improvement in dispersion of this optimized unit cell compared to the original design of Fig. 7. The TL parameters for the optimized unit cell are $C_c = 0.444$ pF and $L_c = 2.94$ nH, obtained from (2.4.4). The differences in physical layout are shown in Fig. 16(b).

In order to eliminate the undesirable bi-anisotropic response of metamaterial ring resonators, several solutions have been proposed, including broadside coupling of two SRRs [21]. In this geometry, a more convenient topology is represented by alternating CSRRs (ACSRR) with opposite orientation along the direction of propagation, eliminating the inherent asymmetry of the periodic configuration. The new unit cell of the metamaterial is shown in Fig. 17(a), with a period S that is twice the period of the original CSRR structure ($S = 2d$). The TL model for the symmetric NIMW geometry is composed of two mirrored circuits as shown in Fig. 17(b), in which the coupling terms cancel each other and force $Z_+ - Z_- = 0$.

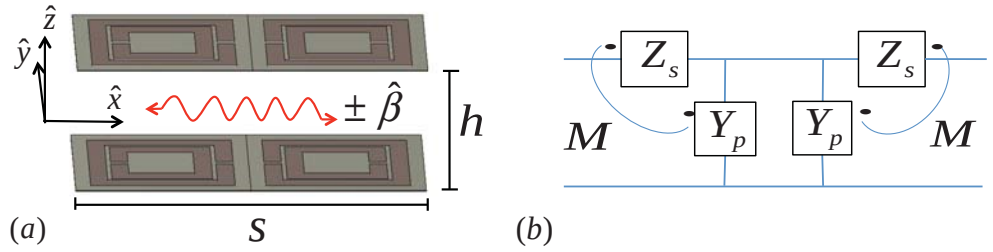

Figure 17: Alternating CSRR design (a) to eliminate bi-anisotropy and (b) TL model for ACSRR NIMW [53].

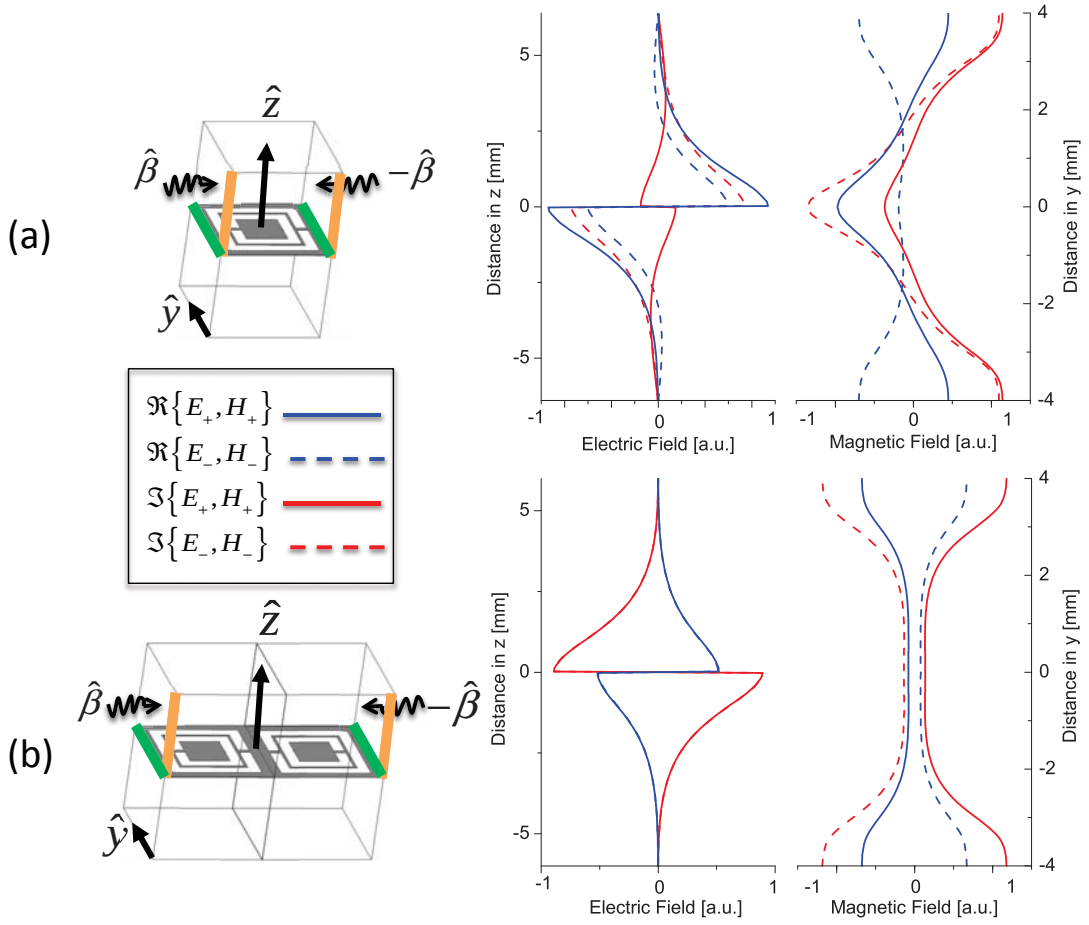

Figure 18: Field distributions for (a) the tangential electric and magnetic fields in the original CSRR metamaterial at $x = -d/2$, for 60° phase shift across the unit cell and (b) alternating CSRR NIMWs at $x = -S/2$, for 120° phase shift across the unit cell. The electric field distribution lines in (b) are exactly on top of each other, as expected for symmetry [53].

A more detailed investigation of the field distribution within each unit cell can provide physical insights into the connection between bi-anisotropy and unit cell design. The field distribution in the transverse plane for the original CSRR design at $\beta_x d$=60° is

shown in Fig. 18(a). The same propagation constant ($\beta_x s$=120°) is used to plot the fields in the ACSRR design in Fig. 18(b), for fair comparison. Real and imaginary parts of E_z (H_y) are plotted along a line parallel to z (y), as shown with orange (green) lines in the inset of Fig. 18. Forward ($+\beta_x$) and backward ($-\beta_x$) propagations are considered on the corresponding entrance planes ($x = -d/2$ for $+\beta_x$ and $x = +d/2$ for $-\beta_x$). It is seen how there is a visible difference between the two entrance planes for forward and backward modes in the original design, which is compensated in the ACSRR case.

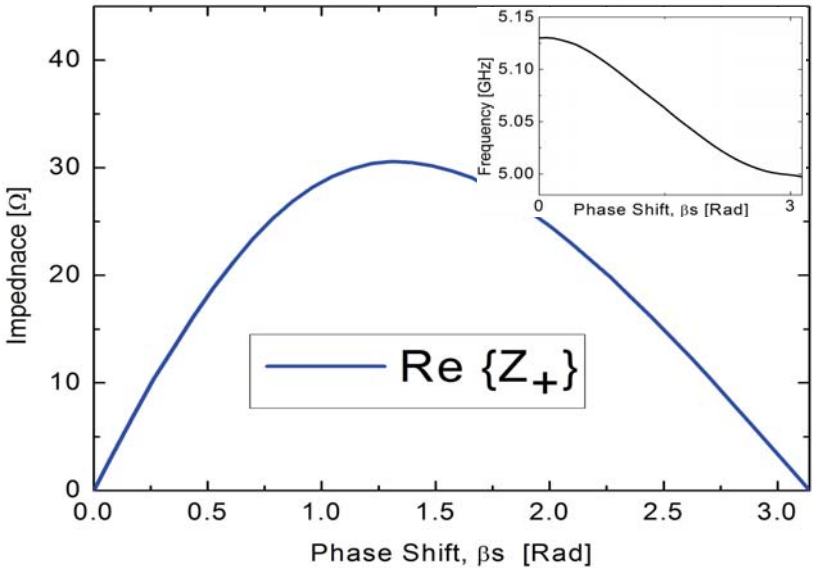

Figure 19: Effective impedance for the alternating CSRR design [53]. The dispersion plot for the alternating CSRR is shown in the inset. The forward and backward impedances are equal and real within simulation accuracy (± 2 Ω).

The associated effective impedance for the ACSRR geometry is shown in Fig. 19. In contrast to $Z_\pm$ of the CSRR NIMW (Fig. 12), the ACSRR NIMW produces equal, real

impedances (blue lines in Fig. 19), regardless of the direction of propagation ($Z_+ = Z_- = \mathrm{Re}\{Z\}$), ensuring that the ACSRR design can eliminate the bi-anisotropy while maintaining the desired NI behavior. The dispersion graph for this geometry is shown in the inset of Fig. 19.

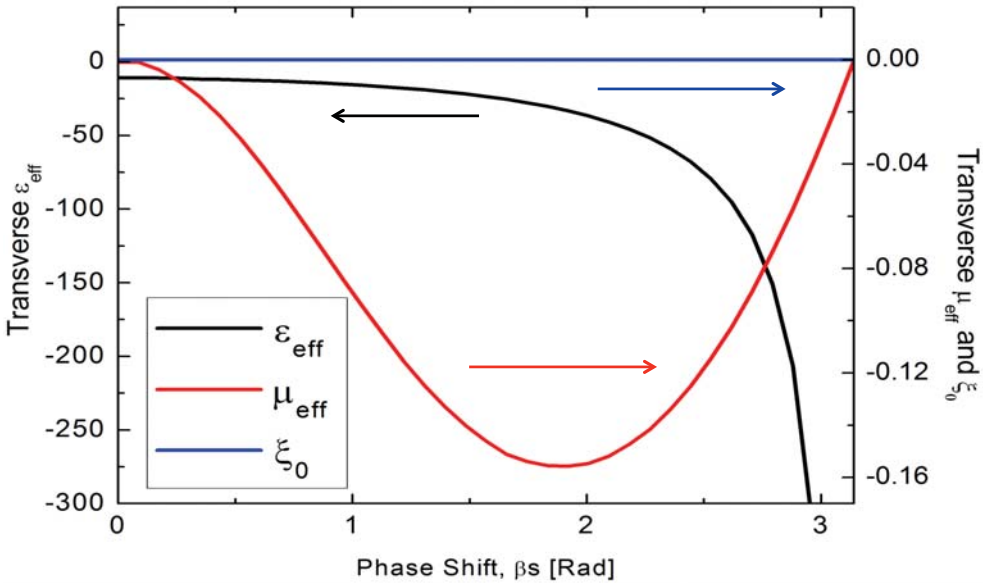

Figure 20: Effective transverse constitutive parameters for the homogenized ACSRR NIMW [53]. Real part of ε_{eff} and μ_{eff} are negative, as predicted, and the megnetoelectric coupling ξ_0 is eliminated, suggesting a dramatic reduction in bi-anisotropic response of the structure.

From the characteristic impedance ($Z_\pm$) and the wave number (β_x), the effective constitutive parameters were extracted using (2.3.7), as shown in Fig. 20. In this ACSRR case we still have negative permittivity and permeability, $\mathrm{Re}\{\varepsilon_{eff}, \mu_{eff}\}<0$, but we manage to suppress the bi-anisotropy coefficient throughout the band of interest. The same mechanisms producing NI propagation of the original design are still present here. The

effective permeability interestingly becomes very close to zero all across the band of interest in this alternative design, while the negative permittivity quickly becomes very large moving towards the bandgap, as in the symmetric case. This is necessary to ensure $\mu_{eff} = 0$ at the edge of the bandgap, for which $\beta_x = \pi/S$ is finite. The near-zero permeability of this metamaterial design may be useful for microwave absorption, antenna directivity enhancement and radiation pattern shaping [63],[64].

2.6 NIMW SLAB SCATTERING AND EXCITATION

After having established the eigen-modal properties of the metamaterial in the previous sections, we consider the scattering properties of a finite sample of NIMW metamaterial. As found in Section 2.2, a TEM positive-index mode also exists in the frequency band of interest, which may be excited by an external plane wave. Excitation at normal incidence with an electric field orthogonal to the plates indeed couples most of the impinging energy to the TEM mode. For this reason, we consider exciting the structure with oblique TM incidence, for which the electric field lies in the plane of the metallic plates, as shown in Fig. 21(a). In this case, while the impinging electric field does not have any component orthogonal to the plates, the longitudinal electric field at oblique incidence can ensure coupling to the NI mode without any interaction with the TEM mode.

Fig. 22 shows the transverse electric field distribution inside and around a finite slab composed of eight unit cells, excited by such obliquely incident TM wave. As can be seen from the phase fronts in this figure, the plane wave indeed excites the NI mode inside the structure, producing negative refraction. Fig. 21(b) shows the electric field

vector distribution in a side view. Once the incident wave enters the NIMW, the fringing effects induce the magneto-electric coupling, leading to NI wave excitation. A strong E_x component is shown at mid-plane, which allows for the interaction with a charged particle beam. It has been reported that the longitudinal electric field and particle interaction can also translate into an effective active metamaterial [18], as the wave propagating in the structure can draw energy from the electron beam.

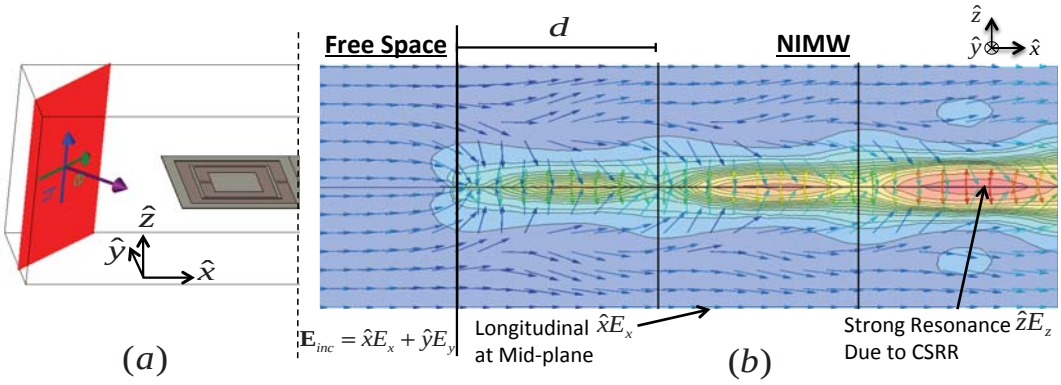

Figure 21: Excitation and electric field distribution for a plane wave at 45° incidence at 5.6 GHz [53]. (a) Plane-wave excitation perspective and (b) electric field response to plane wave excitation in a side view. The metamaterial is truncated in the longitudinal direction (first 3 cells shown in figure). Vertical lines illustrate the separation between unit cells. For clarity, only the E_x and E_z components of the electric field vector are shown in part (b). The $|Ez|$ distribution is shown as a contour plot to illustrate the resonant behavior of the CSRRs.

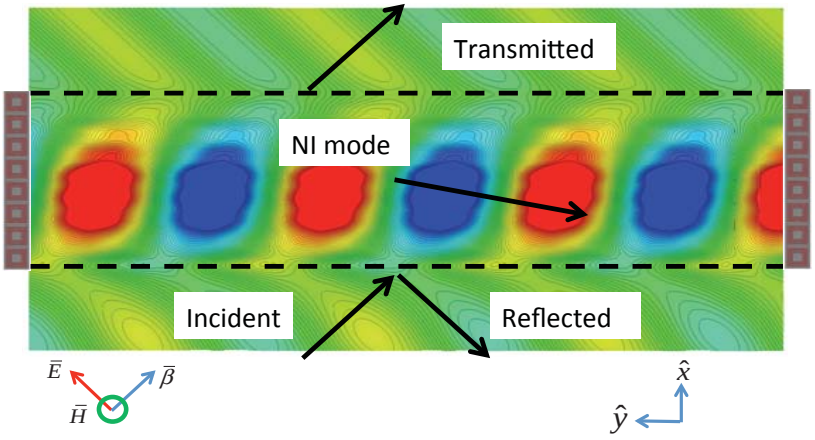

Figure 22: Electric field distribution (snapshot in time) for the excitation of the CSRR metamaterial with an obliquely incident plane wave at 5.6 GHz [53].

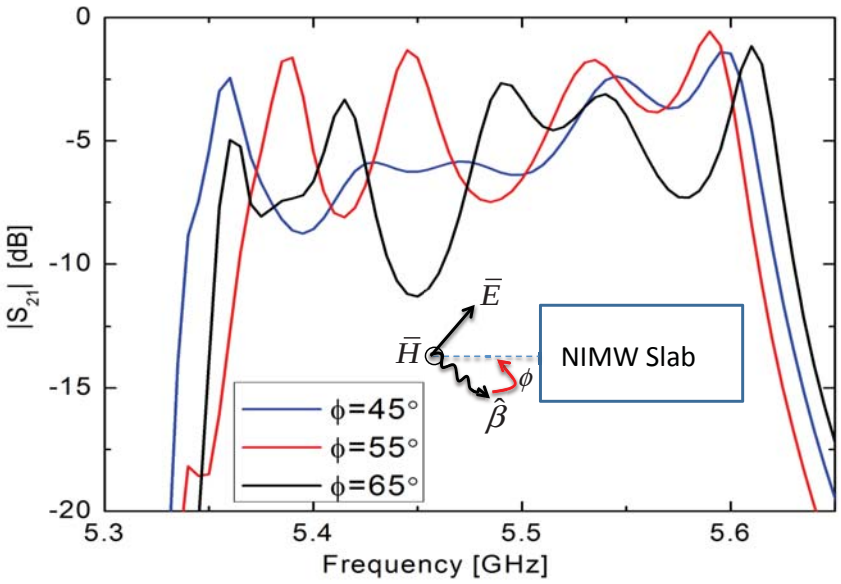

Figure 23: The transmission coefficient for different incidence angles [53]. NIMW supports a pass band between 5.3 to 5.6 GHz, which closely matches the dispersion response of the infinite periodic simulations previously shown. Ripples in the transmission are due to Fabry-Pérot resonances, indicative of partially mismatched interfaces.

The transmission coefficients for the 8-cell CSRR structure for different angles of incidence are shown in Fig. 23. In all cases an NI passband is observed, consistent with the results of the eigen-mode simulations and TL model. The variations in transmission within the passband are due to the mismatch between free-space and the CSRR structure, leading to multiple Fabry-Pérot resonances. If the design were matched to free space, a smooth pass band would be expected.

2.7 Experimental Validation of a 1D NIMW

Before progressing to a full scale NIMW configured for beam interaction, it is advantageous to validate the electromagnetic properties of the NIMW in a simplified, cost effective structure [65]. The CSRR loaded waveguide introduced here is specifically tailored to emulate the electromagnetic coupling properties of the NIMW; the field distribution is consistent with the full bulk metamaterial in the central portion of the waveguide, while it changes near the waveguide boundaries. Due to the boundary condition constraints, in fact, the longitudinal electric field component of the NIMW, necessary for electron beam coupling, cannot be present on the lateral walls of the waveguide.

At first glance, the presented experiment may appear similar to past research involving resonator-loaded waveguides. Previous experiments featured a host waveguide loaded with SRRs, where the negative permittivity is due to the dominant transverse-electric (TE) mode operated below cut-off, and the negative permeability is due to the interaction between an axial magnetic field and the SRRs [12],[13]. Additionally, CSRR-based metamaterials were embedded in microstrip transmission lines, operating in a

TEM-like mode [16]. In the experiment presented here, on the contrary, we excite a sub-cutoff transverse-magnetic (TM) mode, which corresponds to an effective negative permeability, while the CSRR inclusions interact with an axial electric field, which provides an effective negative permittivity. Also this geometry is expected to support NI propagation. To the best of our knowledge, this is the first experimental demonstration of a CSRR-loaded TM rectangular waveguide supporting negative-index response.

The geometry and unit cell of the NIMW, as first reported in [18], has been modified and optimized for a conventional waveguide, as seen in Fig. 24. Our experimental apparatus, shown in Fig. 25, consists of a 13 cm long X-band waveguide loaded with a single column of 13 CSRRs, as shown in Fig. 26. The CSRR unit cell was tailored so that the length and width were the exact size as the width of the X-band waveguide. The CSRR plate was fixed at the center of the waveguide, and end caps were mounted to both waveguide flanges.

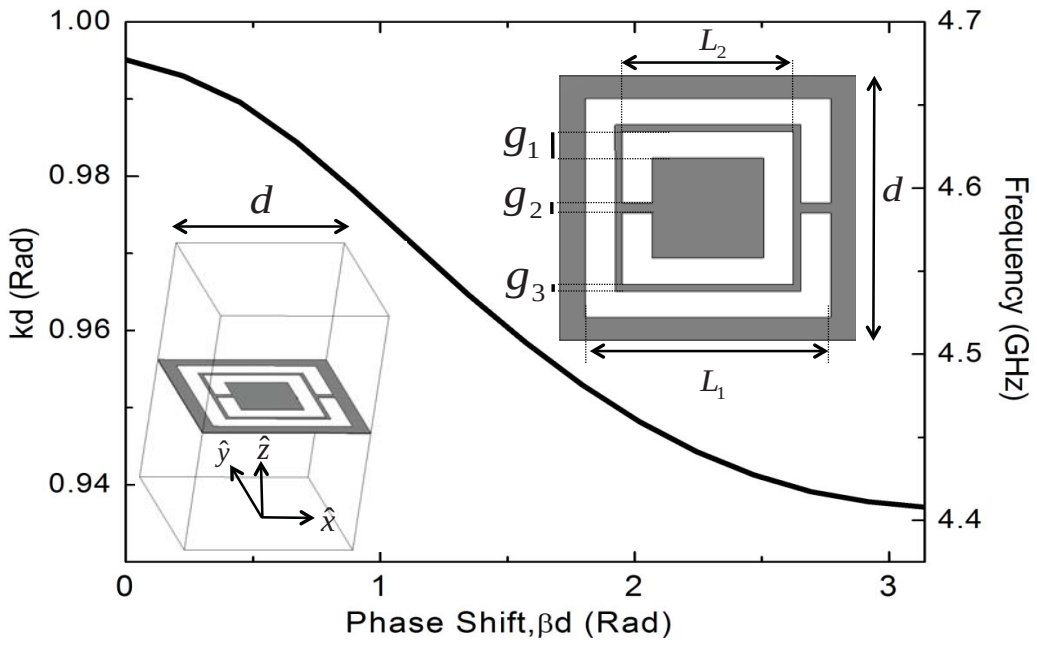

Figure 24: The dispersion diagram for an infinite periodic NIMW [65], a scaled version of the original unit cell proposed in [18]. Bottom left inset is the unit cell, top right is the CSRR geometry. The CSRR dimensions are: d=10.16mm, L_1= 4.19mm, L_2=5.84mm, g_1=1.02mm, g_2=0.38mm, and g_3=0.25mm. Plate thickness is 0.25mm and unit cell height is 12.8mm.

Proper excitation, due to the odd symmetry of the NI mode, requires odd symmetry around the CSRR plane. Efficient coupling to the odd NI mode requires a pair of excitation probes, with 180° phase difference. In order to avoid such complexities, a simple, asymmetric excitation scheme was chosen. The stimulation was optimized to closely match the electric field distribution on the top region of the CSRR plate, leading to the most efficient coupling for this simple excitation mechanism.

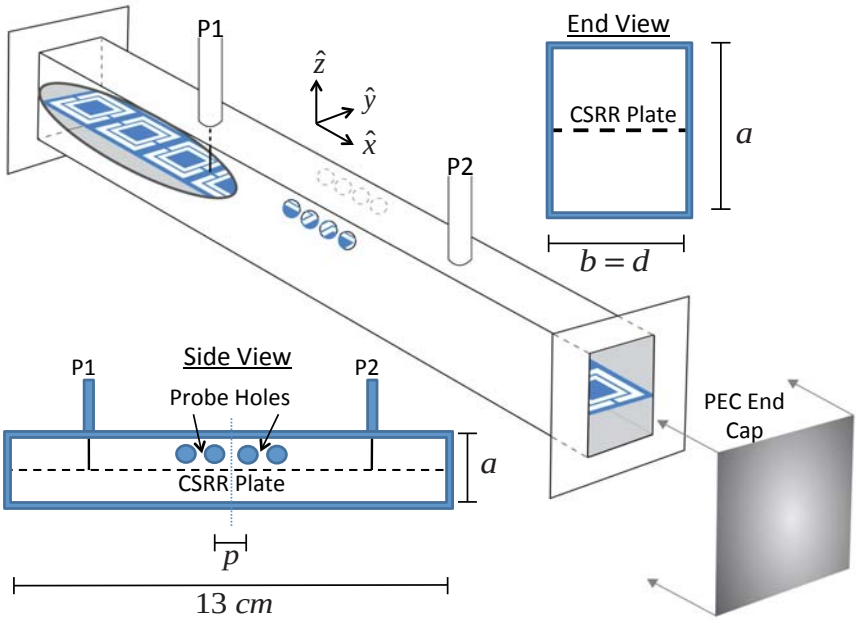

Figure 25: Rendering of the experimental apparatus [65]. A conventional waveguide is loaded with a single column of 13 CSRRs with metal caps placed on the end flanges. The 13 cm X-band waveguide dimensions are: a=22.86cm, b=10.16cm. The spacing between probe holes, p, is 5 mm.

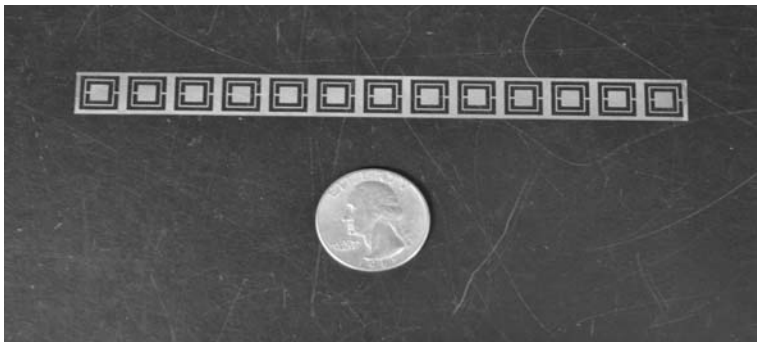

Figure 26: A single column of 13 CSRRs approximately 13 cm in length [65]. Their geometry is consistent with the one shown in the inset of Fig. 24.

Two SMA receptacle terminals were mounted to the upper waveguide wall, located between the third and fourth CSRR inclusion from each end. The inner pin for the receptacle was terminated on the CSRR plate whereas the outer jacket was grounded on the waveguide. The location of the terminals and depth of the excitation/extraction pin was determined through simulations in order to maximize matching in the passband. In order to extract the phase within the passband, eight probe holes were etched out in the waveguide walls. The probe holes were placed at a spacing (p) of 5 mm on both sides of the waveguide while collecting pertinent phase information. The holes on each side of the waveguide were offset, allowing for a field sample every 2.5 mm, due to lateral symmetry of the structure. Simulations and experiments confirmed that the drilled holes caused limited perturbations on the propagation mode of interest; surface currents on the waveguide walls at the probe locations were minimal. At each probe location (x_k), relative magnitude and phase information ($|E|$, ϕ_E) was collected.

If we can neglect reflections at the waveguide termination, the exciting probe produces as a single traveling wave of the form

$$\overline{E} = \overline{E}_o e^{-j\beta x_k}, \tag{2.7.1}$$

where x_k is the relative location of the probe at the k^{th} hole along the direction of propagation. While the relative phase of the fields change given the probe locations, the wavenumber β remains unchanged, and therefore it may be extracted from the relative electric field measurements at each frequency.

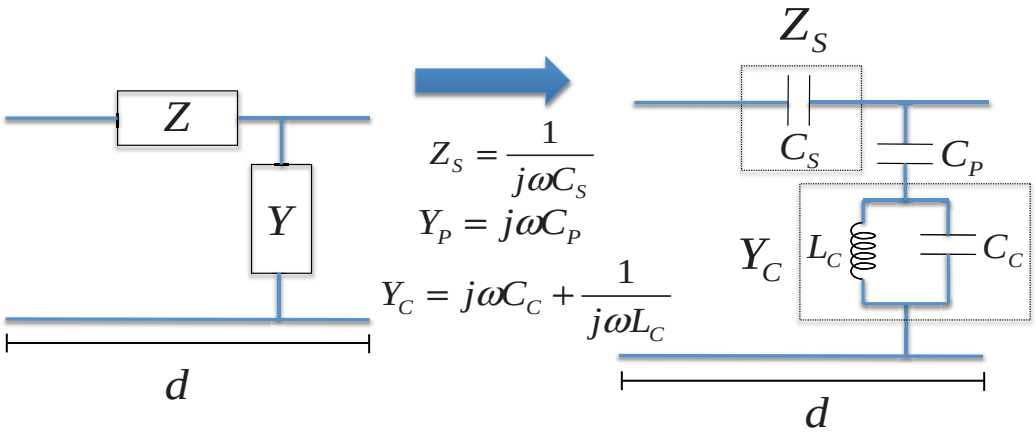

Figure 27: A periodic TL model for the waveguide with embedded CSRRs [65]. Since the transmission-line unit cell is of finite length, all lumped circuit elements are in units Farads/Henrys. This transmission line has the dispersion relation shown in (2.7.2).

Given a sufficient sampling of extracted wavenumbers, we extrapolate the dispersion relation from a derived transmission-line (TL) model describing the NIMW, as shown in Fig. 27. A periodic TL, which takes into account the effects of the waveguide and embedded CSRR plate (Section 2.4), provides a dispersion relation

$$4\sin^2(\frac{\beta d}{2}) = -ZY = -\frac{Z_S Y_C Y_P}{Y_C + Y_P}, \tag{2.7.2}$$

where Y_C is the shunt admittance due to the CSRR resonance [16], Y_P is the parasitic capacitance, and Z_S is a series capacitor that emulates the effects of TM mode propagation. This model does not account for the inherent bi-anisotropy of the CSRRs, but it is sufficiently accurate to predict and model the NI propagation band. If the CSRR plate were removed from the waveguide, the equivalent circuit reduces to a non-propagative *C*-*C* TL, as expected for waveguide operation below the cutoff frequency.

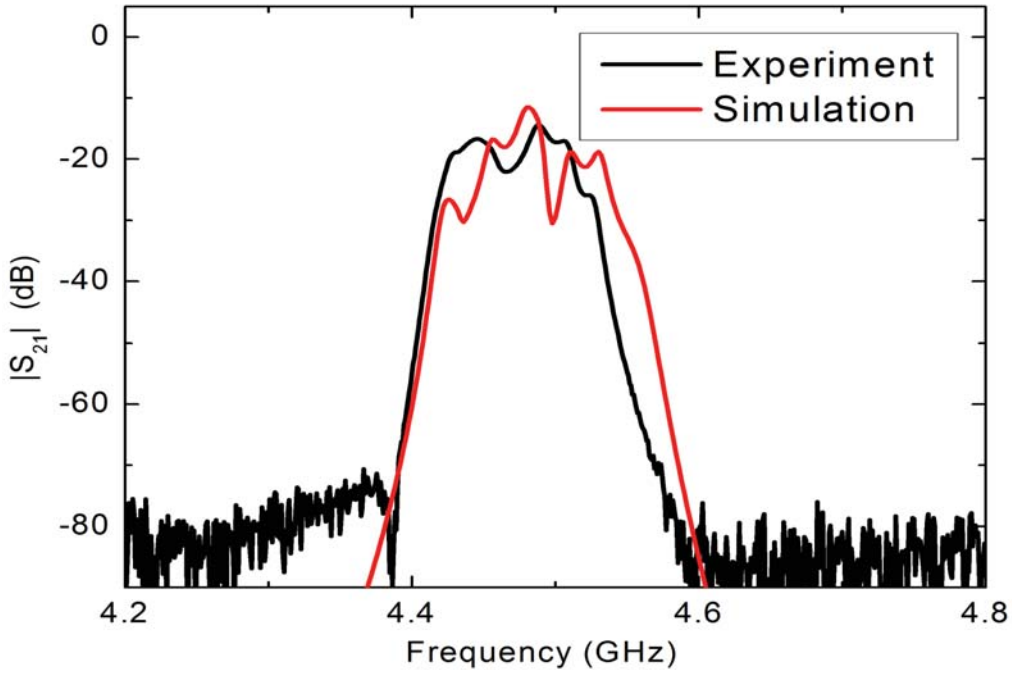

Figure 28: Magnitude of the transmission parameter for experimental (black line) and full wave simulation (red line) data [65]. Both are in good agreement and reveal a passband between 4.4 to 4.6 GHz.

A vector network analyzer was used to extract the scattering parameters in the described experimental apparatus. Transmission data were collected across the expected frequency range, and compared with simulations. A plot of measured transmission magnitude and corresponding full-wave simulations are shown in Fig. 28. The anticipated bandpass, an indicator for NI response, was obtained from 4.4 to 4.6 GHz, well below the cut-off of the TM waveguide mode. The results are in good agreement with full wave simulations and past SRR loaded waveguide experiments [12],[13]. Variation in experimental and simulation results are attributed to the variance in parameters, such as

position of the CSRR plate, port receptacle locations, or warping of the CSRR plate inside the waveguide.

Due to the simplified excitation scheme, which was not impedance matched, and Ohmic loss, the largest transmission magnitude was approximately -12 dB. Within the passband, leakage and dissipation loss was generally limited to less than 3 dB. Conduction losses are expected in resonant or dispersive structures, where large field enhancements are typically induced.

Without the CSRR loading, the waveguide alone only supports evanescent modes in this frequency band, leading to a complete stopband below the cutoff frequency. When the CSRRs are embedded, a strong, transverse magneto-electric coupling between the electric and magnetic fields allows for propagation. This propagation band is only present when there is a strong CSRR resonance, as predicted in the dispersion mode of Fig. 24 and the transmission-line model in Fig. 27 and (2.7.2).

The measured scattering parameters indicate that the best match to the experimental apparatus is around 4.41 GHz. As previously described, the wavenumbers were extracted in this region and fit to the TL dispersion relationship (2.7.2). The extracted wavenumber data points (markers) and resulting wavenumber fitted curves (solid lines) are shown in Fig. 29. For comparison, the simulation of an infinite, loaded waveguide with periodic boundary conditions is also shown.

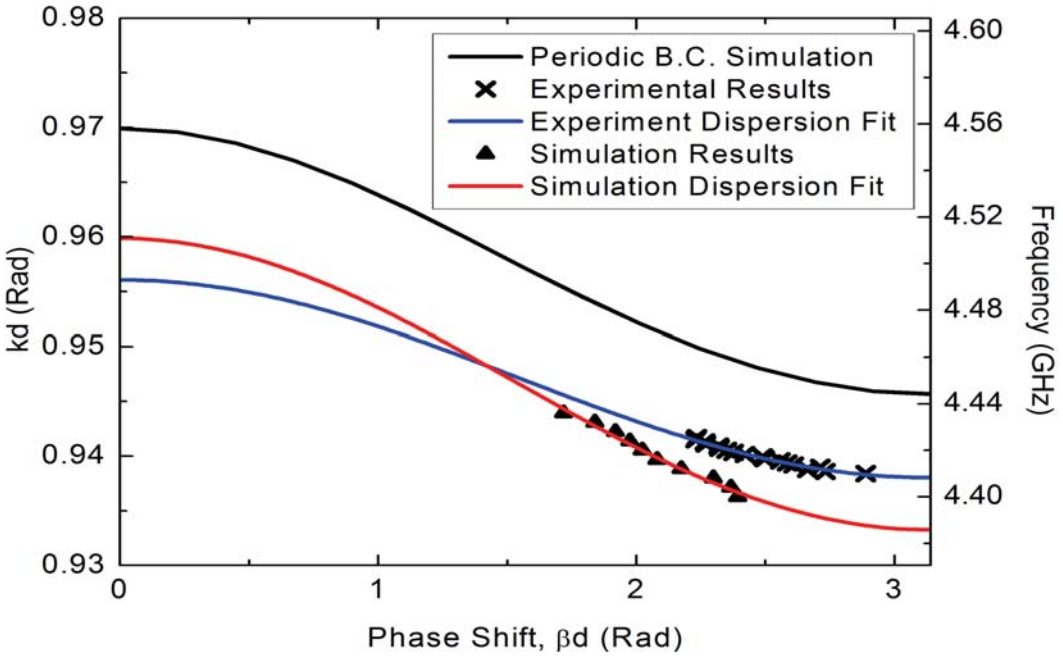

Figure 29: Dispersion diagram for the X-band, CSRR loaded waveguide [65]. Wavenumbers extracted from the experimental and simulated data points are shown as markers. The fitted curves based on the transmission-line model are shown as blue and red lines. Dispersion curve of simulated infinite structure is shown in black line. All three dispersion plots signify negative index behavior within the pass band for all phase shifts.

All measured dispersion bands confirm a NI response, with a negative slope for the phase relationship between 4.39 to 4.56 GHz. The extracted dispersion for the experimental (blue line) and simulation (red line) results are well aligned, with the simulated dispersion resulting in a moderately broader bandwidth. We note that the simulation of an infinite, periodic CSRR loaded waveguide (black line) provides an even wider propagation band, at a higher frequency of operation. The proposed experimental apparatus is only an approximation of the 2D periodic structure and therefore should not

match exactly with the eigen-modal simulation. However, it provides a similar dispersion in the expected frequency range.

2.8 NIMW ELECTRON BEAM COUPLING

In any application involving wave-particle interaction, it is essential to be able to study techniques to inject and extract electromagnetic power into and from the structure. A simple way to study effects of various parameters on the capacity of power transfer to the structure is shown in Fig. 30(a). We have simulated a four-port network of WR-340 rectangular waveguides. The waveguides at the top and bottom of the structure are connected together via a rectangular cavity filled with rows of CSRRs. Although, in this simple example, the structure is not optimized for the best coupling to the CSRR structure, it is evident from the simulation results that in the frequency band of operation there is a relatively strong interaction between the fields propagating in the waveguides and the cavity filled with CSRRs. In Fig. 30(b), two of the S-parameters are shown. Since there is no interaction between CSRRs and the propagating wave below 2.41 GHz and above 2.9 GHz, S_{21} is not affected by the presence of CSRRs and there is virtually no coupling between the two waveguides in those frequency ranges. However, in the frequency band of operation, S_{21} decreases significantly. This decrease in transmitted power to the second port is in parts due to injection of power into the cavity and the reflection of power back into port 1.

By changing the vertical distance between the rows of CSRRs, one can control the amount of power extracted by the cavity to some extent. As the distance between the rows is decreased, the coupled power increases. This is due to the fact that as CSRRs

from neighboring rows come closer to each other, the resonant fields which are located very close to the CSRRs can have a more significant effect on their neighboring resonators. However, decreasing the vertical distance between CSRR will reduce the free space for the electron beam to travel. Therefore the minimum distance which is still suitable for electron beam to travel is the best choice.

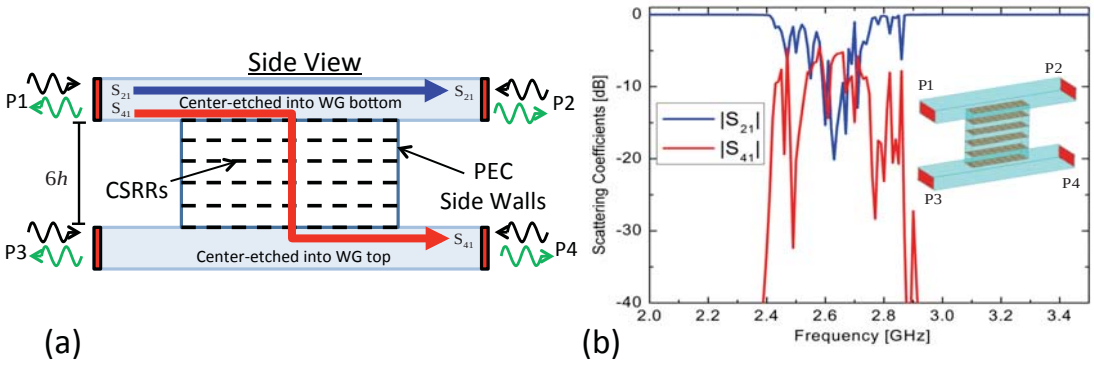

Figure 30: (a) Patterned CSRR cavity resonator coupled to a conventional WR 340 waveguide with unit cell of dimensions in Fig. 1. (b) Transmission coefficients for the waveguide across the CSRR cavity (S_{21}) and through the cavity to the bottom waveguide (S_{41}). The top and bottom waveguides have the outmost CSRR plates etched into the WR 340 for efficient coupling.

In addition, we can study the effect of the width of CSRR rows on the coupling. By increasing the number of CSRRs in the width of each row, we are able to change the width of the cavity in quantized steps, without changing the resonance frequency of the CSRRs. This will change the resonant frequency of the cavity and has an enormous effect on the behavior of the coupling from top to bottom waveguide. In numerical simulations, we have found that increasing the number of CSRRs in each row from one to two improves the coupling considerably. However, three CSRRs in each row worsen the coupling through the cavity. Larger numbers of CSRRs in rows are computationally

expensive and are not simulated. Although these simulations can provide us with a computationally cheap understanding of how the fields interact with the CSRR filled cavity, a simulation with the presence of the electron beam is necessary to study the performance of the structure in more realistic situations.

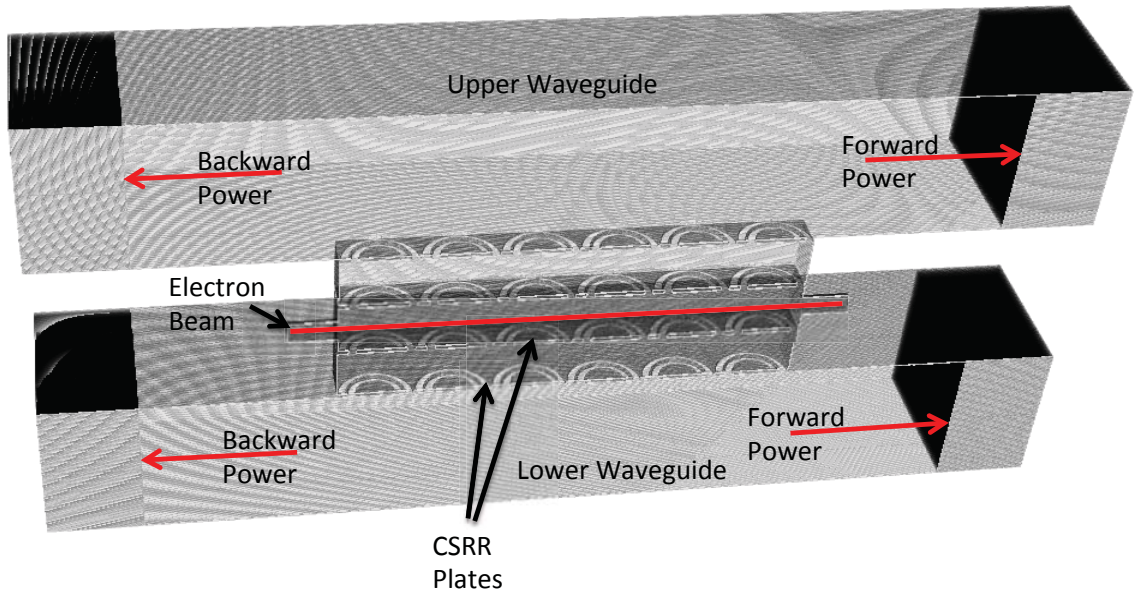

Figure 31: 3D build of the NIMW structure used in the ICEPIC simulations. An electron bean is propagated down the center of 4 CSRR plates, with waveguide ports mounted above for extraction of the wave energy.

An electron beam driven CSRR based source has been simulated in the finite difference time domain (FDTD) code ICEPIC (see [66] as an example) for the geometry seen in Fig. 31. The simulation uses an injected beam with energy of 150 kV and current of 100 A guided by a 1 T magnetic field oriented along the beam propagation direction. As the beam interacts with the electromagnetic fields in the structure, it leads to bunching

of the electron beam and energy transfer to the fields in the structure. The microwave power generated in the structure is extracted into broad wall coupled waveguides at the top and bottom of the NIMW. Microwave power travels down both directions and is absorbed in a perfectly matched layer (PML).

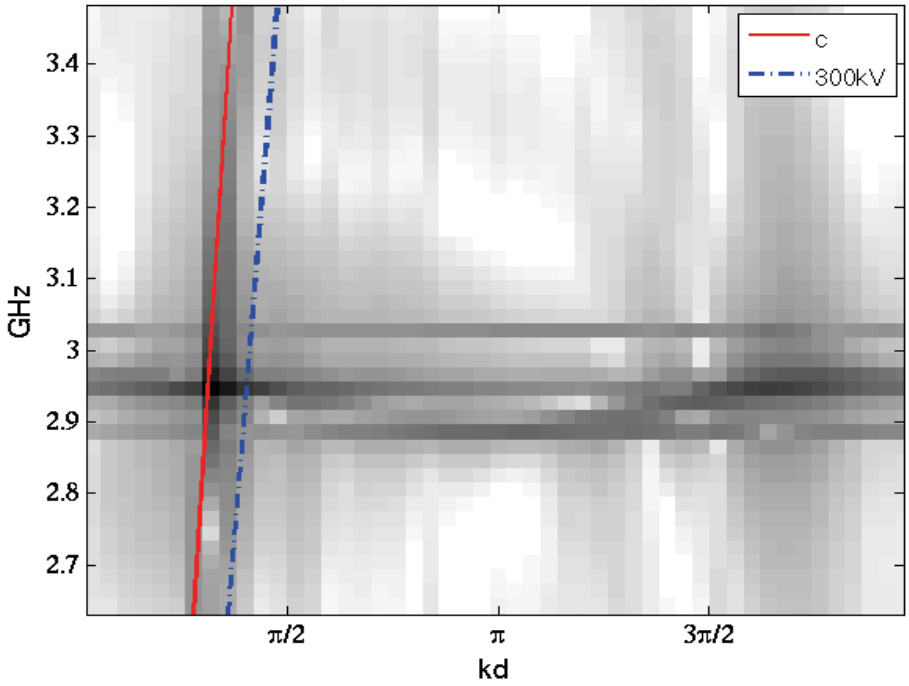

Figure 32: Dispersion relation measured in ICEPIC for the two CSRR plate configuration, similar to the rendering seen in Fig. 31.

The corresponding dispersion relation is shown in Fig. 32. The red line represents the light line and the blue line is a 300 kV beamline. This intersection with the cold structure mode occurs at approximately 2.9 GHz. Since $d\omega/dk < 0$, the mode of interest is indeed a backward wave mode indicating NI behavior. Fig. 33 shows the forward and backward power (see inset of Fig. 33) in the waveguide and the frequency of oscillation

around 2.9 GHz as expected from the dispersion relation. This simulation corresponds to a cavity with two CSRRs in its width. The majority of the power travels backwards out of the waveguides. The output power is around 2 MW for an input power of 15 MW representing an electronic efficiency of approximately 13%. Optimization of this structutre is expected to significantly increase the efficiency.

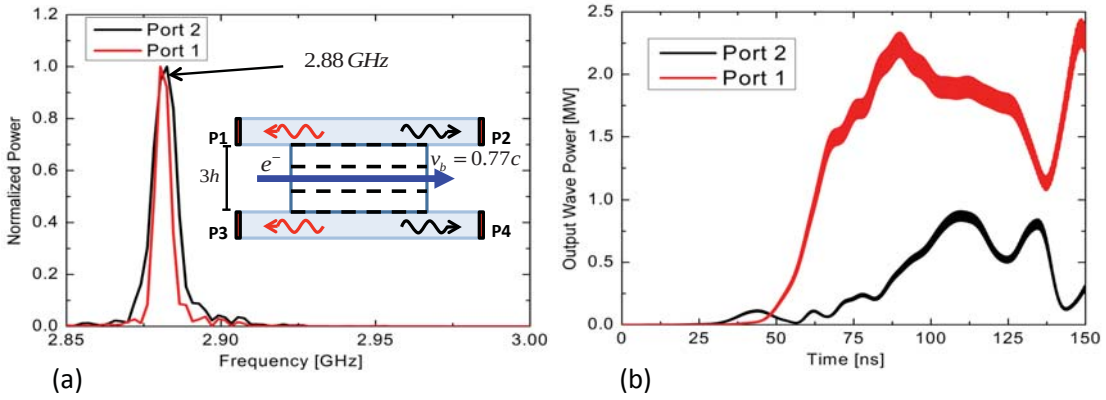

Figure 33: Electron beam coupling to patterned, CSRR metamaterial. (a) Extracted frequency response from output waveguides for 150 kV beam voltage. Four CSRR plates, each with six unite cells, were embedded within a waveguide (shown in inset). (b) Output time domain power levels for the described geometry.

Chapter 3 Angular-Momentum-Biasing Metamaterials

3.1 Coupled-Mode Theory for Temporally Modulated, Coupled Resonator Loops

Non-reciprocal components, essential parts of modern communication systems, are today almost exclusively based on magneto-optical materials, severely limiting their integration and wide applicability. A practical and inexpensive route to magnetic-free non-reciprocity may revolutionize radio-frequency and nanophotonic communication networks. Among the available approaches in this direction [30]-[51], angular-momentum biasing was recently proposed to realize isolation for sound waves traveling in a rotating medium [52], and envisioned as a path towards compact, linear integrated non-reciprocal electromagnetic components [51],[67]. Inspired by this concept, in this and the following chapters we demonstrate a route towards deeply sub-wavelength, magnetic-free, linear radio-frequency non-reciprocal components based on parametric modulation of three identical, strongly and symmetrically coupled resonators. Their resonant frequencies are modulated by external signals with same amplitude and a relative phase difference of 120°, imparting an effective electronic angular momentum to the system. We observe giant non-reciprocity, with large magnitude difference in transmission for opposite directions, in a deeply subwavelength, linear, noise-free device.

---

[75] Authors: N.A. Estep, D.L. Sounas, J. Soric, and A. Alù.
Author Contributions: N.A.E. performed the experiment, D.L.S. and N.A.E. designed the structure and conducted the numerical calculations and theoretical modelling. J.S. helped in the selection and modelling of the modulation varactors. A.A. directed and supervised the work.

In addition, the device topology is tunable in real-time, and can be directly embedded in a conventional integrated circuit.

Early attempts to realize magnetic-free non-reciprocity were based on the non-reciprocal properties of transistors at microwave frequencies [30], and on networks of electro-optical modulators at optical frequencies [47]-[49]. However, such approaches traded the absence of magnetic bias with other significant drawbacks, such as the strong non-linearities and poor noise-performance of transistors, or the large size and complexity of the required electro-optical networks. More recently, non-reciprocity has been achieved in transistor-loaded metamaterials [32]-[35] and non-linear devices [40],[68],[69]. Also these solutions impose severe restrictions on the input power levels, generally degrading the signal quality because of noise or signal distortions. Another interesting approach to magnetic-free non-reciprocity has been introduced in [41], using asymmetric mode conversion in spatiotemporally-modulated waveguides. This concept is especially attractive for integrated optical networks, as it may be fully realized in silicon photonics [44]. However, this technique and its variants [42]-[46],[70],[71] lead to structures much larger than the wavelength, due to the weak electro-optic or acousto-optic effects on which they rely, and require complex modulation schemes. In a similar context, [72] theoretically explored the concept of a non-reciprocal device based on parametrically-coupled resonators.

An approach that can lead to compact, magnetic-free non-reciprocal devices with relaxed implementation complexity was recently introduced in [51],[52],[67], based on angular momentum biasing of a resonant ring. Angular momentum can be applied either by mechanically spinning a fluid, as proven for acoustic waves [52], or, more

conveniently for electromagnetic waves, by spatiotemporal modulation with a traveling wave, realizing an effective electronic spin [51],[67], as illustrated in Fig. 3(b). The resonant nature of the modulated ring can dramatically boost the otherwise weak electro-optic effects through which spatiotemporal modulation is typically achieved [73],[74], allowing the design of largely non-reciprocal devices with dimensions in the order of, or even smaller, than the wavelength. Furthermore, in contrast to other approaches based on spatiotemporal modulation [41],[45], angular-momentum biasing is based on uniform modulation across the ring cross-section, thus significantly simplifying the fabrication process.

In practice, consider the spatiotemporal modulation of a ring resonator, which may be efficiently imparted in a discrete fashion via a number of different regions with uniform modulation [67]. Such a discretization results in a reduction of the modulation efficiency by a factor $\mathrm{sinc}(2l/N)$ for N modulation regions, revealing a trade-off between performance and fabrication complexity. To avoid this problem, Ref. [75] introduced a new design based on three identical resonators symmetrically coupled to each other and modulated by signals with the same amplitude and phase difference of $120°$ [Fig. 34]. In this particular design, non-reciprocity is the result of lifting the degeneracy of the counter-rotating modes of the *composite loop*, as opposed to lifting the degeneracy of the modes of a single ring, as in [51]. Since the modulation of each resonator in the loop is uniform, the modulation efficiency of this structure can reach 100%.

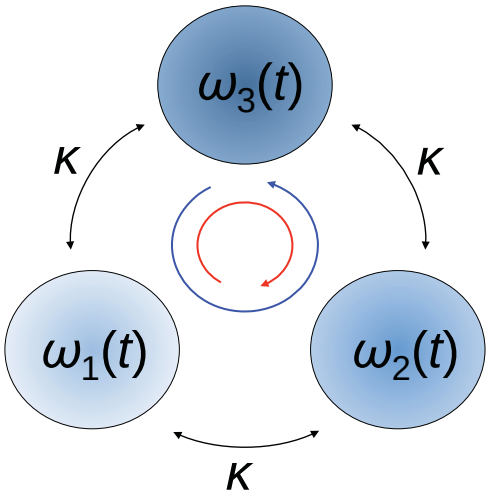

Figure 34: Angular-momentum non-reciprocity with a loop of identical resonators symmetrically coupled to each other [29]. Angular momentum is effectively applied to the loop by modulating the resonators with signals with equal amplitudes and phase difference of 120 deg. Modulation lifts the degeneracy of the counter-rotating modes of the *loop*, as opposed to the counter-rotating states of a *single ring*, as in Fig. 3(b).

The design in [75] was based on a heuristic empirical approach and, although it provided large isolation, it exhibited quite large insertion loss and intermodulation products. In the following, by using coupled-mode theory we develop a rigorous theory, which allows designing circulators with optimum characteristics in terms of isolation, insertion loss and intermodulation products. The designs are based on wye resonators, which are easier to realize than the ring resonator in [75], and also exhibit significantly improved performance. The analysis in the section follows the $e^{-i\omega t}$ harmonic convention and simulations are performed with CST Microwave Studio and Advanced Design Studio.

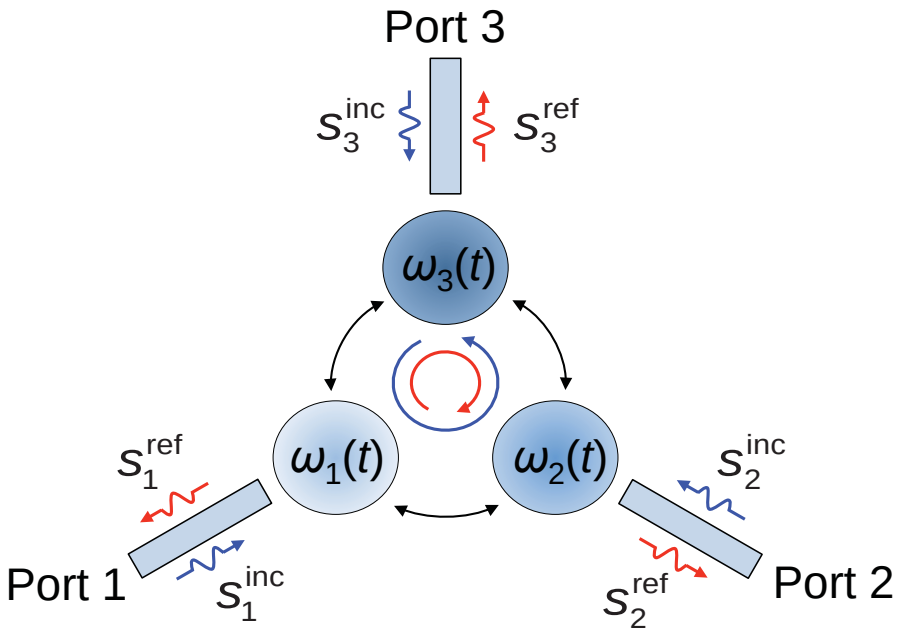

Figure 35: Circulator based on a spatiotemporally modulated loop of coupled resonators, where the resonators are additionally coupled to external transmission lines [29].

Fig. 35 illustrates the most general form of a circulator based on a loop of modulated resonators: it consists of three identical modulated resonators, symmetrically coupled to each other and to three external transmission lines. Networks of coupled resonators can be efficiently studied via coupled-mode theory [76], which, when applied to the network in Fig. 35, yields

$$\begin{aligned} \dot{\mathbf{a}} &= (-i\boldsymbol{\Omega} - \boldsymbol{\Gamma})\mathbf{a} + \mathbf{D}^{\mathrm{T}}\mathbf{s}^{\mathrm{inc}}, \\ \mathbf{s}^{\mathrm{ref}} &= \mathbf{C}\mathbf{s}^{\mathrm{inc}} + \mathbf{D}\mathbf{a}. \end{aligned} \tag{3.1.1}$$

In the above equation, $\mathbf{a} = (a_1 \quad a_2 \quad a_3)^{\mathrm{T}}$ is the state vector, $\boldsymbol{\Omega}$ is the frequency matrix, $\boldsymbol{\Gamma}$ is the decay matrix, $\mathbf{s}^{\mathrm{inc}} = (s_1^{\mathrm{inc}} \quad s_2^{\mathrm{inc}} \quad s_3^{\mathrm{inc}})^{\mathrm{T}}$ is the incident-signal vector, $\mathbf{D}$ is the coupling matrix between the lines and the resonators, $\mathbf{s}^{\mathrm{ref}} = (s_1^{\mathrm{ref}} \quad s_2^{\mathrm{ref}} \quad s_3^{\mathrm{ref}})^{\mathrm{T}}$ is the reflected-signal vector and $\mathbf{C}$ is the matrix describing immediate coupling between $\mathbf{s}^{\mathrm{inc}}$ and $\mathbf{s}^{\mathrm{ref}}$. Since the resonators are identical and the coupling between them is symmetrical, $\boldsymbol{\Omega}$, $\boldsymbol{\Gamma}$ and $\mathbf{D}$ are symmetrical as well:

$$\boldsymbol{\Omega} = \begin{pmatrix} \omega_0 & \kappa & \kappa \\ \kappa & \omega_0 & \kappa \\ \kappa & \kappa & \omega_0 \end{pmatrix}, \quad \boldsymbol{\Gamma} = \begin{pmatrix} \gamma & \zeta & \zeta \\ \zeta & \gamma & \zeta \\ \zeta & \zeta & \gamma \end{pmatrix}, \quad \mathbf{D} = \begin{pmatrix} d & g & g \\ g & d & g \\ g & g & d \end{pmatrix}. \tag{3.1.2}$$

The diagonal elements of these matrices refer to isolated resonators, while the off-diagonal elements describe the effect of coupling. In general, $\boldsymbol{\Gamma}$ consists of two parts, $\boldsymbol{\Gamma}_{\mathrm{loss}}$ and $\boldsymbol{\Gamma}_{\mathrm{cpl}}$ corresponding to thermal loss and leakage to the external lines, respectively. Furthermore, $\mathbf{D}^{\mathrm{H}}\mathbf{D} = 2\boldsymbol{\Gamma}_{\mathrm{cpl}}$ and $\mathbf{C}\mathbf{D}^{*} = -\mathbf{D}$, resulting from power conservation and time-reversal symmetry. Assuming that $\mathbf{C}$ is a diagonal matrix, i.e., there is no direct coupling among different lines, and selecting the reference planes of the external lines so that the diagonal elements of $\mathbf{D}$ are real, $\mathbf{C} = -\mathbf{I}_3$, where $\mathbf{I}_3$ is the 3×3 identity matrix, implying that, if the resonators are not excited ($\mathbf{a} = 0$), all the incident power is reflected.

Modulation is applied to the resonators as $\omega_1(t) = \omega_0 + \delta\omega_{\mathrm{m}} \cos(\omega_{\mathrm{m}} t)$, $\omega_2(t) = \omega_0 + \delta\omega_{\mathrm{m}} \cos(\omega_{\mathrm{m}} t - 2\pi/3)$ and $\omega_3(t) = \omega_0 + \delta\omega_{\mathrm{m}} \cos(\omega_{\mathrm{m}} t - 4\pi/3)$, where $\delta\omega_{\mathrm{m}}$ is the magnitude of the frequency perturbation and ω_{m} is the modulation frequency. This form of modulation imparts an effective electric rotation to the loop of coupled

resonators, as discussed in the Introduction. Then, $\mathbf{\Omega} = \mathbf{\Omega}_0 + \delta\mathbf{\Omega}_\mathrm{m}$, where $\mathbf{\Omega}_0$ is the static part of the modulation matrix as given in (3.1.2) and

$$\delta\mathbf{\Omega}_\mathrm{m} = \delta\omega_\mathrm{m}\begin{pmatrix}\cos(\omega_\mathrm{m}t) & 0 & 0\\ 0 & \cos(\omega_\mathrm{m}t+2\pi/3) & 0\\ 0 & 0 & \cos(\omega_\mathrm{m}t+4\pi/3)\end{pmatrix}. \tag{3.1.3}$$

Since modulation is a perturbation of the static (non-modulated) loop, it is convenient to express (3.1.1) in the eigenbasis of the static loop (eigenbasis of $\mathbf{\Omega}_0$), which consists of a common state with frequency $\omega_\mathrm{c} = \omega_0 - 2\kappa$ and state vector $\mathbf{a}_\mathrm{c} = (1 \quad 1 \quad 1)^\mathrm{T}/\sqrt{3}$, a right-handed state with frequency $\omega_+ = \omega_0 + \kappa$ and state vector $\mathbf{a}_+ = (1 \quad e^{i2\pi/3} \quad e^{i4\pi/3})^\mathrm{T}/\sqrt{3}$, and a left-handed state with same resonance frequency $\omega_- = \omega_+ = \omega_0 + \kappa$, and state vector $\mathbf{a}_- = (1 \quad e^{-i2\pi/3} \quad e^{-i4\pi/3})^\mathrm{T}/\sqrt{3}$. The transformation from the eigenbasis of the separate resonators to the eigenbasis of the loop reads $\bar{\mathbf{a}} = \mathbf{U}^{-1}\mathbf{a}$, where $\bar{\mathbf{a}}$ is the state vector in the eigenbasis of the loop and $\mathbf{U} = (\mathbf{a}_\mathrm{c} \quad \mathbf{a}_+ \quad \mathbf{a}_-)$. Then, (3.1.1) becomes

$$\begin{aligned}\dot{\bar{\mathbf{a}}} &= (-i\bar{\mathbf{\Omega}} - \bar{\mathbf{\Gamma}})\bar{\mathbf{a}} + \bar{\mathbf{D}}^*\mathbf{s}^\mathrm{inc},\\ \mathbf{s}^\mathrm{ref} &= \bar{\mathbf{C}}\mathbf{s}^\mathrm{inc} + \bar{\mathbf{D}}\bar{\mathbf{a}},\end{aligned} \tag{3.1.4}$$

where

$$\bar{\mathbf{\Omega}} = \mathbf{U}^\mathrm{H}\mathbf{\Omega}\mathbf{U} = \underbrace{\begin{pmatrix}\omega_\mathrm{c} & 0 & 0\\ 0 & \omega_+ & 0\\ 0 & 0 & \omega_-\end{pmatrix}}_{\bar{\mathbf{\Omega}}_0} + \underbrace{\frac{\delta\omega_\mathrm{m}}{2}\begin{pmatrix}0 & e^{-i\omega_\mathrm{m}t} & e^{i\omega_\mathrm{m}t}\\ e^{i\omega_\mathrm{m}t} & 0 & e^{-i\omega_\mathrm{m}t}\\ e^{-i\omega_\mathrm{m}t} & e^{i\omega_\mathrm{m}t} & 0\end{pmatrix}}_{\delta\bar{\mathbf{\Omega}}_\mathrm{m}}, \tag{3.1.5}$$

$$\bar{\boldsymbol{\Gamma}} = \mathbf{U}^{\mathrm{H}}\boldsymbol{\Gamma}\mathbf{U} = \begin{pmatrix} \gamma_{\mathrm{c}} & 0 & 0 \\ 0 & \gamma_{+} & 0 \\ 0 & 0 & \gamma_{-} \end{pmatrix}, \tag{3.1.6}$$

$$\bar{\mathbf{D}} = \mathbf{D}\mathbf{U} = \begin{pmatrix} d_{\mathrm{c}} & d_{+} & d_{-} \\ d_{c} & d_{+}e^{i2\pi/3} & d_{-}e^{-i2\pi/3} \\ d_{c} & d_{+}e^{i4\pi/3} & d_{-}e^{-i4\pi/3} \end{pmatrix}. \tag{3.1.7}$$

In the above equations, $\gamma_{\mathrm{c}} = \gamma + 2\zeta$ and $\gamma_{+} = \gamma_{-} = \gamma - \zeta$ are the decay rates of the common and rotating modes, respectively, while $d_{\mathrm{c}} = d + 2g$ and $d_{+} = d_{-} = d - g$ are the coupling coefficients between the lines and these modes. Equation $\mathbf{D}^{\mathrm{H}}\mathbf{D} = 2\boldsymbol{\Gamma}_{\mathrm{cpl}}$ is form-invariant under this transformation, yielding $d_{\mathrm{c}} = \sqrt{2\gamma_{\mathrm{c,cpl}}/3}$ and $d_{+} = d_{-} = \sqrt{2\gamma_{+,\mathrm{cpl}}/3} = \sqrt{2\gamma_{-,\mathrm{cpl}}/3}$, where $\gamma_{\mathrm{c,cpl}}$, $\gamma_{+,\mathrm{cpl}}$ and $\gamma_{-,\mathrm{cpl}}$ are the parts of γ_{c}, γ_{+} and γ_{-} referring to leakage to the external lines. In the eigenbasis of the static loop, the state vectors of the common, right-handed and left-handed eigenstates become $\bar{\mathbf{a}}_{\mathrm{c}} = (1 \quad 0 \quad 0)^{\mathrm{T}}$, $\bar{\mathbf{a}}_{+} = (0 \quad 1 \quad 0)^{\mathrm{T}}$ and $\bar{\mathbf{a}}_{-} = (0 \quad 0 \quad 1)^{\mathrm{T}}$, respectively.

Before solving the source-driven problem (3.1.4), it is important to study the eigenstates of the modulated loop. For simplicity of analysis, we assume $\bar{\boldsymbol{\Gamma}} = 0$, *i.e.*, no loss and no coupling to external lines. The eigen-states of the modulated loop in Fig. 35 are calculated from (3.1.4) for $\bar{\boldsymbol{\Gamma}} = 0$ (no loss) and $\mathbf{s}^{\mathrm{inc}} = 0$.

To solve this equation, we ignore the coupling between the common and rotating states. The results so obtained are shown to be accurate up to the order $\delta\omega_{\mathrm{m}}^{2}$, provided that $\omega_{\mathrm{m}} \ll \left|\omega_{\mathrm{c}} - \omega_{\pm}\right|$. The coupling between the common and rotating states is due to the first column and the first row of $\delta\bar{\boldsymbol{\Omega}}_{\mathrm{m}}$. Taking these elements to be equal to zero, (3.1.4) becomes

$$\begin{aligned}
\dot{\tilde{a}}_{\mathrm{c}} &= -i\omega_{\mathrm{c}}\tilde{a}_{\mathrm{c}}, \\
\dot{\tilde{a}}_{+} &= -i\omega_{+}\tilde{a}_{+} - i\frac{\delta\omega_{\mathrm{m}}}{2}e^{-i\omega_{\mathrm{m}}t}\tilde{a}_{-}, \\
\dot{\tilde{a}}_{-} &= -i\omega_{-}\tilde{a}_{-} - i\frac{\delta\omega_{\mathrm{m}}}{2}e^{i\omega_{\mathrm{m}}t}\tilde{a}_{+},
\end{aligned} \tag{3.1.8}$$

where the "tilde" is used to distinguish the approximate solution from the exact one. The solution of the first of these equations is obviously $\tilde{a}_{\mathrm{c}} = A_{\mathrm{c}}e^{-i\omega_{\mathrm{c}}t}$, where A_{c} is a complex number. The solution of the other two equations can be found by assuming $\tilde{a}_{+} = A_{+}e^{-i\omega t}$ and $\tilde{a}_{-} = A_{-}e^{-i(\omega-\omega_{\mathrm{m}})t}$. Then, (3.1.8) becomes

$$\begin{pmatrix} \omega_{+} & \delta\omega_{\mathrm{m}}/2 \\ \delta\omega_{\mathrm{m}}/2 & \omega_{+}+\omega_{\mathrm{m}} \end{pmatrix}\begin{pmatrix} A_{+} \\ A_{-} \end{pmatrix} = \omega\begin{pmatrix} A_{+} \\ A_{-} \end{pmatrix}, \tag{3.1.9}$$

which is a typical eigenvalue problem with eigenvalues $\omega_{\mathrm{m}+} = \omega_{+} - \Delta\omega/2$ and $\omega_{\mathrm{m}-} = \omega_{+} + \Delta\omega/2 + \omega_{\mathrm{m}}$, and corresponding eigenvectors $\mathbf{A}_{\mathrm{m}+} = (1 \quad -\Delta\omega/\delta\omega_{\mathrm{m}})^{\mathrm{T}}$ and $\mathbf{A}_{\mathrm{m}-} = (\Delta\omega/\delta\omega_{\mathrm{m}} \quad 1)^{\mathrm{T}}$, where $\Delta\omega = \sqrt{\omega_{\mathrm{m}}^2 + \delta\omega_{\mathrm{m}}^2} - \omega_{\mathrm{m}}$. The corresponding solutions of (3.1.8) read

$$\tilde{\mathbf{a}}_{\mathrm{mc}} = \begin{pmatrix} 1 \\ 0 \\ 0 \end{pmatrix}e^{-i\omega_{\mathrm{c}}t}, \quad \tilde{\mathbf{a}}_{\mathrm{m}+} = \frac{1}{\sqrt{\Delta}}\begin{pmatrix} 0 \\ 1 \\ -\frac{\Delta\omega}{\delta\omega_{\mathrm{m}}}e^{i\omega_{\mathrm{m}}t} \end{pmatrix}e^{-i\omega_{\mathrm{m}+}t}, \quad \tilde{\mathbf{a}}_{\mathrm{m}-} = \frac{1}{\sqrt{\Delta}}\begin{pmatrix} 0 \\ \frac{\Delta\omega}{\delta\omega_{\mathrm{m}}}e^{-i\omega_{\mathrm{m}}t} \\ 1 \end{pmatrix}e^{-i\omega_{\mathrm{m}-}t}, \tag{3.1.10}$$

where $\Delta = 1 + (\Delta\omega/\delta\omega_{\mathrm{m}})^2$.

Next, we transform (3.1.4) in the basis defined by (3.1.10) via $\bar{\mathbf{a}} = \mathbf{V}\hat{\mathbf{a}}$, where

$$\mathbf{V}=\frac{1}{\sqrt{\Delta}}\begin{pmatrix}\sqrt{\Delta} & 0 & 0\\ 0 & 1 & \frac{\Delta\omega}{\delta\omega_{\mathrm{m}}}e^{-i\omega_{\mathrm{m}}t}\\ 0 & -\frac{\Delta\omega}{\delta\omega_{\mathrm{m}}}e^{i\omega_{\mathrm{m}}t} & 1\end{pmatrix}. \tag{3.1.11}$$

in particular,

$$\dot{\hat{\mathbf{a}}}=-i\hat{\mathbf{\Omega}}\hat{\mathbf{a}}, \tag{3.1.12}$$

where $\hat{\mathbf{\Omega}}=\mathbf{V}^{\mathrm{H}}\bar{\mathbf{\Omega}}\mathbf{V}-i\mathbf{V}^{\mathrm{H}}\dot{\mathbf{V}}$. After straightforward but lengthy manipulations, we find

$$\hat{\mathbf{\Omega}}=\hat{\mathbf{\Omega}}_0+\delta\omega_1\begin{pmatrix}0 & e^{-i\omega_{\mathrm{m}}t} & e^{i\omega_{\mathrm{m}}t}\\ e^{i\omega_{\mathrm{m}}t} & 0 & 0\\ e^{-i\omega_{\mathrm{m}}t} & 0 & 0\end{pmatrix}+\delta\omega_2\begin{pmatrix}0 & e^{i2\omega_{\mathrm{m}}t} & e^{-i2\omega_{\mathrm{m}}t}\\ e^{-i2\omega_{\mathrm{m}}t} & 0 & 0\\ e^{i2\omega_{\mathrm{m}}t} & 0 & 0\end{pmatrix}, \tag{3.1.13}$$

where $\hat{\mathbf{\Omega}}_0=\mathrm{diag}\{\omega_{\mathrm{c}},\omega_{\mathrm{m}+},\omega_{\mathrm{m}-}\}$ and

$$\begin{aligned}\delta\omega_1&=\frac{\delta\omega_{\mathrm{m}}^2}{2\sqrt{2}\sqrt{\delta\omega_{\mathrm{m}}^2-\omega_{\mathrm{m}}\Delta\omega}},\\ \delta\omega_2&=-\frac{\delta\omega_{\mathrm{m}}\Delta\omega}{2\sqrt{2}\sqrt{\delta\omega_{\mathrm{m}}^2-\omega_{\mathrm{m}}\Delta\omega}}.\end{aligned} \tag{3.1.14}$$

The matrix $\hat{\mathbf{\Omega}}$ is time-periodic with periodicity $T_{\mathrm{m}}=2\pi/\omega_{\mathrm{m}}$. Therefore, according to Floquet theorem, the solution of (3.1.12) can be expressed as

$$\hat{\mathbf{a}}=\sum_{n=-\infty}^{\infty}\hat{\mathbf{a}}_{\mathrm{n}}e^{-i(\omega+n\omega_{\mathrm{m}})t}, \tag{3.1.15}$$

where $\hat{\mathbf{a}}_n$ is the state vector of the n-th Floquet harmonic. In the Floquet space, (3.1.12) is transformed to the regular infinite eigenvalue problem

$$\hat{\mathbf{\Omega}}_{\mathrm{F}}\hat{\mathbf{a}}_{\mathrm{F}} = \omega\hat{\mathbf{a}}_{\mathrm{F}}, \tag{3.1.16}$$

where $\hat{\mathbf{a}}_{\mathrm{F}} = (\cdots \quad \hat{\mathbf{a}}_{-1}^{\mathrm{T}} \quad \hat{\mathbf{a}}_0^{\mathrm{T}} \quad \hat{\mathbf{a}}_1^{\mathrm{T}} \quad \cdots)^{\mathrm{T}}$ and $\hat{\mathbf{\Omega}}_{\mathrm{F}}$ is the matrix whose (m,n) block relating $\hat{\mathbf{a}}_m$ with $\hat{\mathbf{a}}_n$ reads

$$\hat{\mathbf{\Omega}}_{\mathrm{F},mn} = (\hat{\mathbf{\Omega}}_0 - m\omega_{\mathrm{m}})\delta_{mn} + \delta\omega_1(\hat{\mathbf{\Omega}}_1\delta_{m,n+1} + \hat{\mathbf{\Omega}}_{-1}\delta_{m,n-1}) + \delta\omega_2(\hat{\mathbf{\Omega}}_2\delta_{m,n+2} + \hat{\mathbf{\Omega}}_{-2}\delta_{m,n-2}), \tag{3.1.17}$$

where

$$\hat{\mathbf{\Omega}}_1 = \hat{\mathbf{\Omega}}_{-2} = \begin{pmatrix} 0 & 1 & 0 \\ 0 & 0 & 0 \\ 1 & 0 & 0 \end{pmatrix}, \quad \hat{\mathbf{\Omega}}_{-1} = \hat{\mathbf{\Omega}}_2 = \begin{pmatrix} 0 & 0 & 1 \\ 1 & 0 & 0 \\ 0 & 0 & 0 \end{pmatrix}. \tag{3.1.18}$$

A pictorial representation of $\hat{\mathbf{\Omega}}_{\mathrm{F}}$ is provided in Fig. 36.

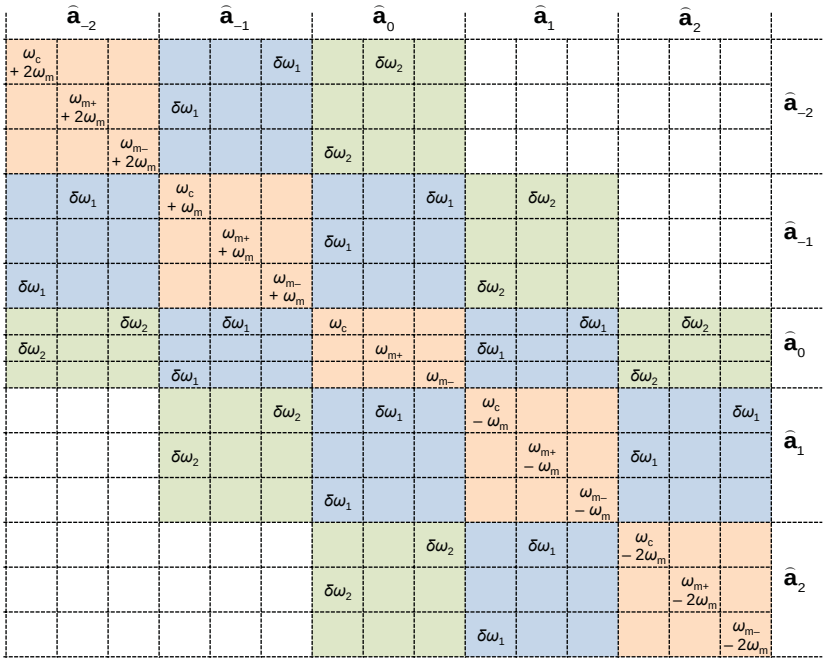

Figure 36: Matrix $\widehat{\mathbf{\Omega}}_{\mathrm{F}}$ in (3.1.17). All the blank locations correspond to zero elements [29].

The matrix $\widehat{\mathbf{\Omega}}_{\mathrm{F}}$ does not have degenerate terms in the main diagonal and, as a result, conventional perturbation theory can be applied on (3.1.16) [77]. For example, the first-order correction to eigenvalue $\omega_{\mathrm{m}+}$ is given by $\delta\omega_{\mathrm{m}+}^{(1)} = (\hat{\mathbf{a}}_{\mathrm{F}+,0}, \delta\widehat{\mathbf{\Omega}}_{\mathrm{F}}\hat{\mathbf{a}}_{\mathrm{F}+,0})$, where $\delta\widehat{\mathbf{\Omega}}_{\mathrm{F}}$ is the off-diagonal part of $\widehat{\mathbf{\Omega}}_{\mathrm{F}}$, $\hat{\mathbf{a}}_{\mathrm{F}+,0}$ is the Floquet vector with the "+" element of the 0-th harmonic equal to unity and all other elements equal to zero, and $(\mathbf{u},\mathbf{v}) = \mathbf{u}^{\mathrm{T}}\mathbf{v}$. It is not difficult to show that $\delta\omega_{\mathrm{m}+}^{(1)} = 0$. Similarly, the second-order correction to $\omega_{\mathrm{m}+}$ can be calculated from

$$\delta\omega_{\mathrm{m}+}^{(2)} = \sum_{i,j\in\{\mathrm{c},+,-\}} \sum_{m\neq n} \frac{\left|(\hat{\mathbf{a}}_{\mathrm{F}i,m}, \delta\widehat{\mathbf{\Omega}}_{\mathrm{F}}\hat{\mathbf{a}}_{\mathrm{F}i,n})\right|^2}{\omega_{\mathrm{m}j} - \omega_{\mathrm{m}i} + (n-m)\omega_{\mathrm{m}}}, \tag{3.1.19}$$

where $\widehat{\mathbf{a}}_{\mathrm{F}i,n}$ is the Floquet vector with the *i*-th element of the *n*-th harmonic equal to one and all other elements equal to zero. Substituting (3.1.17) into (3.1.19) yields

$$\delta\omega_{\mathrm{m}+}^{(2)} = \frac{\delta\omega_{\mathrm{l}}^2}{\omega_{\mathrm{c}} - \omega_{\mathrm{m}+} - \omega_{\mathrm{m}}} + \frac{\delta\omega_2^2}{2\omega_{\mathrm{m}}}. \tag{3.1.20}$$

By taking the limit $\delta\omega_{\mathrm{m}} \to 0$ in (3.1.14), it can be shown that $\delta\omega_{\mathrm{l}} = \delta\omega_{\mathrm{m}}/2 + O(\delta\omega_{\mathrm{m}}^3)$ and $\delta\omega_2 = \delta\omega_{\mathrm{m}}^2/(4\omega_{\mathrm{m}}) + O(\delta\omega_{\mathrm{m}}^4)$. Therefore, if in addition $\omega_{\mathrm{m}} \ll |\omega_{\mathrm{c}} - \omega_{\mathrm{m}+}|$, $\delta\omega_{\mathrm{m}+}^{(1)} = O(\delta\omega_{\mathrm{m}}^2)$. Following a similar analysis, it can be shown that the corrections to $\omega_{\mathrm{m}-}$ and ω_{c} are also $O(\delta\omega_{\mathrm{m}}^2)$, while the correction to the corresponding eigenvectors are $O(\delta\omega_{\mathrm{m}})$. Therefore, (3.1.10) are solutions of (3.1.4) to the order $O(\delta\omega_{\mathrm{m}})$.

Therefore, under these conditions, and for $\omega_{\mathrm{m}} \ll |\omega_{\mathrm{c}} - \omega_{+}|$, the states of the modulated loop read

$$\begin{aligned}
\overline{\mathbf{a}}_{\mathrm{mc}} &= \overline{\mathbf{a}}_{\mathrm{c}} e^{-i\omega_{\mathrm{mc}}t} + O(\delta\omega_{\mathrm{m}}), \\
\overline{\mathbf{a}}_{\mathrm{m}+} &= \overline{\mathbf{a}}_{+} e^{-i\omega_{\mathrm{m}+}t} - \frac{\Delta\omega}{\delta\omega_{\mathrm{m}}} \overline{\mathbf{a}}_{-} e^{-i(\omega_{\mathrm{m}+} - \omega_{\mathrm{m}})t} + O(\delta\omega_{\mathrm{m}}), \\
\overline{\mathbf{a}}_{\mathrm{m}-} &= \overline{\mathbf{a}}_{-} e^{-i\omega_{\mathrm{m}-}t} + \frac{\Delta\omega}{\delta\omega_{\mathrm{m}}} \overline{\mathbf{a}}_{+} e^{-i(\omega_{\mathrm{m}-} + \omega_{\mathrm{m}})t} + O(\delta\omega_{\mathrm{m}}),
\end{aligned} \tag{3.1.21}$$

where

$$\begin{aligned}
\omega_{\mathrm{mc}} &= \omega_{\mathrm{c}}, \\
\omega_{\mathrm{m}+} &= \omega_{+} - \frac{\Delta\omega}{2}, \\
\omega_{\mathrm{m}-} &= \omega_{-} + \frac{\Delta\omega}{2},
\end{aligned} \tag{3.1.22}$$

and $\Delta\omega = \sqrt{\omega_{\mathrm{m}}^2 + \delta\omega_{\mathrm{m}}^2} - \omega_{\mathrm{m}}$. Modulation affects the common state very little, as expected from the fact that $\omega_{\mathrm{m}} \ll \left|\omega_{\mathrm{c}} - \omega_{+}\right|$. On the other hand, it significantly affects the rotating states, resulting in two new quasi-rotating states, $\bar{\mathbf{a}}_{\mathrm{m}\pm}$, consisting of the rotating ones with different amplitudes and frequencies separated by ω_{m}, as illustrated in Fig. 37. The quasi-rotating states are separated from each other by $\Delta\omega$, an effect that resembles frequency-splitting of counter-polarized waves in magnetized ferrites and, therefore, it provides a direct evidence of the non-reciprocal properties of the modulated loop.

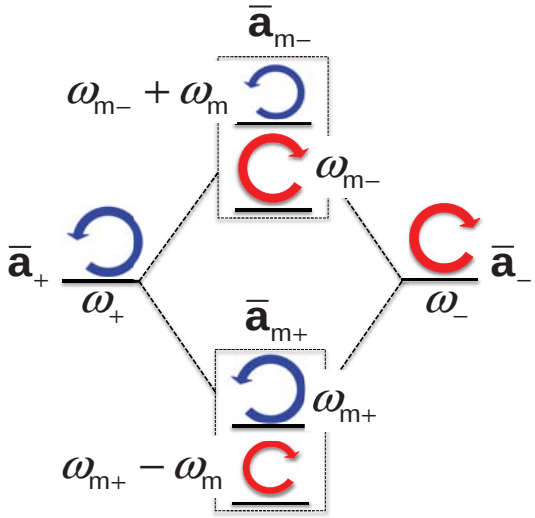

Figure 37: Frequency diagram for the spatiotemporally-modulated loop of coupled resonators [29]. Without modulation, the loop supports degenerate counter-rotating states $\bar{\mathbf{a}}_{\pm}$ (left- and right-hand side). Modulation mixes these states, producing the hybrid states $\bar{\mathbf{a}}_{\mathrm{m}\pm}$ (center), which consist of the rotating states at frequency levels separated by ω_{m}. Each of the hybrid states is dominated by one of the rotating states, making the hybrid states quasi-rotating. The quasi-rotating states exist at different frequency levels ($\omega_{\mathrm{m}\pm}$), which is a direct evidence that the modulated loop is non-reciprocal.

Neglecting the common mode, which is minimally affected by the modulation, (3.1.4) becomes

$$\begin{aligned}\dot{a}_+ &= (-i\omega_+ - \gamma_+)a_+ - i\frac{\delta\omega_{\mathrm{m}}}{2}e^{-i\omega_{\mathrm{m}}t}a_- + \mathbf{k}_+\mathbf{s}^{\mathrm{inc}},\\ \dot{a}_- &= (-i\omega_- - \gamma_-)a_- - i\frac{\delta\omega_{\mathrm{m}}}{2}e^{i\omega_{\mathrm{m}}t}a_+ + \mathbf{k}_-\mathbf{s}^{\mathrm{inc}},\end{aligned} \tag{3.1.23}$$

where a_+ and a_- are the complex amplitudes of the right- and left-handed modes of the loop, $\mathbf{k}_+ = d_+(1 \quad e^{-i2\pi/3} \quad e^{-i4\pi/3})$ and $\mathbf{k}_- = d_-(1 \quad e^{i2\pi/3} \quad e^{i4\pi/3})$. (3.1.23) can be solved by assuming

$$\begin{aligned}a_+ &= a_+^{(0)}e^{-i\omega t} + a_+^{(+1)}e^{-i(\omega+\omega_{\mathrm{m}})t},\\ a_- &= a_-^{(-1)}e^{-i(\omega-\omega_{\mathrm{m}})t} + a_-^{(0)}e^{-i\omega t},\end{aligned} \tag{3.1.24}$$

where ω is the frequency of the incoming signal, $a_\pm^{(0)}$ are the amplitudes of the dominant sub-states and $a_\pm^{(\pm1)}$ the amplitudes of the secondary ones. For excitation from port 1, these amplitudes are found by substituting (3.1.24) into (3.1.23) as

$$\begin{aligned}a_\pm^{(0)} &= d_+\frac{-i(\omega-\omega_+\mp\omega_{\mathrm{m}})+\gamma_+}{[-i(\omega-\omega_+)+\gamma_+][-i(\omega-\omega_+\mp\omega_{\mathrm{m}})+\gamma_+]+\delta\omega_{\mathrm{m}}^2/4},\\ a_\pm^{(\pm1)} &= d_+\frac{-i\,\delta\omega_{\mathrm{m}}/2}{[-i(\omega-\omega_+)+\gamma_+][-i(\omega-\omega_+\mp\omega_{\mathrm{m}})+\gamma_+]+\delta\omega_{\mathrm{m}}^2/4}.\end{aligned} \tag{3.1.25}$$

Transmission to ports 2 and 3 can be calculated by substituting (3.1.24) into the second equation of (3.1.4) as

$$
\begin{aligned}
S_{11}(\omega) &= -1 + d_+\left[a_+^{(0)} + a_-^{(0)}\right], \\
S_{21}(\omega) &= d_+\left[a_+^{(0)} e^{i2\pi/3} + a_-^{(0)} e^{-i2\pi/3}\right], \\
S_{31}(\omega) &= d_+\left[a_+^{(0)} e^{i4\pi/3} + a_-^{(0)} e^{-i4\pi/3}\right].
\end{aligned}
\tag{3.1.26}
$$

Due to the rotational symmetry of the structure, the rest of the S-parameters can be directly calculated from (3.1.26) by rotating the port indices as $(1,2,3) \to (3,1,2) \to (2,3,1)$. For example, S_{13} and S_{23} can be calculated from (3.1.26) by applying $(1,2,3) \to (3,1,2)$: $S_{13} = S_{21}$ and $S_{23} = S_{31}$. Note that, apart from signals at the input frequency (S-parameters given in (3.1.26)), there are also signals at frequencies $\omega \pm \omega_{\mathrm{m}}$. For excitation from port 1 the S-parameters for these signals can be found by substituting (3.1.24) into the second equation of (3.1.4) as

$$
\begin{aligned}
S_{11}(\omega - \omega_{\mathrm{m}}) &= S_{21}(\omega - \omega_{\mathrm{m}}) = S_{31}(\omega - \omega_{\mathrm{m}}) = d_+ a_-^{(-1)}, \\
S_{11}(\omega + \omega_{\mathrm{m}}) &= S_{21}(\omega + \omega_{\mathrm{m}}) = S_{31}(\omega + \omega_{\mathrm{m}}) = d_+ a_+^{(+1)}.
\end{aligned}
\tag{3.1.27}
$$

The rest of the S-Parameters at $\omega \pm \omega_{\mathrm{m}}$ can be found again via rotation of the port indices.

Due to its three-fold symmetry, the modulated loop operates as a circulator, if the signal at one of the output posters is equal to zero. For the modulation phase used here (0 deg, 120 deg and 240 deg for resonators 1, 2 and 3, respectively), this condition is satisfied at port 3 if the frequency of the incident wave is ω_+ and

$$
\delta\omega_{\mathrm{m}} = 2\sqrt{\frac{\gamma_+(\omega_{\mathrm{m}}^2 + \gamma_+^2)}{\omega_{\mathrm{m}}\sqrt{3} - \gamma_+}}.
\tag{3.1.28}
$$

Observe that in order for $\delta\omega_{\mathrm{m}}$ to be real, the condition $\omega_{\mathrm{m}}\sqrt{3} \geq \gamma_{+}$ should hold. When (3.1.28) is satisfied, it is easy to show from (3.1.25) that the right- and left-handed states are respectively excited with phases $\pi/6$ and $-\pi/6$ at port 1. Their phases become $\pi/6+4\pi/3=3\pi/2$ and $-\pi/6-4\pi/3=-3\pi/2$ at port 3, leading to mutual cancellation by destructive interference at this port. Since no power is transferred to port 3, one may think that, in the absence of loss, the transmission to port 2 is perfect. However, this is not true since, as already hinted, modulation results in allocation of part of the energy to frequencies outside the main band in the form of intermodulation products. Under the ideal modulation condition (3.1.28), it can be found from (3.1.25) and (3.1.26) that the transmission at port 2 and the reflection at the input port (port 1) are respectively given by is

$$\left|S_{21}(\omega)\right| = \gamma_{+,\mathrm{cpl}}\left|\frac{1}{\omega_{\mathrm{m}}\sqrt{3}} - \frac{1}{\gamma_{+}}\right|, \tag{3.1.29}$$

$$\left|S_{11}(\omega)\right| = 1 - \left|S_{21}(\omega)\right|. \tag{3.1.30}$$

Observe that, since $\gamma_{+,\mathrm{cpl}} < \gamma_{+}$, $\left|S_{21}(\omega)\right| < 1$, as expected from the conversion of part of the power to intermodulation products. The intermodulation products at any port are found from (3.1.25) and (3.1.27) as

$$\left|S_{21}(\omega \pm \omega_{\mathrm{m}})\right| = \sqrt{\frac{1}{3}\left|S_{21}(\omega)\right|\left[\frac{\gamma_{+,\mathrm{cpl}}}{\gamma_{+}} - \left|S_{21}(\omega)\right|\right]}, \tag{3.1.31}$$

and they are always greater than zero. The transmission bandwidth, another important parameter of the structure, is given by $2\gamma_{+}$ and it satisfies

$$\mathrm{BW} = 2\gamma_+ = \sqrt{3}\omega_\mathrm{m}\left[1-\frac{\gamma_+}{\gamma_{+,\mathrm{cpl}}}\left|S_{21}(\omega)\right|\right]. \tag{3.1.32}$$

Considering that $\gamma_{+,\mathrm{cpl}} \le \gamma_+$, where the equality holds in the absence of loss, Eqs. (3.1.31) and (3.1.32) lead to the following expressions, involving only $\left|S_{21}(\omega)\right|$:

$$\left|S_{21}(\omega \pm \omega_\mathrm{m})\right| \le \sqrt{\frac{1}{3}\left|S_{21}(\omega)\right|\left[1-\left|S_{21}(\omega)\right|\right]}, \tag{3.1.33}$$

$$\mathrm{BW} \le \sqrt{3}\omega_\mathrm{m}\left[1-\left|S_{21}(\omega)\right|\right]. \tag{3.1.34}$$

Eq. (3.1.33) shows that the intermodulation products tend to zero, as the transmission approaches unity, as expected from power conservation. On the other hand, Eq. (3.1.34) reveals a fundamental trade-off between bandwidth and transmission. For a specified modulation frequency, bandwidth decreases, as transmission increases. In order to increase transmission without affecting the bandwidth, it is necessary to increase the modulation frequency.

3.2 Connecting Performance Metrics for General Angular-Momentum-Biased Circulator

Fig. 38 presents $\left|S_{21}(\omega)\right|$, $\left|S_{21}(\omega \pm \omega_\mathrm{m})\right|$, $\left|S_{11}(\omega)\right|$ and BW versus $\delta\tilde{\omega}_\mathrm{m} = \delta\omega_\mathrm{m}/\gamma_{+,\mathrm{loss}}$ and $\tilde{\omega}_\mathrm{m} = \omega_\mathrm{m}/\gamma_{+,\mathrm{loss}}$ under the infinite-isolation condition (3.1.28). In these plots we use the normalized modulation parameters, $\delta\tilde{\omega}_\mathrm{m}$ and $\tilde{\omega}_\mathrm{m}$, instead of the absolute ones, $\delta\omega_\mathrm{m}$ and ω_m, since the response of the structure, such as the *S*-parameters, depends on $\gamma_{+,\mathrm{loss}}$, which generally is different for different structures. As a result, a plot of the structure's response versus $\delta\omega_\mathrm{m}$ and ω_m is only valid for specific $\gamma_{+,\mathrm{loss}}$, narrowing

its applicability. This problem is overcome by considering $\gamma_{+,\text{loss}}$, over which we have little control, as a normalization quantity, and plotting the response versus $\delta\tilde{\omega}_\text{m} = \delta\omega_\text{m}/\gamma_{+,\text{loss}}$ and $\tilde{\omega}_\text{m} = \omega_\text{m}/\gamma_{+,\text{loss}}$. It should be noted that $2\gamma_{+,\text{loss}}$ is the bandwidth of the intrinsic resonance of the system, i.e., the resonance under negligible coupling to the external lines, and, as such, it also represents a lower bound for the bandwidth of the loaded system BW. Considering that $Q_+ = \omega_0/(2\gamma_{+,\text{loss}})$, where $Q_{+,\text{loss}}$ is the intrinsic Q-factor of the system, the normalized modulation parameters in Fig. 38 can also be expressed as $\delta\tilde{\omega}_\text{m} = 2Q_{+,\text{loss}}\,\delta\omega_\text{m}/\omega_0$ and $\tilde{\omega}_\text{m} = 2Q_{+,\text{loss}}\,\omega_\text{m}/\omega_0$. The white region in Fig. 38 corresponds to values of the modulation parameters for which infinite isolation is impossible. Furthermore, the charts in Fig. 38 are valid, provided that the conditions $\omega_\text{m}, \delta\omega_\text{m} \ll \omega_0$, under which Eqs. (3.1.23) have been derived, hold[1]. It is easy to show that these conditions are satisfied, if $\delta\tilde{\omega}_\text{m}, \tilde{\omega}_\text{m} \ll 2Q_{+,\text{loss}}$. Through numerical calculations, we have found that $0.5Q_{+,\text{loss}}$ and $0.1Q_{+,\text{loss}}$ are good upper bounds for $\tilde{\omega}_\text{m}$ and $\delta\tilde{\omega}_\text{m}$, respectively. Fig. 38 allows designing structures with specified response, in terms of $|S_{21}(\omega)|$, $|S_{21}(\omega \pm \omega_\text{m})|$, $|S_{11}(\omega)|$ and BW, for given $\gamma_{+,\text{loss}}$.

[1] As explained before, the condition under which (3.1.23) are valid is $\omega_\text{m}, \delta\omega_\text{m} \ll |\omega_{\text{m}+} - \omega_\text{c}| \approx |\omega_+ - \omega_\text{c}|$. Assuming that $\omega_\text{c} \ll \omega_+$, as happens for the structures that are presented in Sec. III, the above condition becomes $\omega_\text{m}, \delta\omega_\text{m} \ll \omega_+$.

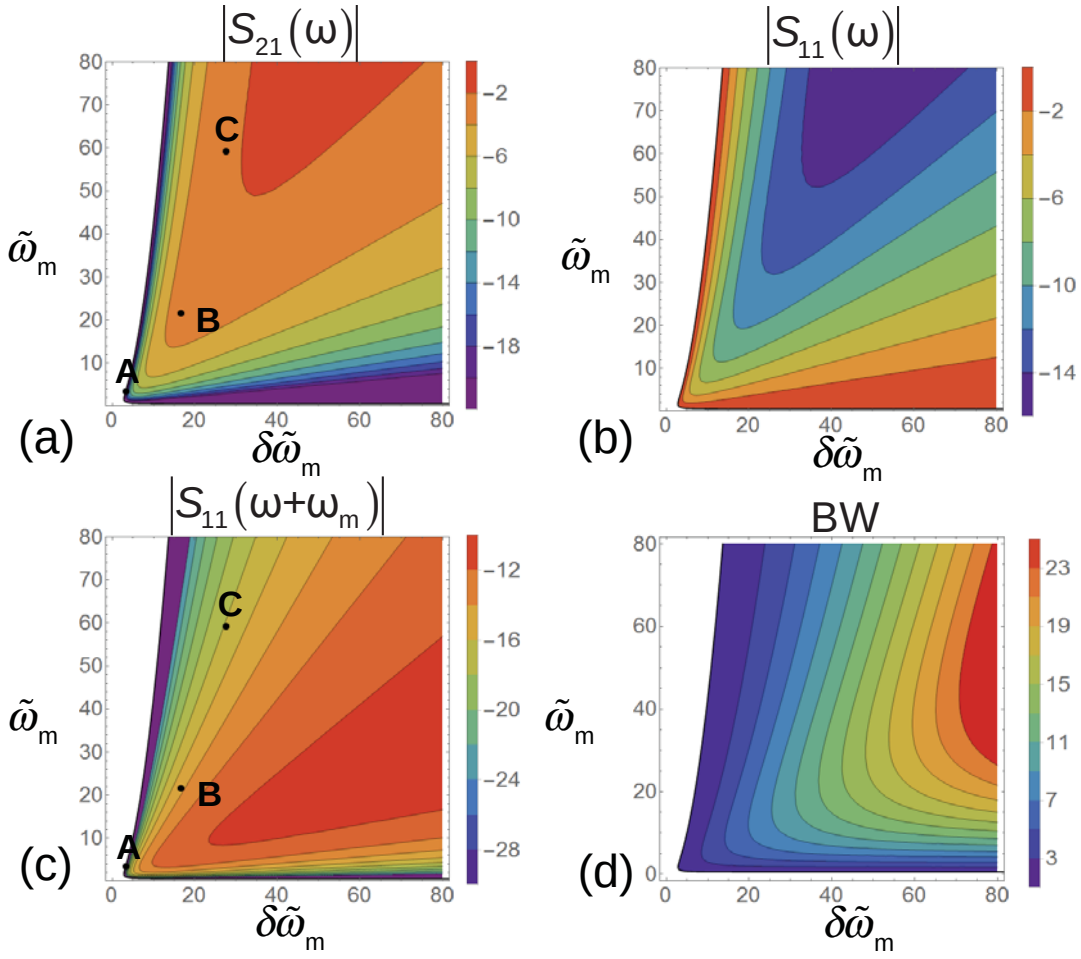

Figure 38: Design charts for magnetic-free circulators based on loops of modulated resonators. (a) Insertion loss, $|S_{21(\omega)}|$, (b) return loss, $|S_{11(\omega)}|$, (c) intermodulation products, $|S_{21(\omega\pm\omega_m)}|$, and (d) bandwidth, BW, versus the normalized modulation frequency, $\tilde{\omega}_m = \omega_m/\gamma_{+,loss}$, and the normalized modulation amplitude, $\delta\tilde{\omega}_m = \delta\omega_m/\gamma_{+,loss}$. All the results were derived under condition (3.1.28) to obtain maximum isolation. Point A corresponds to the design in [75], while points B and C to the designs in [29]. Inside the white regions, infinite isolation is impossible.

The charts in Fig. 38 allow reaching interesting conclusions about the effect of the modulation parameters on the characteristics of the structure. First of all, insertion and return losses generally decrease when both $\tilde{\omega}_{\mathrm{m}}$ and $\delta\tilde{\omega}_{\mathrm{m}}$ increase. On the other hand, intermodulation products tend to decrease as $\tilde{\omega}_{\mathrm{m}}$ increases. This behavior is consistent with (3.1.21), where the term $\Delta\omega/\delta\omega_{\mathrm{m}}$, providing the amplitude of the undesired secondary sub-states of the modulated loop, decreases as ω_{m} increases. Apart from leading to smaller reflection, larger transmission and smaller intermodulation products, increasing ω_{m} is also advantageous from an implementation point of view: a large ω_{m}, and therefore a large separation between the wanted frequency response and the unwanted intermodulation products, results in less steep filters for the rejection of these products, and therefore easier fabrication. The charts in Fig. 38 and the above general conclusions will be used in the next section in order to design two magnetic-free microwave circulators based on lumped and distributed elements for low- and high-frequency applications, respectively.

We will use these general design charts to explore two proof-of-concept optimal designs for magnetic-free microwave circulators in Chapter 4.

3.3 Resonance Shift Due To Modulation

Here, we show that modulation creates a shift in the resonance frequency of second order with respect to δC_{m}. Such an effect cannot be predicted by the first-order coupled-mode theory and it requires full solution of circuit equations. By defining the inductor currents and capacitor charges as in Fig. 39, Kirchhoff's laws read

$$i_1 + i_2 + i_3 = 0, \tag{3.3.1}$$

$$
\begin{aligned}
2v_1^{\text{inc}} - Z_0 i_1 - L\frac{di_1}{dt} - \frac{q_1}{C_1} &= 2v_2^{\text{inc}} - Z_0 i_2 - L\frac{di_2}{dt} - \frac{q_2}{C_2}, \\
2v_1^{\text{inc}} - Z_0 i_1 - L\frac{di_1}{dt} - \frac{q_1}{C_1} &= 2v_3^{\text{inc}} - Z_0 i_3 - L\frac{di_3}{dt} - \frac{q_3}{C_3}, \\
2v_2^{\text{inc}} - Z_0 i_2 - L\frac{di_2}{dt} - \frac{q_2}{C_2} &= 2v_3^{\text{inc}} - Z_0 i_3 - L\frac{di_3}{dt} - \frac{q_3}{C_3}.
\end{aligned}
\tag{3.3.2}
$$

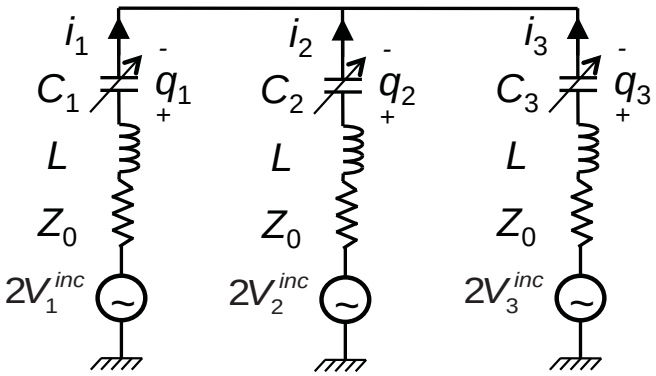

Figure 39: Circuit schematic of the lumped-element wye resonator [29].

The sources v_i^{inc} stand for the incident waves from the three ports of the circuit. Summing the two first equations of (3.3.2) and replacing the term $i_2 + i_3$ in the resulting equation with $-i_1$ from (3.3.1) yields

$$
3L\frac{di_1}{dt} + 3Z_0 i_1 + 2\frac{q_1}{C_1} - \frac{q_2}{C_2} - \frac{q_3}{C_3} = 2(2v_1^{\text{inc}} - v_2^{\text{inc}} - v_3^{\text{inc}}). \tag{3.3.3}
$$

By performing the same operation to the other pairs of (3.3.2) we get

$$
\begin{aligned}
3L\frac{di_2}{dt}+3Z_0 i_2-\frac{q_1}{C_1}+2\frac{q_2}{C_2}-\frac{q_3}{C_3}&=2(-v_1^{\mathrm{inc}}+2v_2^{\mathrm{inc}}-v_3^{\mathrm{inc}}),\\
3L\frac{di_3}{dt}+3Z_0 i_3-\frac{q_1}{C_1}-\frac{q_2}{C_2}+2\frac{q_3}{C_3}&=2(-v_1^{\mathrm{inc}}-v_2^{\mathrm{inc}}+2v_3^{\mathrm{inc}}).
\end{aligned}
\tag{3.3.4}
$$

Equation (3.3.4) can be compactly written as

$$
\ddot{\mathbf{q}}+\frac{Z_0}{L}\dot{\mathbf{q}}+\frac{1}{L}\mathbf{D}\mathbf{C}^{-1}\mathbf{q}=\frac{2}{L}\mathbf{D}\mathbf{v}^{\mathrm{inc}},
\tag{3.3.5}
$$

where $\mathbf{q}=(q_1 \quad q_2 \quad q_3)^{\mathrm{T}}$, $\mathbf{v}^{\mathrm{inc}}=(v_1^{\mathrm{inc}} \quad v_2^{\mathrm{inc}} \quad v_3^{\mathrm{inc}})$, $\mathbf{C}=\mathrm{diag}\{C_1,C_2,C_3\}$ and

$$
\mathbf{D}=\frac{1}{3}\begin{pmatrix}2&-1&-1\\-1&2&-1\\-1&-1&2\end{pmatrix}.
\tag{3.3.6}
$$

For the derivation of (3.3.5) we have also used $i_i=dq_i/dt$. In the presence of modulation, $C_n=C+\delta C_{\mathrm{m}}\cos[\omega_{\mathrm{m}}t+2(n-1)\pi/3]$ and, if $\delta C_{\mathrm{m}}\ll C$, (3.3.5) becomes

$$
\ddot{\mathbf{q}}+\frac{Z_0}{L}\dot{\mathbf{q}}+\frac{1}{LC}\mathbf{D}\mathbf{q}-\frac{\delta C_{\mathrm{m}}}{LC^2}\mathbf{D}\mathbf{M}\mathbf{q}=\frac{2}{L}\mathbf{D}\mathbf{v}^{\mathrm{inc}},
\tag{3.3.7}
$$

where $\mathbf{M}=\mathrm{diag}\{\cos(\omega_m t),\cos(\omega_{\mathrm{m}}+2\pi/3),\cos(\omega_{\mathrm{m}}+4\pi/3)\}$.

Similarly to (3.1.1), (3.3.7) can be transformed to the eigenbasis of the common and rotating states of the ring as

$$
\ddot{\tilde{\mathbf{q}}}+\frac{Z_0}{L}\dot{\tilde{\mathbf{q}}}+\frac{1}{LC}\tilde{\mathbf{D}}\tilde{\mathbf{q}}-\frac{\delta C_{\mathrm{m}}}{LC^2}\tilde{\mathbf{D}}\tilde{\mathbf{M}}\tilde{\mathbf{q}}=\frac{2}{L}\tilde{\mathbf{D}}\tilde{\mathbf{v}}^{\mathrm{inc}},
\tag{3.3.8}
$$

where $\tilde{\mathbf{q}}=\mathbf{U}^{\mathrm{H}}\mathbf{q}$, $\tilde{\mathbf{v}}=\mathbf{U}^{\mathrm{H}}\mathbf{v}$, $\tilde{\mathbf{D}}=\mathrm{diag}\{0,1,1\}$ and

$$\tilde{\mathbf{M}} = \frac{1}{2}\begin{pmatrix} 0 & e^{-i\omega_m t} & e^{i\omega_m t} \\ e^{i\omega_m t} & 0 & e^{-i\omega_m t} \\ e^{-i\omega_m t} & e^{i\omega_m t} & 0 \end{pmatrix}. \tag{3.3.9}$$

Neglecting the common mode, as in the case of the coupled-mode analysis, (3.3.8) becomes

$$\begin{aligned} \ddot{q}_+ + \frac{\omega_0}{Q}\dot{q}_+ + \omega_0^2 q_+ - \omega_0 \delta\omega_m e^{-i\omega_m t} q_- &= \frac{2}{L\sqrt{3}} e^{-i\omega t}, \\ \ddot{q}_- + \frac{\omega_0}{Q}\dot{q}_- + \omega_0^2 q_- - \omega_0 \delta\omega_m e^{i\omega_m t} q_+ &= \frac{2}{L\sqrt{3}} e^{-i\omega t}, \end{aligned} \tag{3.3.10}$$

where $q_\pm$ are the amplitudes of the rotating states, $\omega_0 = 1/\sqrt{LC}$, $Q = \omega_0 L / Z_0$ and $\delta\omega_m = \omega_0 \, \delta C_m / (2C)$. For the derivation of (3.3.10) we have assumed that the structure is excited from port 1 with a signal of unitary amplitude and frequency ω. Similarly to (3.1.23), (3.3.10) can be solved by making the assumption

$$\begin{aligned} q_+ &= q_+^{(0)} e^{-i\omega t} + q_+^{(+1)} e^{-i(\omega+\omega_m)t}, \\ q_- &= q_-^{(0)} e^{-i\omega t} + q_-^{(-1)} e^{-i(\omega-\omega_m)t}, \end{aligned} \tag{3.3.11}$$

which leads to

$$\begin{aligned} q_\pm^{(0)} &= -\frac{2}{\sqrt{3}} \frac{\omega_0^2[\omega_0^2 - (\omega \mp \omega_m)^2 - i2\gamma(\omega \mp \omega_m)]}{\omega_0^2 \delta\omega_m^2 - (\omega_0^2 - \omega^2 - i2\gamma\omega)[\omega_0^2 - (\omega \mp \omega_m)^2 - i2\gamma(\omega \mp \omega_m)]}, \\ q_\pm^{(\pm 1)} &= \frac{2}{\sqrt{3}} \frac{\omega_0^3 \delta\omega_m}{\omega_0^2 \delta\omega_m^2 - (\omega_0^2 - \omega^2 - i2\gamma\omega)[\omega_0^2 - (\omega \pm \omega_m)^2 - i2\gamma(\omega \pm \omega_m)]}. \end{aligned} \tag{3.3.12}$$

The resonances associated with the dominant sub-states of the circuit can be found from the roots of the denominator in the first equation of (3.3.12). For sufficiently high *Q*-factor, γ can be taken equal to zero and

$$\omega_{\mathrm{m}\pm} = \frac{1}{2}\left[\sqrt{\omega_{\mathrm{m}}^2 + 4\omega_0(\omega_0 \mp \sqrt{\omega_{\mathrm{m}}^2 + \delta\omega_{\mathrm{m}}^2})} \pm \omega_{\mathrm{m}}\right]. \tag{3.3.13}$$

These frequencies are shifted from ω_0 by different amounts, implying that their center of mass, $\omega_{\mathrm{c}} = (\omega_{\mathrm{m}+} + \omega_{\mathrm{m}-})/2$, is also shifted from ω_0. In particular, it is not difficult to show that

$$\omega_{\mathrm{c}} = \omega_0 - \frac{\omega_0}{8\omega_0^2 - 2\omega_{\mathrm{m}}^2}\delta\omega_{\mathrm{m}}^2 + O(\delta\omega_{\mathrm{m}}^4). \tag{3.3.14}$$

Therefore, ω_{c} is red-shifted from ω_0 by the amount $\omega_0\delta\omega_{\mathrm{m}}^2/(8\omega_0^2 - 2\omega_{\mathrm{m}}^2)$ at the point in which isolation becomes maximum, or, for $\omega_{\mathrm{m}} \ll \omega_0$, $\delta\omega_{\mathrm{m}}^2/(8\omega_0)$. This shifting is the result of the second-order nature of (3.3.5), and it is related to the weak coupling between positive and negative frequencies, which are completely neglected in coupled-mode analysis.

3.4 Passivity and the Exchange of Power for Angular-Momentum-Biased Circulators

As previously described, imparting spatiotemporal modulation upon a resonant structure allows one to emulate an angular-momentum-bias, thus breaking reciprocity of the system. Here, we investigate power exchange between the modulation and operation signals for circulators based on this approach. In particular, we study the most practically relevant case of a circulator comprising three spatiotemporally modulated resonators with symmetrical coupling between them [29],[75]. Coupled-mode analysis is expected to zero power exchange between the modulation and operation signals, due to the conservation of power assumptions in (3.1.1). The results to be shown are a proof that, like magnetic-

based devices, angular-momentum-based ones are inherently passive. Like the magnetic field, angular-momentum interacts with the structure in a totally reactive way: it creates a phase asymmetry for wave propagating in opposite directions, but it does affect the power balance of the circuit.

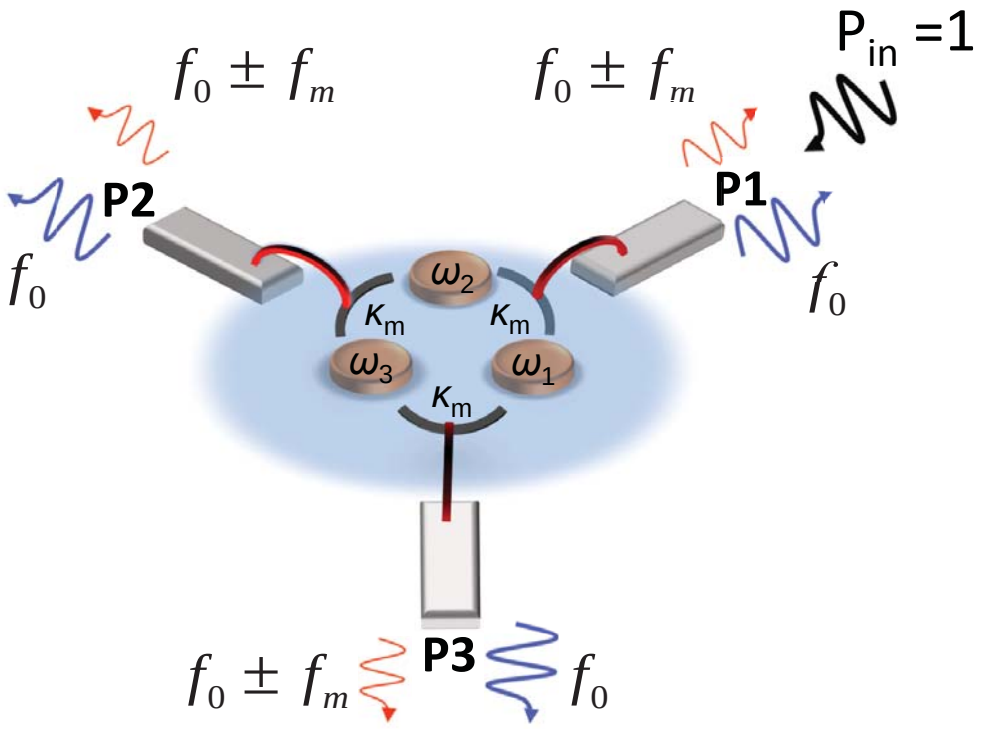

Figure 40: Input and output signals for an angular-momentum-biased circulator. Assuming an incident wave at the fundamental frequency, f, the output signals exist at both the fundamental and inter-modulation frequencies.

Fig. 40 presents the possible output signals for the circulators in [29],[75], when excited from port 1 with a signal of frequency f. In addition to the output signals at the same frequency as the input one, there are also signals at frequencies $f \pm f_m$, where f_m is the modulation frequency, as the result of the modulation or, equivalently, the Doppler

effect related to the effective spinning of the structure. Through coupled-mode theory [78], analytical expressions for the scattering parameters of the structure were derived in Section 3.1, which are repeated here for convenience:

$$\begin{aligned} S_{11}(\omega) &= -1+\sqrt{2\gamma_c/3}\left[a_+^{(0)}+a_-^{(0)}\right], \\ S_{21}(\omega) &= \sqrt{2\gamma_c/3}\left[a_+^{(0)}e^{i2\pi/3}+a_-^{(0)}e^{-i2\pi/3}\right], \\ S_{31}(\omega) &= \sqrt{2\gamma_c/3}\left[a_+^{(0)}e^{i4\pi/3}+a_-^{(0)}e^{-i4\pi/3}\right], \end{aligned} \tag{3.4.1}$$

$$\begin{aligned} S_{11}(\omega\pm\omega_m) &= \sqrt{2\gamma_c/3}a_\pm^{(\pm1)}, \\ S_{21}(\omega\pm\omega_m) &= \sqrt{2\gamma_c/3}a_\pm^{(\pm1)}e^{\pm i2\pi/3}, \\ S_{31}(\omega-\omega_m) &= \sqrt{2\gamma_c/3}a_\pm^{(\pm1)}e^{\pm i4\pi/3}, \end{aligned} \tag{3.4.2}$$

where

$$\begin{aligned} a_\pm^{(0)} &= \sqrt{2\gamma_c/3}\,\frac{-i(\omega-\omega_0\mp\omega_m)+\gamma_c}{[-i(\omega-\omega_0)+\gamma_c][-i(\omega-\omega_0\mp\omega_m)+\gamma_c]+\delta\omega_m^2/4}, \\ a_\pm^{(\pm1)} &= \sqrt{2\gamma_c/3}\,\frac{-i\,\delta\omega_m/2}{[-i(\omega-\omega_0)+\gamma_c][-i(\omega-\omega_0\mp\omega_m)+\gamma_c]+\delta\omega_m^2/4}, \end{aligned} \tag{3.4.3}$$

γ_c is the coupling decay rate between the ports and the resonator, $\delta\omega_m$ is the modulation amplitude, and ω_0 is the frequency of the degenerate, un-modulated states. Perfect isolation at port 2 is obtained when

$$\delta\omega_m = 2\sqrt{\frac{\gamma_c(\omega_m^2+\gamma_c^2)}{\omega_m\sqrt{3}-\gamma_c}}. \tag{3.4.4}$$

The power exchanged between the modulation and operation signals can be found from

$$X(\omega) = 1 - \sum_{n=-1}^{1} \sum_{m=1}^{3} \left| S_{m1}(\omega + n\omega_{\mathrm{m}}) \right|^2 . \tag{3.4.5}$$

The double sum in the right-hand side of the above equation is the output power at the input and intermodulation frequencies. Under the optimum modulation condition (3.4.4) and for $\omega = \omega_0$, when isolation is maximum (theoretically infinite), (3.4.5) reads

$$X(\omega_0) = 1 - \frac{\gamma_c^2}{3\omega_m^2} - \frac{1}{9}\left| \frac{\sqrt{3}\gamma_c}{\omega_m} - 3 \right|^2 - \frac{2}{3}\frac{\left| \gamma_c \left(\gamma_c - \sqrt{3}\omega_m \right) \right|}{\omega_m^2} . \tag{3.4.6}$$

If $\gamma_{\mathrm{c}} > \sqrt{3}\omega_{\mathrm{m}}$, which is the necessary condition in order for $\delta\omega_{\mathrm{m}}$ to be real for a passive design ($\gamma_{\mathrm{c}} > 0$), $X(\omega_0) = 0$. We observe that the coupled mode theory predicts identically zero power exchange between the fundamental and modulation signals, at least under optimum modulation conditions.

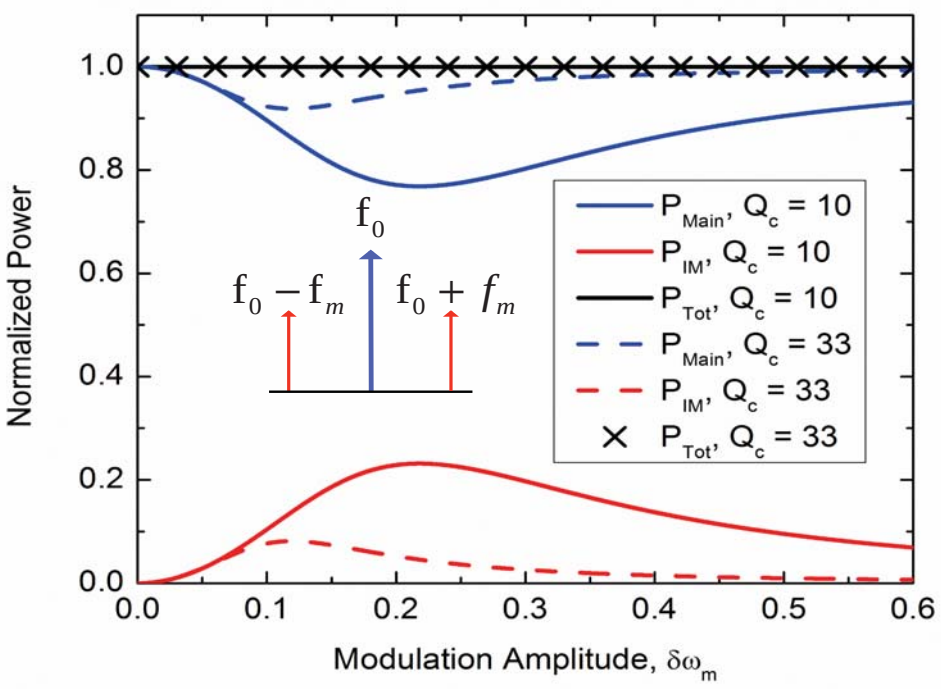

Figure 41: Power distributed to the fundamental (main) and intermodulation (IM) signals for AM circulator, as predicted from coupled-mode theory. The total power, defined as the sum of the fundamental and intermodulation contributions, is also presented. Results correspond to two different Q-factors. The intermodulation power maximum occurs at the maximum isolation condition. The total power remains equal to unity for all values of modulation amplitude, demonstrating the passivity of the circuit.

The power exchange remains zero even if (3.4.4) is not satisfied, as can be seen in Fig. 41, which plots the output power at ω_0 and $\omega_0 \pm \omega_m$ versus $\delta\omega_m$ for $\omega_m/\omega_0 = 0.2$ and two different quality (Q) factors (without loss, as assumed here, $Q = \omega_0/(2\gamma_c)$). Observe that the sum of the output power at ω_0 and $\omega_0 \pm \omega_m$ is always unity, implying $X(\omega_0) = 0$. Similar results can also be found for an arbitrary input frequency ω. Note

that the zero power exchange is also in agreement with the fact that the coupled mode equations in [29] through which (3.4.1)-(3.4.3) are derived involve Hermittian matrices.

Fig. 41 can also lead to interesting conclusions regarding the distribution of power to the different intermodulation products. When $\delta\omega_{\mathrm{m}} = 0$, i.e., when there is no modulation, the intermodulation products are zero. As $\delta\omega_{\mathrm{m}}$ increases, the intermodulation products grow and they become maximum at the optimum coupling condition, when isolation is maximum (theoretically infinite). Past the optimum modulation point, the effect of modulation is reduced and the same happens to the intermodulation products. It is evident that intermodulation is a necessary by-product in order to break reciprocity. Nevertheless, by increasing the *Q*-factor, it is possible to significantly reduce the intermodulation strength, as can be seen in Fig. 41 for the two different values of the *Q*-factor.

The coupled-mode theory analysis states that power exchange is identically zero for any modulation amplitude and frequency, which obviously cannot be true: a parametric circuit with resonant frequency ω_0 is generally unstable for $\omega_{\mathrm{m}} = 2\omega_0/n$, where n is an integer. The reason why coupled-mode theory fails to predict possible power exchange between the modulation and input signals is that it is developed by assuming power conservation, which for systems described by symmetrical frequency matrices $\mathbf{\Omega}$, as in Fig. 40, remains valid even in the case of modulation.

For this reason, investigation of the power properties of the parametric circulator in Fig. 40 can only be achieved through full-wave or circuit models for particular topologies. Here, we will use the wye circuit in Fig. 39, which exhibits favorable characteristics in terms of performance and implementation complexity, and for which

the scattering parameters can be expressed in closed form. As the general network in Fig. 40, the circuit in Fig. 39 supports right- and left-handed rotating modes. By applying Kirchhoff's laws and assuming an incident signal from port 1 with frequency ω and unitary amplitude, it is possible to show that the complex amplitudes of these modes satisfy

$$\begin{aligned}\ddot{q}_+ + \frac{Z_0}{L}\dot{q}_+ + \frac{1}{LC}q_+ - \frac{\delta C_{\mathrm{m}}}{2LC^2}e^{-i\omega_{\mathrm{m}}t}q_- &= \frac{2V_{\mathrm{inc}}}{L\sqrt{3}}e^{-i\omega t},\\ \ddot{q}_- + \frac{Z_0}{L}\dot{q}_- + \frac{1}{LC}q_- - \frac{\delta C_{\mathrm{m}}}{2LC^2}e^{i\omega_{\mathrm{m}}t}q_+ &= \frac{2V_{\mathrm{inc}}}{L\sqrt{3}}e^{-i\omega t},\end{aligned} \tag{3.4.7}$$

where q_+ and q_- are the amplitudes of the right- and left-handed modes. Note that (3.4.7) is exact, despite the fact that it does not involve a common mode, as one might expect for a network with rotational symmetry. The reason is that the common mode of the wye circuit is a trivial with zero frequency and zero stored energy, practically implying that it does not really exist. (3.4.7) can be analytically solved to give

$$\begin{aligned}q_+ &= q_+^{(0)}e^{-i\omega t} + q_+^{(+1)}e^{-i(\omega+\omega_{\mathrm{m}})t},\\ q_- &= q_-^{(0)}e^{-i\omega t} + q_-^{(-1)}e^{-i(\omega-\omega_{\mathrm{m}})t},\end{aligned} \tag{3.4.8}$$

where

$$\begin{aligned}q_\pm^{(0)} &= \frac{2CV_{\mathrm{inc}}}{\sqrt{3}}\frac{\omega_0^2[\omega_0^2 - (\omega \mp \omega_{\mathrm{m}})^2 - i2\gamma(\omega \mp \omega_{\mathrm{m}})]}{\Delta_\mp},\\ q_\pm^{(\pm 1)} &= \frac{2CV_{\mathrm{inc}}}{\sqrt{3}}\frac{\omega_0^3\delta\omega_{\mathrm{m}}}{\Delta_\pm},\end{aligned} \tag{3.4.9}$$

$\Delta_{\pm}=(\omega_0^2-\omega^2-i2\gamma\omega)[\omega_0^2-(\omega\pm\omega_{\rm m})^2-i2\gamma(\omega\pm\omega_{\rm m})]-\omega_0^2\delta\omega_{\rm m}^2, \gamma=Z_0/(2L)$, and $\delta\omega_{\rm m}=\omega_0\delta C_{\rm m}/(2C)$. Interestingly enough, the only harmonics existing in the wye resonator are $\omega\pm\omega_{\rm m}$. From q_+ and q_- it is possible to find the varactor charges as

$$\begin{aligned} q_1 &= \frac{1}{\sqrt{3}}(q_+ + q_-), \\ q_2 &= \frac{1}{\sqrt{3}}(q_+ e^{i2\pi/3} + q_- e^{i4\pi/3}), \\ q_3 &= \frac{1}{\sqrt{3}}(q_+ e^{i4\pi/3} + q_- e^{i2\pi/3}). \end{aligned} \tag{3.4.10}$$

The power supplied by the modulation signal to the network is essentially the power leaving the resonator at points A, B and C, which can be calculated through

$$P_{\rm m} = -\frac{1}{2}\left\langle \mathrm{Re}\{v_{\rm A}^* i_{\rm A} + v_{\rm B}^* i_{\rm B} + v_{\rm C}^* i_{\rm C}\}\right\rangle, \tag{3.4.11}$$

where

$$\left\langle f\right\rangle = \lim_{T\to\infty}\frac{1}{T}\int_{-T/2}^{T/2} f(t)dt. \tag{3.4.12}$$

The currents and voltages at points A, B, and C are given by

$$\begin{aligned} i_{\rm A} &= \dot{q}_1, \quad v_{\rm A} = 2V_{\rm inc}e^{-i\omega t} - Z_0\dot{q}_1, \\ i_{\rm B} &= \dot{q}_2, \quad v_{\rm B} = -Z_0\dot{q}_2, \\ i_{\rm C} &= \dot{q}_3, \quad v_{\rm C} = -Z_0\dot{q}_3. \end{aligned} \tag{3.4.13}$$

Inserting (3.4.10) and (3.4.13) into (3.4.11) yields

$$P_{\rm m} = \left\langle -\frac{1}{\sqrt{3}}\mathrm{Re}\{V_{\rm inc}^*(\dot{q}_+ + \dot{q}_-)e^{i\omega t}\} + \frac{Z_0}{2}\left(\left|\dot{q}_+\right|^2 + \left|\dot{q}_-\right|^2\right)\right\rangle. \tag{3.4.14}$$

By taking the complex conjugate of (3.4.7) and multiplying the resulting expressions q_+ and q_-, we can show that

$$P_{\mathrm{m}} = \frac{\delta C_{\mathrm{m}}}{4C^2}\left\langle \mathrm{Re}\{q_-^* \dot{q}_+ e^{i\omega_{\mathrm{m}}t} + q_+^* \dot{q}_- e^{-i\omega_{\mathrm{m}}t}\}\right\rangle. \tag{3.4.15}$$

Further reduction in (3.4.15) leads to the closed form expression for the exchanged power as

$$P_{\mathrm{m}} = \frac{2Z_0}{3}\left(CV_{\mathrm{inc}}\right)^2 \omega_{\mathrm{m}}\omega_0^6 \delta\omega_{\mathrm{m}}^2 \left(\frac{\omega-\omega_{\mathrm{m}}}{\left|\Delta_{\mathrm{m}}\right|^2} - \frac{\omega+\omega_{\mathrm{m}}}{\left|\Delta_{\mathrm{p}}\right|^2} \right). \tag{3.4.16}$$

The exchanged power (red curve), along with the transferred power in the main band (blue), is shown in Fig. 42(a). Here, the given terms are normalized for a Q-factor of 14, and the capacitor frequency and amplitude modulation is $\omega_{\mathrm{m}} = 0.2\omega_0$ and $\delta C_{\mathrm{m}} = 0.02$, respectively. It is clear that the minimum power exchanged is very small compared to the main power transmitted in the circuit. Further investigation shows that the exchange power resembles a bipolar waveform, with 4 poles located at the counter rotating ($\omega_{\mathrm{m}+}$, $\omega_{\mathrm{m}-}$) and inter-modulation offset ($\omega_{\mathrm{m}+} - \omega_{\mathrm{m}}$, $\omega_{\mathrm{m}-} + \omega_{\mathrm{m}}$) frequencies, as displayed in Fig. 42(a). The power exchange is red-shifted, expected from the analysis in Section 3.3, and asymmetric about the center resonance, ω_0. When comparing the power terms for a single frequency ($\omega_0 = 1$), the exchange power is 29.6 dB lower than the main band.

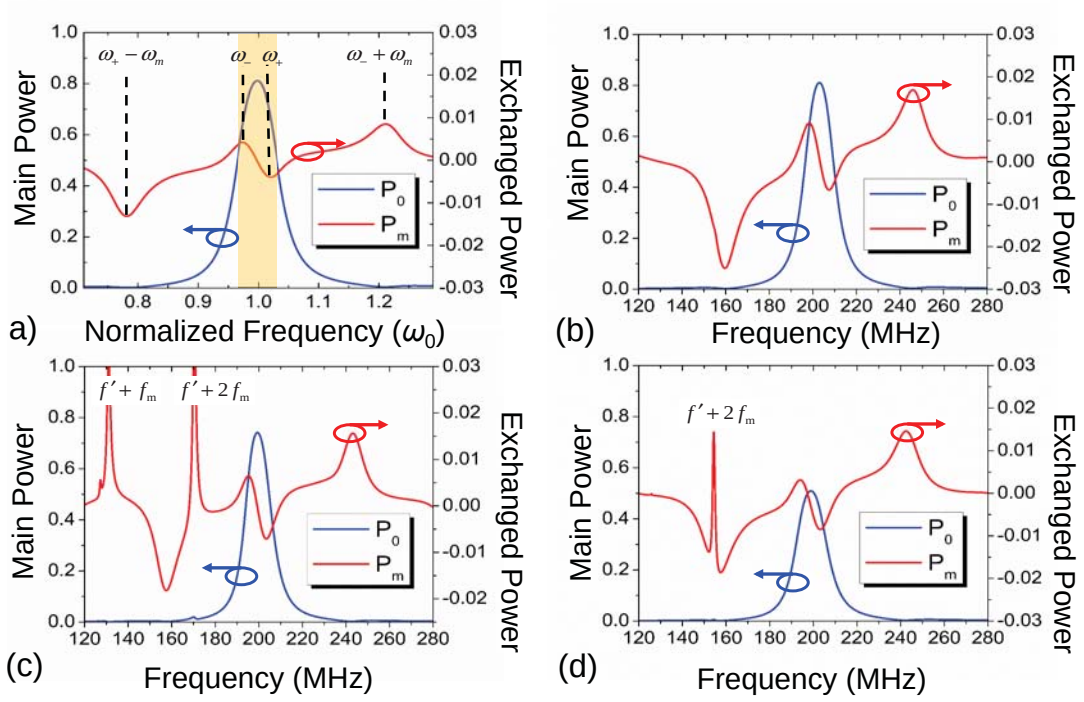

Figure 42: The main band, P_0, (blue) and exchanged power, P_m, (red) between the carrier and modulation signals under optimum circulator conditions. (a) Response for theory developed in equations (3.4.1) and (3.4.16). Shown for q-factor of 14 and $\omega_m = 0.2\omega_0$. Highlighted region is the FWHM bandwidth used in integration region. (b) Simulation of circulator with ideal, linear capacitor implementation. Simulation of full lumped-element circulator without loss (c) and with loss (d). Additional peaks between 130 and 170 MHz are higher order inter-modulation products attributed to circuit filters.

The comparison of power levels at a given frequency provides insight, however, a realistic system requires a finite frequency spectrum in order to transfer information. When the power is integrated over the full width half maximum (FWHM) (even about $\omega_0 = 1$), as shown as the highlighted region in Fig. 42(a), the exchanged power is more than 35.5 dB lower than the transmitted power. Other fractional bandwidths also show that the

exchange power is extremely small compared to the transmitted power (40.8 dB for 10%, 24 dB for 25%, and 23 dB for 40%).

To validate the coupled-mode-theory and transmission-line results, a lumped-element angular-momentum circulator, similar to the one in [29], was simulated in Agilent's Advanced Design System (ADS) through the harmonic-balance technique. The *Q*-factor of the circulator is around 15, the resonance frequency 198 MHz and the modulation frequency 40 MHz. In such a realistic scenario, the harmonics with order larger than one ($\omega \pm 2\omega_{\mathrm{m}}, \omega \pm 3\omega_{\mathrm{m}}, \ldots$) are generally non-zero and for this reason they were considered in the simulation. The number of harmonics was selected so that convergence in the results was ensured.

To begin with, an ideal, lossless lumped-element circulator consisting of linear capacitors (C_0 = 1.13 pF) and 560 nH inductors was simulated. The main and exchange power for this circuit is shown in Fig. 43(b). The response agrees extremely well with the transmission line theory, with the four poles present at the appropriate frequencies. Next, the linear capacitor was replaced with a high fidelity varactor model (Skyworks SVM 1233), to include the parasitic effects, but without loss. The power response is shown in Fig. 42(c). The power exchange response is similar to the linear capacitor simulation, but now includes two additional peaks (identified as $f' + f_m$, $f' + 2f_{\mathrm{m}}$ in Fig. 42(c)). These additional peaks related to the higher order intermodulation products for a resonance attributed to the filter ($f' \sim 90$ MHz). These terms were not present in frequency space of Fig. 42(b), but were lower in frequency due to the lower static capacitance of the linear capacitor in the simulation. Additionally, the main transmission power is reduced from the linear capacitor simulation due to filters and some power being distributed to

harmonics introduced by the non-linearities. Lastly, the addition of loss in the resonant inductor and varactors leads to the high fidelity response of Fig. 42(d). Here, the transmitted power is further reduced due to the loss in the resonant elements, while the exchange power response remains very similar to previous simulations. Overall, the exchanged power is very small (the power exchange is less than 1% of the input power near operational band in all cases) in both theory and simulation, essentially validating the passivity of the angular-momentum approach.

Chapter 4 Realizing Angular-Momentum-Biased Circulators

4.1 AM Circulator - Lumped-Element Design

We realized the structure of Fig. 34 at RF using three basic L-C circuit tanks, as in Fig. 43(a), where the capacitance C is equally distributed on both sides of the inductance L to maintain a symmetric structure. The resonance frequency modulation is achieved via capacitance modulation, commonly obtained in RF with varactor diodes. These diodes are biased by two signals, a static one V_{dc}, which provides the required reverse bias and controls the static capacitance, and a RF one v_{m} with frequency ω_{m} and amplitude V_{m}, providing the time modulation. Assuming that the resonators are coupled to each other through capacitances C_{c}, as in Fig. 43(b), the frequencies of the common and rotating states are $\omega_{\mathrm{c}} = \omega_0 \big/ \sqrt{1+2C_{\mathrm{c}}/C}$ and $\omega_{\pm} = \omega_0 \sqrt{(C+3C_{\mathrm{c}}/2)/(C+2C_{\mathrm{c}})}$, respectively, where $\omega_0 = 1\big/\sqrt{LC}$ is the static resonance frequency of each tank. Then, if the amplitude of the capacitance modulation is ΔC_{m}, the frequency modulation amplitude is found as $\delta\omega_{\mathrm{m}} = \omega_{\pm}\,\Delta C_{\mathrm{m}}/(2C)$. The frequency ω_{c} should be designed to be as far as possible from $\omega_{\pm}$ in order for the common mode not to affect the operation of the structure at $\omega_{\pm}$, at which non-reciprocity occurs. In the lumped-element circuit of Fig. 43(b) this condition is satisfied by taking $C_{\mathrm{c}} \to \infty$, or equivalently by coupling the tanks through short circuits, yielding $\omega_{\mathrm{c}} = 0$ and $\omega_{\pm} = \omega_0 \sqrt{3}/2$.

---

[75] Authors: N.A. Estep, D.L. Sounas, J. Soric, and A. Alù.
Author Contributions: N.A.E. performed the experiment, D.L.S. and N.A.E. designed the structure and conducted the numerical calculations and theoretical modelling. J.S. helped in the selection and modelling of the modulation varactors. A.A. directed and supervised the work.

The non-reciprocal response of the circuit of Fig. 43(b) is demonstrated by capacitively coupling it to three microstrip transmission lines, realizing a three-port device. Exciting the structure from, e.g., port 1 at frequency $\omega_{\pm}$ results in the excitation of $\bar{\mathbf{a}}_{m+}$ and $\bar{\mathbf{a}}_{m-}$ with same amplitude and opposite phase $\phi_R = -\phi_L$, due to the symmetrical distribution of these states around $\omega_{\pm}$. Then, the signals at ports 2 and 3 are proportional to $e^{i2\pi/3}e^{i\phi_R} + e^{i4\pi/3}e^{i\phi_L}$ and $e^{-i2\pi/3}e^{i\phi_R} + e^{-i4\pi/3}e^{i\phi_L}$, respectively, as the superposition of $\bar{\mathbf{a}}_{m+}$ and $\bar{\mathbf{a}}_{m-}$ at these ports. If $\delta\omega_m$ and ω_m are selected so that $\phi_R = -\phi_L = \pi/6$, the signal at port 3 is identically zero, while the one at port 2 is non-zero, routing the incident power from port 1 to port 2. Due to the symmetry of the structure with respect to its ports, incident power from ports 2 and 3 is similarly routed to ports 3 and 1, thus realizing the functionality of a non-reciprocal circulator with infinite isolation. Notice, that the above description assumes a weak excitation of the common state, which makes clear the importance of choosing its resonance frequency as far as possible from the resonance frequency of the rotating states.

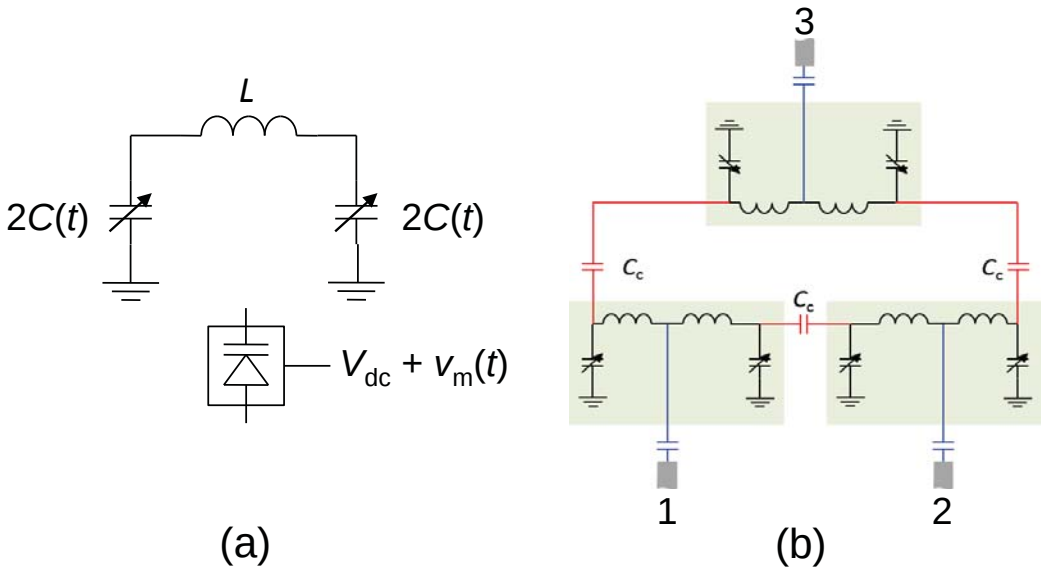

Figure 43: Circuit implementation of the non-reciprocal coupled-resonator loop at radio frequencies [75]. (a) A single resonant circuit of the proposed device: an *L*-*C* tank with modulated capacitance. The capacitance is equally distributed at both sides of the inductance to maintain symmetry. Capacitance modulation is achieved with varactor diodes, controlled by a static signal V_{dc} and the modulation signal $v_m(t)$. (b) A loop formed by three identical resonators coupled through three identical capacitances C_c. The loop is further coupled to three external microstrip lines carrying the external signal.

The complete circuit is designed to resonate at two frequencies: the modulation frequency f_m and the RF one f_{RF}, as shown in Fig. 44. By doing this we avoid three additional ports for feeding the varactors with the modulation signals and filters required to prevent the RF signal to leak into the modulation ports and vice versa, thus significantly simplifying the design. The dual resonance of the ring is achieved by combining two complementary networks. The first one is designed to resonate at the RF

frequency f_{RF}, and it consists of three L-C tanks with series inductances L_2 and shunt capacitances C_2 (red elements in Fig. 44), following the topology of Fig. 43.

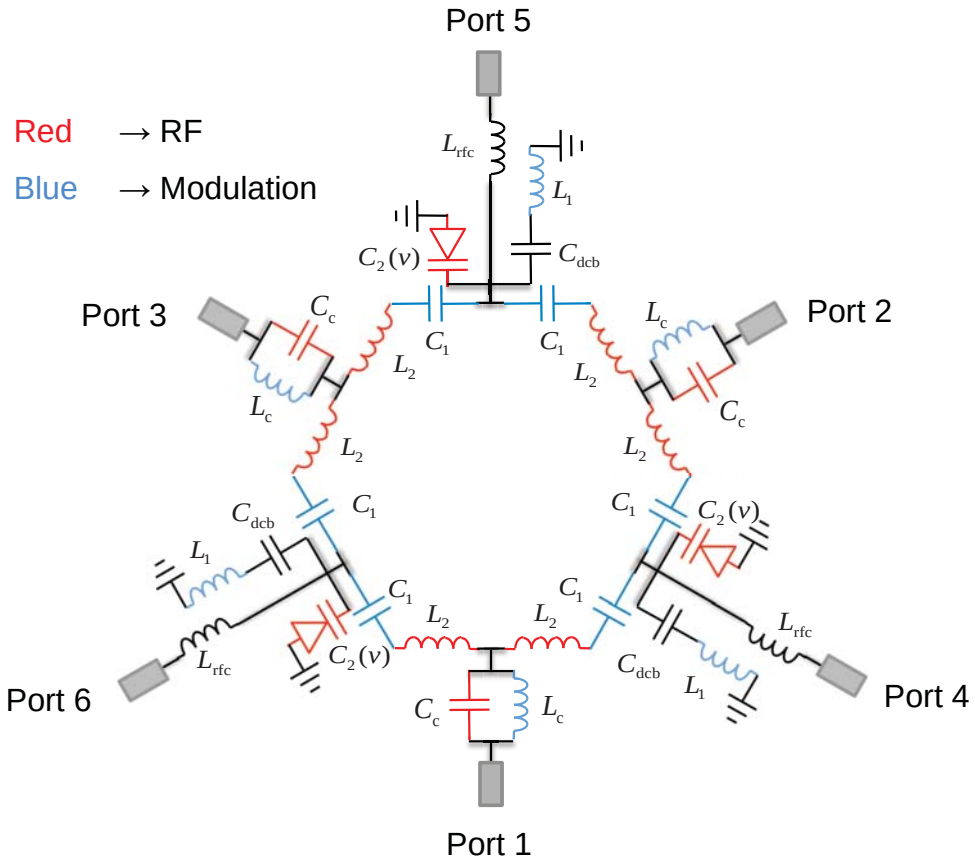

Figure 44: Implementation of the RF non-reciprocal coupled-resonator ring, including the biasing and modulation networks [75]. The ring consists of two complementary networks: one operating at the RF frequency (red elements) and another one operating at the modulation frequency (blue elements). Ports 1, 2 and 3 provide access to the ring for the RF and modulation signals. Ports 4, 5 and 6 provide access to the ring for the static biasing voltage.

The resonance frequency of this network can be found from elementary circuit analysis as

$$\omega_{\mathrm{RF}} = 2\pi f_{\mathrm{RF}} = \frac{\sqrt{3}}{2}\frac{1}{\sqrt{L_2 C_2}}. \tag{4.1.1}$$

The second network is designed to resonate at the modulation frequency f_{m}, and it consists of three *L*-*C* tanks with series capacitances C_1 and shunt inductances L_1 (blue elements in Fig. 44). The resonance frequency of this network reads

$$\omega_{\mathrm{m}} = 2\pi f_{\mathrm{m}} = \frac{2}{\sqrt{3}}\frac{1}{\sqrt{L_1 C_1}}. \tag{4.1.2}$$

Note that the complementarity of the networks is necessary in order to obtain two different modulation frequencies: if both networks were of the same type (e.g. series inductance and shunt capacitance), the distinct series and shunt elements would simply add up, resulting in a single resonance.

Eqs. (4.1.1) and (4.1.2) strictly hold when no coupling exists between the corresponding networks. Such a condition is impossible in the setup of Fig. 44. However, it may be possible to minimize the effect of each network on the other, so that Eqs. (4.1.1) and (4.1.2) are approximately correct. This is achieved by selecting the inductances and capacitances as follows

$$\omega_{\mathrm{RF}} L_2 \gg \frac{1}{\omega_{\mathrm{RF}} C_1}, \quad \omega_{\mathrm{RF}} L_1 \gg \frac{1}{\omega_{\mathrm{RF}} C_2}, \tag{4.1.3}$$

$$\omega_{\mathrm{m}} L_2 \ll \frac{1}{\omega_{\mathrm{m}} C_1}, \quad \omega_{\mathrm{m}} L_1 \ll \frac{1}{\omega_{\mathrm{m}} C_2}. \tag{4.1.4}$$

Eq. (4.1.3) makes sure that the total series and shunt impedances at f_{RF} are approximately equal to the impedances of L_2 and C_2, respectively. Similarly, Eq. (4.1.4) makes sure that the total series and shunt impedances at f_{m} are approximately equal to the impedances of C_1 and L_1, respectively. In practice, the "much larger" and "much smaller" conditions of Eqs. (4.1.3) and (4.1.4) are considered to hold if the compared quantities are different by a factor of 10:

$$\omega_{\mathrm{RF}} L_2 = \frac{10}{\omega_{\mathrm{RF}} C_1}, \quad \omega_{\mathrm{RF}} L_1 = \frac{10}{\omega_{\mathrm{RF}} C_2}, \tag{4.1.5}$$

$$\omega_{\mathrm{m}} L_2 = \frac{0.1}{\omega_{\mathrm{m}} C_1}, \quad \omega_{\mathrm{m}} L_1 = \frac{0.1}{\omega_{\mathrm{m}} C_2}. \tag{4.1.6}$$

Eqs. (4.1.5) and (4.1.6) are mutually satisfied if $\omega_{\mathrm{RF}} = 10\omega_{\mathrm{m}}$. Then, solving Eqs. (4.1.1), (4.1.2), (4.1.5) and (4.1.6) yields

$$L_1 = \frac{40}{3} L_2, \quad C_1 = \frac{40}{3} C_2. \tag{4.1.7}$$

The capacitance C_2 is the static capacitance of the varactors. For the varactor model used in our design (Skyworks SMV 1237) and for a static bias voltage of 3 V, $C_2 = 30$ pF. Then, if we choose $f_{\mathrm{RF}} = 150$ MHz, L_2 is selected as 28 nH, according to Eq. (4.1.1), and f_{m} as 15 MHz (10 time smaller than f_{RF}), Furthermore, $L_1 = 370$ nH and $C_1 = 400$ pF, according to Eq. (4.1.7).

The ring needs to be coupled to three external lines through capacitances C_{c}, as explained in the main text. The value of C_{c} determines the *Q*-factor of the ring: the leakage to the external ports increases and the *Q*-factor decreases as C_{c} increases. The *Q*-

factor should be selected so that the intermodulation products fall outside the operation band, a condition which is satisfied if $Qf_m = f_{RF}$. Therefore, here C_c was selected so that the Q-factor is around 10. A coupling inductor was also added in parallel to C_c in order to achieve independent control over the Q-factor at f_m. If such an inductor was not added, the Q-factor at f_m would be much larger than at f_{RF}, due to the larger impedance of C_c, leading to an undesirably high sensitivity with respect to f_m. Note that the sensitivity of the measured structure should be small in order to be able to compensate unpredicted variations in the operation bandwidth of other components in the setup, such as the modulation phase shifters.

The DC signal required for the biasing of the varactors is fed through three separate ports (ports 4, 5 and 6), as shown in the Fig. 44, and choke inductors L_{rfc} are used to prevent the RF and modulation signals from leaking to the DC source. For this purpose, any value larger than $1\ \mu H$ is sufficient. Indeed, the impedance of a $1\ \mu H$ inductor at the RF frequency of 150 MHz is $943\ \Omega$, which is much larger than the impedance $35\ \Omega$ of the varactor C_2, meaning that the RF signal leaking to the DC source is very small. Similarly, the impedance of a $1\ \mu H$ inductor at the modulation frequency of 15 MHz is $94\ \Omega$, which is fairly larger than the impedance $35\ \Omega$ of the inductance L_1, meaning that the modulation signal leaking to the DC source is small. The capacitance C_{dcb} blocks the DC signal from leaking to the ground through L_1, while appearing as a short circuit at RF and modulation frequencies. A value of $10\ \mu F$, corresponding to an impedance of $1\ m\Omega$ and $0.1\ m\Omega$ at 15 MHz and 150 MHz, respectively, is enough for this purpose.

Component	Value	Equivalent Series Resistance (Ω)
C_1	300 pF	0.04
C_2	30 pF @ V_{DC} ~ 3 V	0.25
L_1	270 nH	0.8
L_2	27 nH	0.57
C_c	5.6 pF	0.05
L_c	1 µH	3.8
C_{dcb}	10 µF	-
L_{rfc}	2.7 µH	-

Table 1: Lumped elements used for the realization of the circuit in the Fig. 44.

The values of the lumped elements used in the fabricated layout are listed in Table 1. Notice, that these values are slightly different than the ones calculated before due to restrictions in the available commercial elements. The elements are of 0603 and 0805 surface mount technology (SMT). Furthermore, the circuit was fabricated in a FR4 substrate and the external microstrip lines as well as the ones connecting the elements between themselves were designed to have a characteristic impedance of 50 Ω.

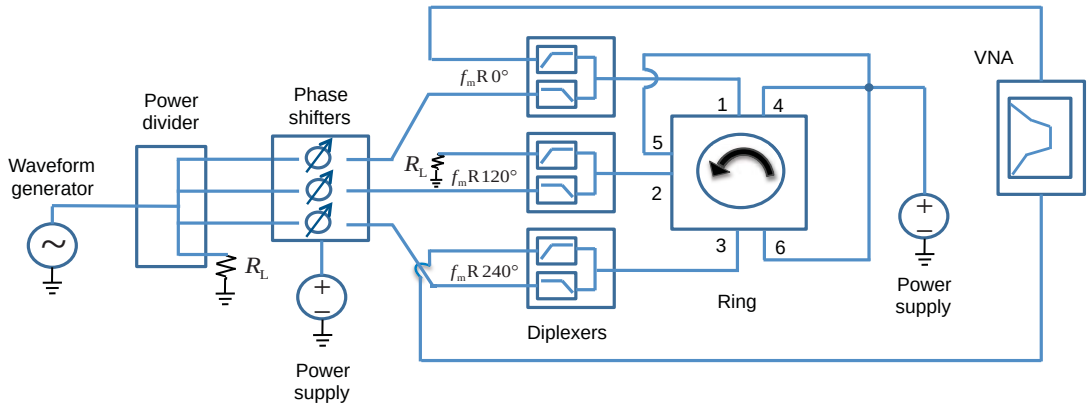

Figure 45: The modulation signals are generated by the waveform generator shown on the left-hand side. The output of the generator is split evenly into three signals through a power divider and then routed to three phase shifters that provide the necessary phase difference of 120° between the modulation signals. The phase shifters are powered with a DC source and potentiometers are used to control their phase. The outputs of the phase shifters are connected to the low-pass ports of three diplexers in order to combine the modulation signals with the RF ones. The high-pass ports of two of the diplexers are connected to the ports of a vector network analyzer (VNA), while the high-pass port of the third diplexer is terminated to a matched load. The outputs of the diplexers are led to ports 1, 2 and 3 of the ring. Rotating the diplexers where the VNA ports are connected allows for the measurement of all the *S*-Parameters of the circuit. The static biasing signal for the varactor is provided by a DC source connected to ports 4, 5 and 6 of the ring [75].

Equipment	Model
Vector Network Analyzer	Agilent E5071C ENA Series
Signal Generator	HP 33120A
Power Supply	Agilent E3631A
Diplexer	Mini-Circuits ZDPLX-2150-S+
Power Divider	Anzac DS-4-4

Table 2: Equipment used during the measurement of the coupled-resonator ring.

The complete experimental setup is shown in the Fig. 45 and a list of the associated equipment is provided in the Table 2. A waveform generator provides the modulation signal, which is split into three equal parts by means of a power divider. The output signals are then led to three phase shifters, which provide the required phase difference of 120° for the modulation signals of the three coupled resonators. The phase shifters are powered by a DC source and their phase shift is controlled via potentiometers. The output of the phase shifters are connected to the low-pass ports of three diplexers, whose output is connected to the RF/modulation ports of the ring. The high-pass ports of two of the diplexers are connected to the VNA ports while the high-pass port of the third diplexer is terminated to a matched load. The diplexers combine the modulation and RF signals and at the same time provide infinite isolation between the RF and modulation paths. By rotating the diplexers, which are connected to the VNA ports, it is possible to measure all the *S*-Parameters of the circuit. The DC signal for biasing of the varactors is provided by a DC source connected to ports 4, 5 and 6 of the ring.

The realized device was designed to resonate at 170 MHz with a Q-factor of about 10 for $V_{\mathrm{dc}} = 1.99\,\mathrm{V}$ and $V_{\mathrm{m}} = 0$. The modulation frequency was set to 15 MHz, in order for the intermodulation by-products at frequencies $\omega \pm \omega_{\mathrm{m}}$, created by the secondary sub-states of $\bar{\mathbf{a}}_{\mathrm{m+}}$ and $\bar{\mathbf{a}}_{\mathrm{m-}}$, to fall outside the resonance band, whose bandwidth is here around 10 MHz. Fig. 46 shows a photograph of the experimental setup and the fabricated prototype. We underline here the deeply subwavelength size of the realized device (~ $\lambda/75$), simply based on three lumped resonant circuit tanks.

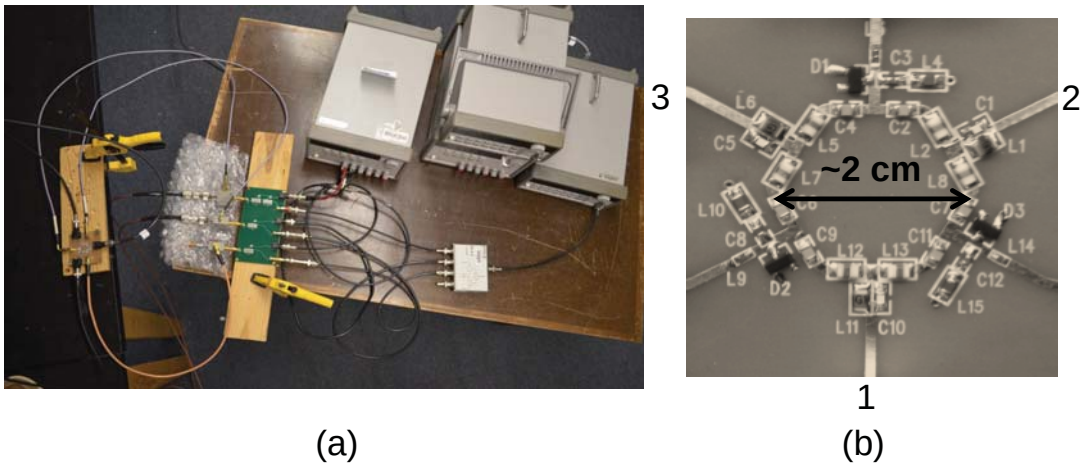

Figure 46: (a) Full experimental setup and (b) Fabricated prototype [75]. The maximum dimension of the structure is 2 cm, corresponding to an electrical size of $\lambda/75$ at 200 MHz.

Without modulation, the signal is equally split at the two output ports, as expected from symmetry, and the system is fully reciprocal (Fig. 47(a)). When the modulation signal is switched on, the symmetry is broken and power is unequally split. By varying the modulation amplitude it is possible to find a value for which all the energy entering port 1 is routed to port 3, corresponding to $\phi_{\mathrm{R}} = -\phi_{\mathrm{L}} = \pi/6$. This condition is satisfied for

$V_m = 0.6$ V, as can be seen in Fig. 47(b): at the resonance frequency of 170 MHz, power incident to ports 1, 2 and 3 is routed to ports 2, 3 and 1, respectively, demonstrating the operation of an ideal, magnetic-free, deeply subwavelength linear circulator. For comparison, Fig. 47(c) shows the *S*-parameters obtained using full-wave and circuit simulations: the agreement with the measurement is excellent.

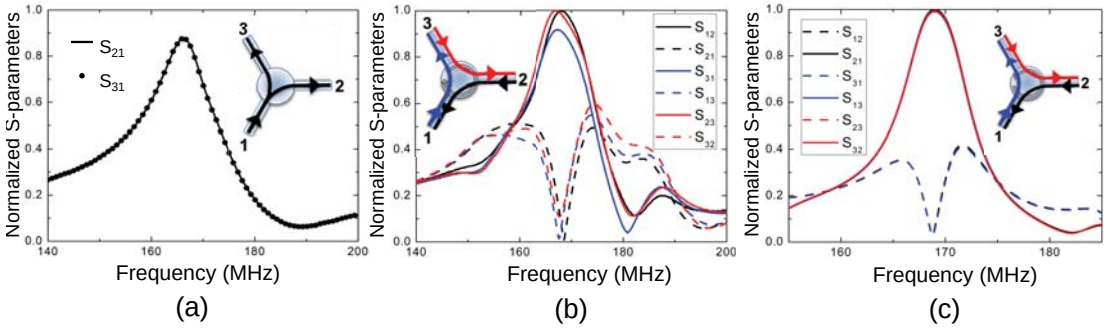

Figure 47: Response versus frequency [75]. (a) Measured transmission from port 1 to ports 2 and 3 without modulation ($V_m = 0$ V). The power is equally split to the output ports. (b) Measured scattering parameters when $V_m = 0.6$ V. Incident power to ports 1, 2 and 3 is transmitted to ports 3, 1 and 2, respectively, thus realizing a three-port circulator. (c) Simulated response of the loop for the case of panel (b): excellent agreement between theory and experiment is observed. All results correspond to $V_{dc} = 1.99$ V.

In order to get a deeper insight into the effect of V_m on the device operation, Fig. 48(a) shows the transmission between ports 1 and 2 at resonance versus V_m. For $V_m = 0$, $S_{21} = S_{12}$, as expected. Increasing V_m results in a decrease of S_{21} and an increase of S_{12} until $V_m = 0.6$ V, where $S_{21} = 0$. Past this point, S_{21} and S_{12} get closer, as expected when we depart from the destructive interference condition. For very large values of V_m, S_{21} and S_{12} both tend to zero, since the counter-rotating states move far from $\omega_\pm$ and, therefore, are weakly excited at $\omega_\pm$. The magnitude of the asymmetry between S_{21} and

S_{12} is measured by the isolation $|S_{12}/S_{21}|$, plotted in Fig. 48(b) in logarithmic scale versus V_{m}. At the optimum modulation voltage $V_{\mathrm{m}} = 0.6$ V, S_{12} is over 4 orders of magnitude larger than S_{21}, indicating giant non-reciprocity, well above the levels of any commercial magnetic-based device.

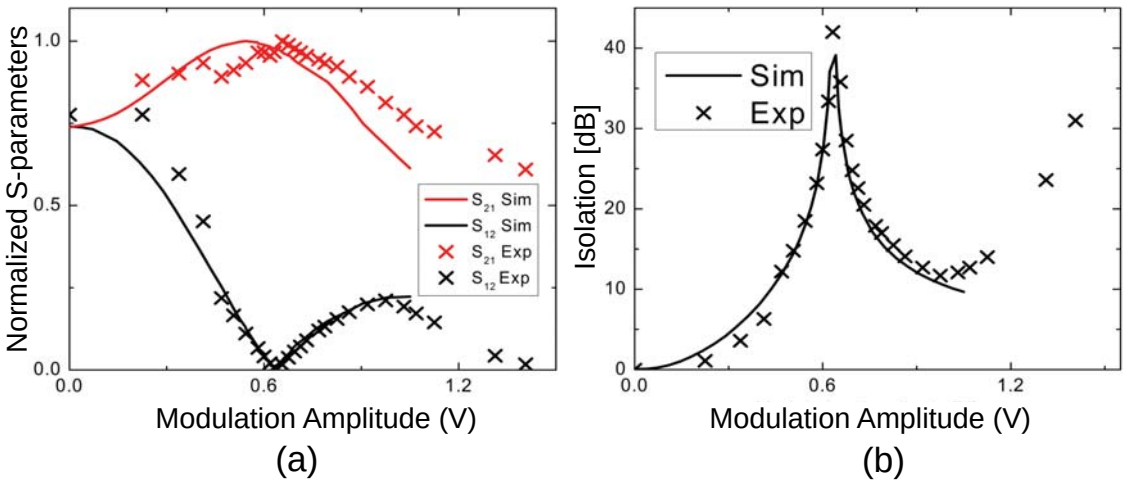

Figure 48: Response versus modulation [75]. (a) Measured and simulated transmission between ports 1 and 2. Transmission is different for opposite propagation directions, indicating non-reciprocity. Maximum contrast is observed for $V_{\mathrm{m}} = 0.6$ V. The results correspond to $V_{\mathrm{dc}} = 1.99$ V. (b) Isolation (S_{12}/S_{21}) in logarithmic scale for the same biasing conditions as in panel b. For $V_{\mathrm{m}} = 0.6$ V, the difference between S_{12} and S_{21} is over four orders of magnitude.

Despite the impressive isolation provided by the design in Fig. 44, there are drawbacks that led to a re-evaluation of the design. The concept of angular-momentum-induced non-reciprocity was experimentally demonstrated in [75] through a ring of capacitively-modulated *L*-*C* resonators, as in Fig. 49(a). The most straightforward way to realize a modulated capacitor is through a varactor and a diplexer, as in Fig. 49(b). If the

transmission phase between the high-frequency and common ports of the diplexer is zero, the input impedance at the high-frequency port is equal to the impedance of the modulated varactor. Furthermore, the diplexer makes sure that the modulation and input signals do not mix with each other outside the varactor. Although functional, the circuit in Fig. 49(b) has a major drawback: the diplexer is part of the resonant network – the input signal needs to go through the diplexer in order to reach the varactor – potentially complicating the design and detrimentally affecting the overall performance. For this reason, [75] followed an alternative approach to move the diplexers outside the resonant circuit. By combining the circuit in Fig. 49(a) with a dual one consisting of shunt inductors and series capacitors, the ring in [75] was designed to resonate at both the input and modulation frequencies, thus eliminating the need of separate modulation lines and diplexers. Such an approach led to very large isolation (more than 50 dB), but also quite large insertion loss (22 dB). The reason is that, in order to avoid interference between the main and modulation sub-circuits of the ring, the modulation frequency had to be selected quite far from the input frequency, forcing the circulator to operate in the sub-optimal bottom-left area in Fig. 38. Indeed, from the data provided in [75], it can be found that the corresponding circuit operates at point A in Fig. 38.

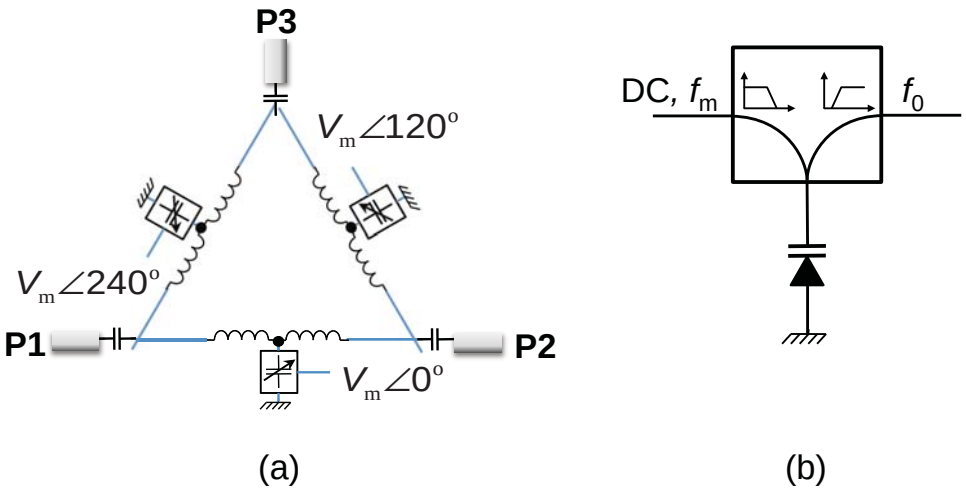

Figure 49: Circulator based on a ring resonator [29], as in [75]. (a) Ring of capacitively-modulated *L*-*C* resonators. (b) Implementation of a variable capacitor through a varactor and a diplexer.

The aforementioned problems related to the ring topology may be overcome using the wye topology in Fig. 50(a). Modulation can be achieved by connecting varactors between filters, as in Fig. 50(b), which provide a low-impedance path for the DC and modulation signals, while they exhibit very large impedance for the input signal. A simple implementation of such a filter involves a parallel combination of a choke inductor (L_{rfc}), which provides a low-impedance path for the DC signal, and a series *L*-*C* band-pass filter (L_{bpf} and C_{bpf}), which, if designed to resonate at the modulation frequency, provides a low-impedance path for the modulation signal. Furthermore, the filter is designed to have large impedance at the resonance frequency of the circuit, in order to block the input signal. For the filters connecting the circuit ports and the inductors *L*, such as the filter on the left-hand side of the varactor in Fig. 50(b), this

condition is satisfied if $Z_{\text{filter}}(\omega_0) \gg Z_0$, where $Z_{\text{filter}}(\omega_0)$ is the filter impedance at the circuit resonance frequency ω_0, considering that, at ω_0, the impedance at the position of the filters looking towards the ports and the varactors is Z_0 and $Z_0/2$, respectively. Through a similar analysis, it is possible to show that the condition $Z_{\text{filter}}(\omega_0) \gg Z_0$ is also sufficient to minimize the flow of the input signal through the filter connected at the center node of the circuit [filter at the right-hand side of the varactor in Fig. 50(b)]. Filters can also be connected between the external lines and the inductors of the wye circuit in order to prevent the modulation signals from leaking to the external lines. These filters can be simple parallel *L*-*C* band-stop filters (L_{bsf} and C_{bsf}), which, although exhibiting a narrow bandwidth, they can effectively block the monochromatic modulation signal. Interestingly, none of the filters in the wye-circuit design intercepts the path of the input signal inside the resonant circuit formed by the varactors and the inductors L, and as a result their effect on the operation of the device at the input frequency is expected to be minimal.

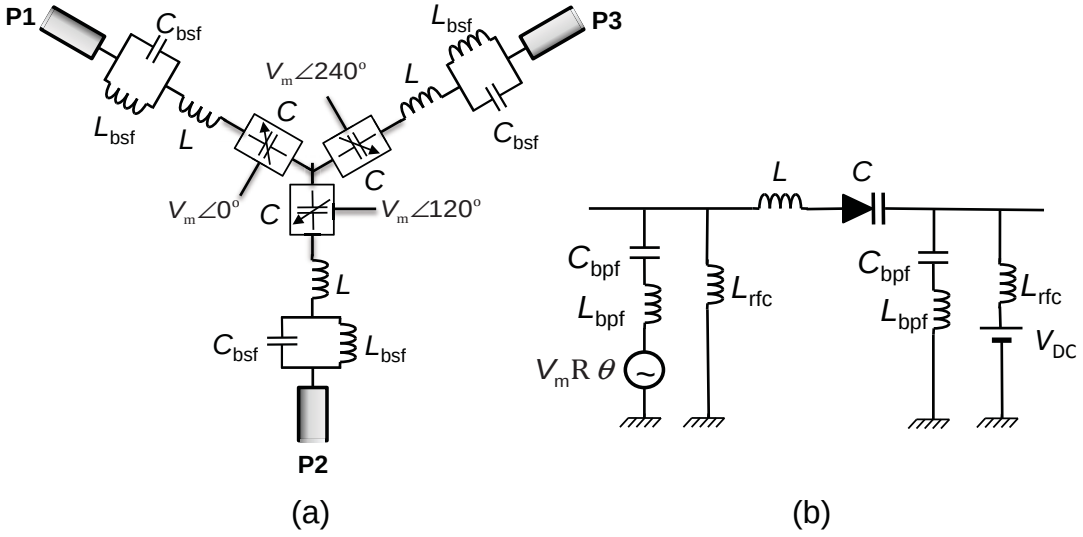

Figure 50: Circulator based on a wye resonator [29]. (a) Capacitively-modulated lumped-element wye resonator. The parallel *LC* bandstop filters (L_{bsf} and C_{bsf}) are used to prevent the modulation signal from leaking to the external lines. (b) Implementation of the variable capacitors through varactors and filters that create a low-impedance path for bias and modulation signals, while they block the input signal.

The resonant states of the wye resonator can be calculated by terminating the transmission lines with matched loads, and assuming no external excitation. Conservation of charge at the center node of the circuit demands that the total charge of the three capacitors is zero. This fact excludes the presence of a common state, which would require all the capacitors to have the same charge and, as a result, the total charge to be non-zero. On the other hand, charge conservation is satisfied by the rotating states, since for such states the total charge is by definition zero, as a result of their three-fold symmetry, with 120 deg phase difference between different resonators. The three-fold

symmetry of the rotating states also requires that the voltage at the center node of the circuit is zero. Then, considering that at resonance the current flow is non-zero, the total impedance of each branch is zero, yielding

$$\begin{aligned} \omega_{\pm} &= \sqrt{\frac{1}{LC} - \frac{Z_0^2}{4L}}, \\ \gamma_{\pm} &= \frac{Z_0}{2L}, \end{aligned} \tag{4.1.8}$$

where Z_0 is the characteristic impedance of the transmission lines. For $\gamma_{\pm} \ll \omega_{\pm}$, i.e., for a circuit with a large Q-factor, $\omega_{\pm} \approx 1/\sqrt{LC}$. Then, a capacitance perturbation δC_{m} produces a frequency perturbation $\delta\omega_{\mathrm{m}} = \omega_0 \delta C_{\mathrm{m}}/(2C)$. Loss in the inductors and varactors can be represented by a series resistance R, and in such a case Z_0 in (4.1.8) should be replaced by $Z_0 + R$. It is obvious that $Z_0/(2L)$ and $R/(2L)$ correspond to the leakage and loss decay rates, $\gamma_{\pm,\mathrm{cpl}}$ and $\gamma_{\pm,\mathrm{loss}}$, respectively. Then, the corresponding Q-factors read $Q_{\mathrm{cpl}} = \sqrt{L/C}/Z_0 = \omega_{\pm} L/Z_0$ and $Q_{\mathrm{loss}} = \sqrt{L/C}/R = \omega_{\pm} L/R$. The fact that the wye resonator does not have a common state indicates that the coupled-mode analysis in Section 3.1 is only restricted by the parametric oscillation condition $\omega_{\mathrm{m}} \approx 2\omega_{\pm}$. A full circuit analysis for the wye resonator, including modulation and excitation from the external lines, is presented in Section 3.3.

Component	Value	Equivalent Series Resistance	Self-Resonance Frequency
L	560 nH	~ 12 Ω at 200 MHz (Q-factor of 55)	600 MHz
C	Skyworks SMV1233 V_{dc} ~ 4.5 V	1.2 Ω	–
L_{bpf}	Coilcraft 1.5 μH	–	190 MHz
C_{bpf}	American Technical Ceramics 11 pF	~ 0.05 Ω	~ 4 GHz
L_{rfc}	Coilcraft 1.5 μH	–	190 MHz

Table 3: Lumped elements values for the circuit in Fig. 50.

Based on the above analysis, we designed a circulator for operation at 200 MHz ($\omega_{\pm} = 200$ MHz), with a target resonance bandwidth of 10% ($Q = 10$). Considering that R can be much smaller than Z_0 for good-quality inductors, we find that the values of L and C that satisfy these specifications are 400 nH and 1.6 pF, respectively. Based on these values and commercially available components, we choose the lumped elements listed in Table 3. Furthermore, the modulation frequency is chosen as 40 MHz, resulting in operation at point B in Fig. 38, where the insertion loss and intermodulation products are 3.1 dB and –16 dB, respectively. Note that at 200 MHz the inductors L_{bpf} and L_{rfc} operate above self-resonance, and as a result, their effective response at this frequency is capacitive and very lossy. However, since their impedance is very large, they can still

efficiently prevent the input signal from leaking to the modulation lines. This fact shows that for the wye topology, contrary to the ring topology, it is not necessary for the filter components to operate optimally at both the modulation and input frequencies, thereby significantly relaxing the design constraints. Note that, for simplicity purposes, in the proof-of-concept design presented here, the band-stop filters used to prevent the modulation signals from leaking to the external lines [filters L_{bsf}-C_{bsf} in Fig. 50(a)] are omitted. The effect of these filters on the input signal is minimal, since the capacitors C_{bsf}, through which the input signal primarily flows, have a self-resonance frequency much larger than the operation frequency.

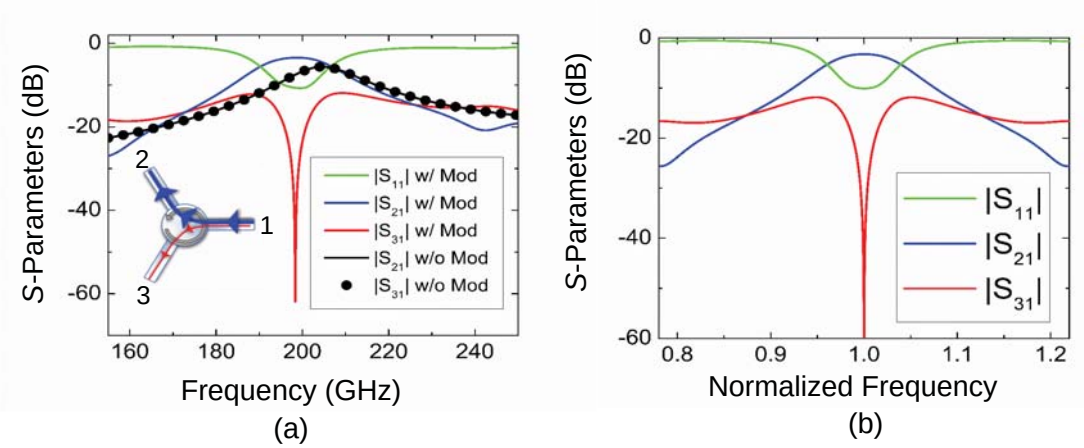

Figure 51: Scattering parameters for the lumped-element wye resonator without modulation and under the optimum modulation condition [29]. (a) Full-wave simulations. (b) Coupled-mode analysis.

Fig. 51 presents the *S*-parameters with and without modulation as obtained through full-wave simulations and the coupled-mode equations presented in Section 3.1. Simulations were performed by considering full SPICE models for the varactors and the filter inductors, while inductors L were modeled through a series combination of

inductances and resistances, as listed in Table 3, considering that these inductors operate well below their self-resonances. Without modulation, the input power is equally split to the output ports. When modulation is applied, the signal is transmitted to port 3 with insertion loss of about 3.4 dB, a little larger than at point B in Fig. 38, due to additional loss introduced by the filters, while the power transmitted to port 2 is negligible (isolation is larger than 50 dB), showing a remarkable improvement in the performance compared to the ring topology. The numerical results are in excellent agreement with the theoretical ones, apart from a slight shift in the resonance frequency in simulations when the modulation is applied. As shown in Section 3.3, this is a second-order effect with respect to δC_{m} that cannot be captured by first-order coupled-mode theory.

Fig. 51 shows that the circuit exhibits a return loss of –10 dB, which, although not ideal, can be considered acceptable for practical applications. An interesting question that now arises is whether the return loss may be reduced by impedance matching. Matching the proposed circulator is equivalent to matching a lossy device, considering that intermodulation conversion in the proposed circulator is by all means a loss channel at the fundamental frequency, given the overall passivity of the device. Ideal matching of a lossy three-port circulator is possible only if the common mode of the circulator can absorb power. This can be proven by considering that the *S*-matrix of a lossy circulator with infinite isolation reads

$$\mathbf{S} = \begin{pmatrix} S_{11} & 0 & S_{21} \\ S_{21} & S_{11} & 0 \\ 0 & S_{21} & S_{11} \end{pmatrix}. \tag{4.1.9}$$

Then, it is not difficult to show that the eigenvalue associated with the common mode of the system, i.e., the reflection coefficient of the common mode, is given by $S_{11}+S_{21}$ and, as a result, the power absorbed by the common mode is equal to $1-\left|S_{11}+S_{21}\right|^2$. It is clear that zero reflection, $S_{11}=0$, is only possible if the common mode can absorb power, as mentioned before. For the simple wye resonators considered here such an effect is impossible, because these resonators do not support a common mode at all. Nevertheless, according to (3.1.30), it is possible to achieve very small values of S_{11} if the modulation parameters are appropriately selected so that S_{21} is close to unity. Total reflection cancellation may be possible by adding networks between the ports and the branches of the circulator that allow the excitation of a common mode. However, this is not a trivial problem and falls beyond the scope of the present work.

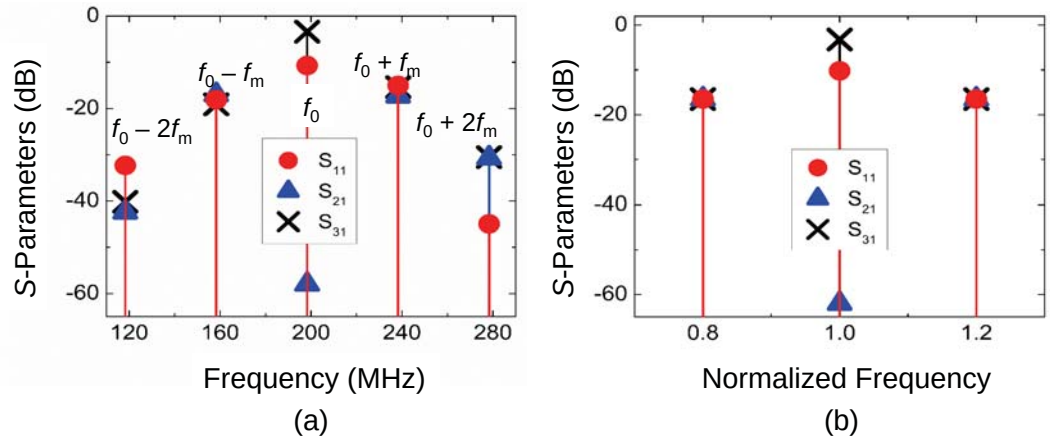

Figure 52: *S*-parameters at input and intermodulation frequencies in the case of the lumped-element resonator, for the modulation condition in Fig. 51 [29]. (a) Full-wave simulations. (b) Coupled-mode analysis.

Intermodulation frequencies are unavoidable by-products of the proposed concept and, therefore, it is important to know how strong they are. Fig. 52 plots the *S*-parameters

at the center frequency f_0 and the inter-modulation frequencies $f_0 \pm nf_m$, for the modulation parameters in Fig. 51. Both in simulations and theory, the first-order intermodulation products $f_0 \pm f_m$ are about 14 dB lower than the output power, a bit higher than at point B in Fig. 38(c), due to additional loss in the filters. Numerical simulations reveal the existence of additional higher-order intermodulation products $f_0 \pm nf_m$ with $n > 1$, which result from higher-order modulation terms at frequencies nf_m, due to the non-linear response of the varactors. These products are much weaker than the first-order intermodulation products and they are completely absent for perfectly linear varactors, as shown in Section 3.1.

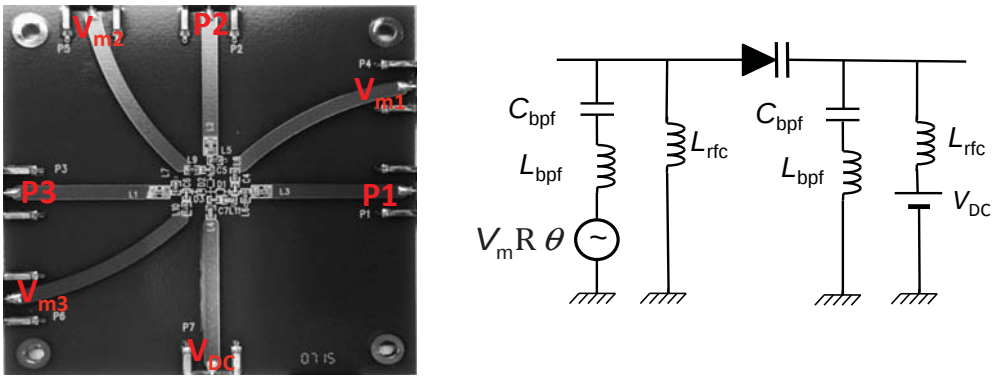

Figure 53: Realized wye resonator [29]. (a) Measured scattering parameters when V_m = 1.28 V and the DC biasing= 1.7 V. (b) Simulated response, now including shift in inductance for the filter inductors. (c) Experimental prototype of wye resonant circulator.

The circuit in Fig. 50(a) was realized on a printed circuit board, as shown in Fig 53(a). Modulation of the varactors was achieved through the circuit in Fig. 53(b), which is different from the one in Fig. 50(b) with respect to the position of the filters L_{bpf}-C_{bpf}-

L_{rfc}. In particular, in Fig. 53(b) these filters are connected at the varactors' anodes, while in Fig. 50(b) they are connected between the external lines and the inductors L. At a first glance, this difference may look not important for the circulator operation. However, a closer inspection reveals that the impedance at the position of the filters towards the circuit ports in the circuit of Fig. 53(b) is $Z_0 + R + i\omega_0 L$, instead of Z_0 as in Fig. 50(b) and, as a result, the condition $Z_{\mathrm{filter}}(\omega_0) \gg Z_0$ may not be sufficient. Indeed, for the lumped-element values in Table 3, the modulation circuit in Fig. 53(b) leads to a resonance at 150 MHz, instead of 200 MHz as for the modulation circuit in Fig. 50(b). Furthermore, insertion loss with the circuit in Fig. 53(b) is larger than with the circuit in Fig. 50(b), due to the significant loss of L_{bpf} and L_{rfc} at the input frequency, and the fact that the input signal can now flow through these inductors. Loss can be reduced by reducing the resonance frequency, since inductor loss typically decreases as frequency decreases. For the fabricated circuit, loss becomes minimum for a DC bias voltage of 1.1 V and a resonance frequency of 130 MHz.

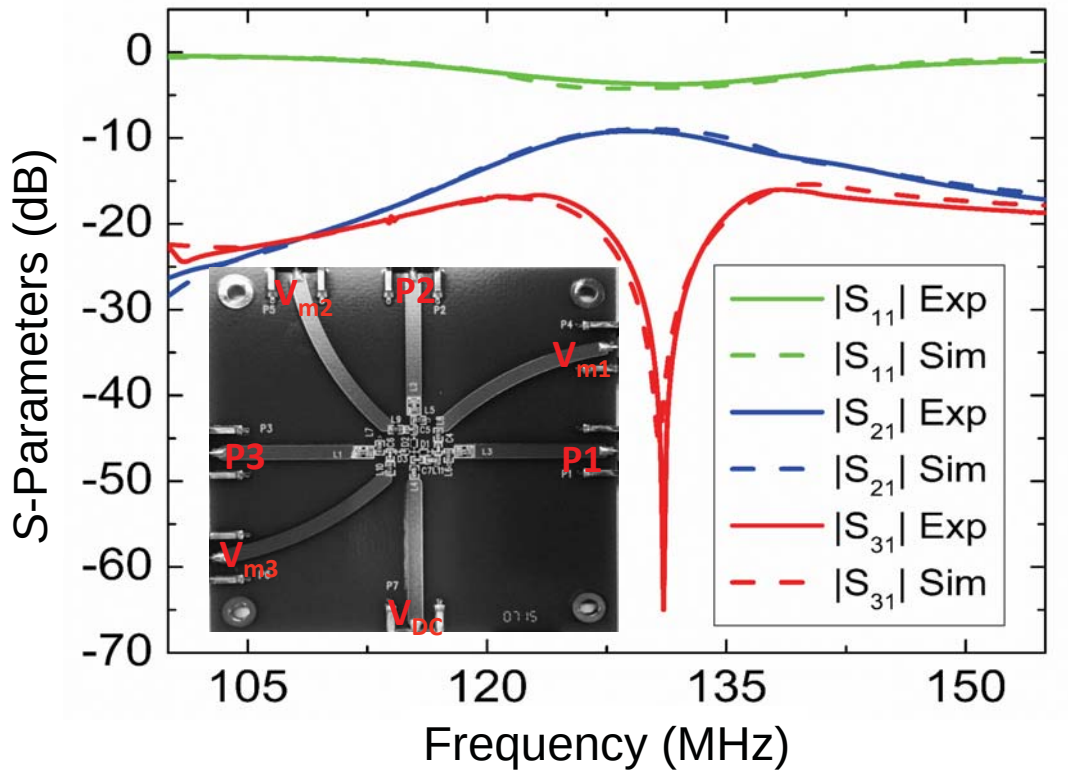

Figure 54: Experimental and numerical results for the circuit in Fig. 50(a) with the modulation network in Fig. 53(b) [29]. The lumped-element values are the same as in Table 3.

Measured and simulated *S*-parameters for this geometry are presented in Fig. 54. These results provide a clear experimental demonstration of the non-reciprocal properties of the lumped-element wye circulator in Fig. 50(a), with isolation exceeding 50 dB. Furthermore, although insertion loss is larger than in Fig. 51, due to the sub-optimal connection of the filters L_{bpf}-C_{bpf}-L_{rfc}, as explained before, it is significantly smaller than in the preliminary design [75], which was based on the ring topology in Fig. 49(a). It is also worth noticing the good agreement between experimental and numerical results,

even in terms of fine features, such as the small bump at 140 MHz, which is related to the dispersive characteristics of L_{bpf} and L_{rfc}[1]. The good agreement between experimental and numerical results is a strong indication that the numerical results in Fig. 51, corresponding to optimal connection of the filters L_{bpf}-C_{bpf}-L_{rfc}, are practically achievable.

4.2 AM CIRCULATOR – DISTRIBUTED-ELEMENT DESIGN

The circulator presented in the previous section is based on lumped elements and, as such, it is ideal for low-frequency applications. However, as the frequency increases, lumped components exhibit poorer performance, or they are totally unavailable. For this reason, in this section we present a distributed design for wireless-communications band (~ 2.2 GHz), which, like the lumped-element design, is based on the wye topology, but with inductors now replaced by transmission-line sections, as in Fig. 55. The wye resonator is coupled to external lines through the capacitors C_{cpl}. The modulation network is identical to the lumped-element case, with the only variation in the position of the band-stop filters, which are now connected between the external lines and the coupling capacitors.

[1] This small bump disappears, if L_{bpf} and L_{rfc} are modeled as a series combination of dispersion-less inductances and resistances.

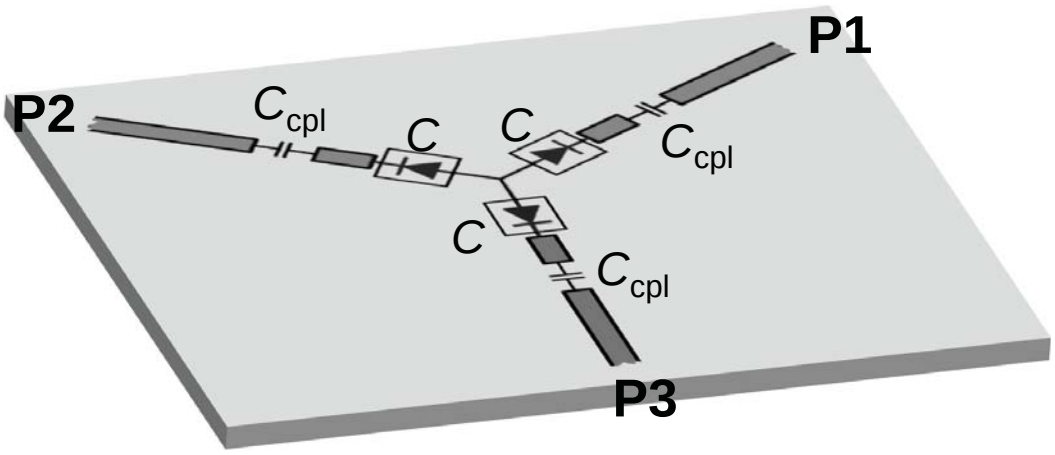

Figure 55: Circulator based on a distributed wye resonator for high-frequency operation [29]. The varactors and adjacent transmission line sections provide the resonance of the circuit, while the capacitors C_{cpl} couple the resonator to the external transmission lines.

Neglecting the coupling to external lines ($C_{cpl} \to 0$), the input impedance of the transmission-line section from the side of the varactors reads $Z_{TL} = iZ_0 \cot(\beta l)$, where Z_0, β and l are the characteristic impedance, wavenumber and length of the transmission line segments. Similar to the lumped-element case, the input impedance of each branch as seen from the center node of the circuit should be zero at resonance, resulting in

$$Z_0 \cot(\beta l) + \frac{1}{\omega C} = 0, \tag{4.2.1}$$

which is satisfied if the length of the transmission-line sections is between a quarter and half wavelength. In reality, the resonance frequency is slightly lower than

what predicted by (4.2.1), due to the coupling capacitors. The frequency perturbation due to a change in the varactor capacitance can be calculated from (4.2.1). In particular, by taking the derivative of (4.2.1) with respect to C it can be shown that

$$\delta\omega_0 = -\omega_0 \frac{\delta C}{2C} \frac{2}{1+\beta_0 l[\omega_0 Z_0 C + 1/(\omega_0 Z_0 C)]}, \tag{4.2.2}$$

where ω_0 is the resonance frequency and β_0 the corresponding transmission-line wavenumber. Considering that $\omega_0 Z_0 C + 1/(\omega_0 Z_0 C) \geq 2$ and $\beta_0 l \geq \pi/2$, we find that $|\delta\omega_0| \leq \omega_0 \, \delta C/(4C)$, which shows that, in the case of the distributed element design, the frequency perturbation is smaller than in the case of the lumped-element design, where $\delta\omega_0 = -\omega_0 \, \delta C/(2C)$, by at least a factor of two.

Parameter	Value
Substrate	Rogers 4350
Substrate thickness	0.762 mm
Microstrip width	1.55 mm
Microstrip thickness	0.043 mm
Microstrip length	22 mm

Element	Value	Equivalent Series Resistance	Self-Resonance Frequency
C	Skyworks SMV1234 V_{dc} ~ 4 V	0.8 Ω	–
C_{cpl}	0.3 pF	0.15 Ω	20 GHz
L_{bpf}	Coilcraft 56 nH	–	2.07 GHz
C_{bpf}	2.85 pF	0.15 Ω	7 GHz
L_{rfc}	Coilcraft 56 nH	–	2.07 GHz

Table 4: Geometrical parameters and lumped element values for the circuit in Fig. 55.

Based on (4.2.1), we designed a circulator for operation at 2.2 GHz. The geometrical parameters of the structure and the values of the lumped elements are provided in Table 4. The structure is selected to operate at point C in Fig. 38, where insertion loss is less than 2.5 dB and intermodulation products are –20 dB. For $Q_{\text{loss}} = 160$, which was calculated by fitting coupled-mode theory to simulations in the case without modulation[1], we found that the modulation frequency would be 400 MHz.

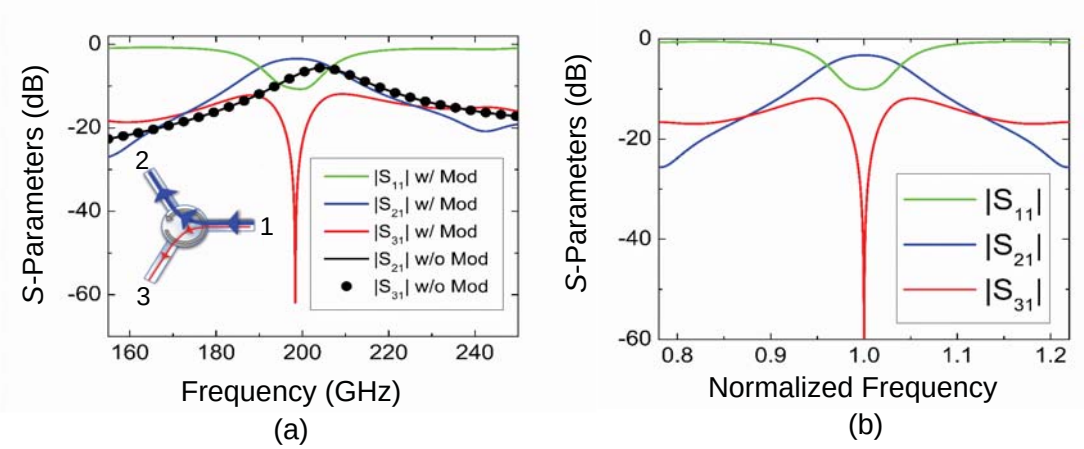

Figure 56: Scattering parameters for the distributed wye resonator without modulation and under the optimum modulation condition [29]. (a) Full-wave simulations. (b) Coupled-mode analysis.

[1] Transmission in the case without modulation can be found by substituting (3.1.25) into (3.1.26) with $\omega_{\text{m}} = \delta\omega_{\text{m}} = 0$ as $S_{21} = (2/3)\gamma_{\text{cpl}}/[-i(\omega-\omega_0)+\gamma]$. By fitting this expression to numerical results, we can calculate γ and γ_{cpl}. Then $\gamma_{\text{loss}} = \gamma - \gamma_{\text{cpl}}$ and $Q_{\text{loss}} = \omega_0/(2\gamma_{\text{loss}})$. Note, that the value of the coupling capacitor is not important for the calculation of Q_{loss}, because Q_{loss} is an inherent property of the resonator.

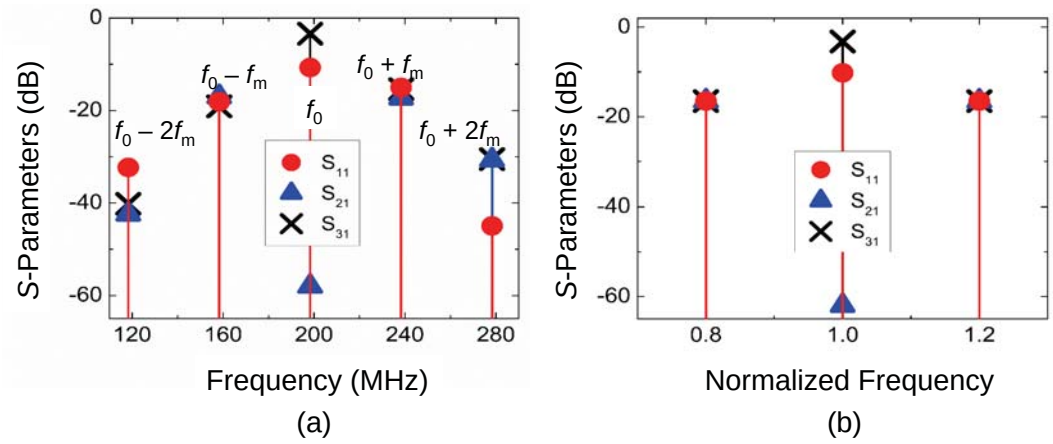

Figure 57: *S*-parameters at input and intermodulation frequencies in the case of the distributed wye resonator, for the modulation condition in Fig. 56 [29]. (a) Full-wave simulations. (b) Coupled-mode analysis.

Fig. 56 shows the *S*-parameters of the structure for the optimum modulation condition. Results are similar to the lumped element case, apart from a slight asymmetry in the simulated resonance curves, resulting from a higher-order resonance above 3 GHz, which does not exist in the lumped-element design. This asymmetry is not visible in the theoretical results, because this higher-order mode is neglected in coupled-mode analysis. Fig. 57 shows the *S*-parameters at the center and intermodulation frequencies, for the modulation condition in Fig. 56. The intermodulation product at $f_0 - f_m$ is 20 dB below the main signal at f_0, in perfect agreement with Fig. 38(c), while the intermodulation product at $f_0 + f_m$ is slightly larger than $f_0 - f_m$, due to the asymmetry created by the higher-order resonance.

4.3 BANDWIDTH ENHANCEMENT FOR ANGULAR-MOMENTUM-BIASED CIRCULATORS

Previously, it was shown that the isolation and insertion loss of an angular-momentum circulator is related to the decay rates, both due to losses and external line coupling, and the modulation frequency. More explicitly, the modulation requirements to achieve optimal isolation are inversely proportional to the quality factor of the resonance. From this intrinsic relationship, the question arises: Is it possible to extend the instantaneous bandwidth of the device, which is entangled with the quality factor of the resonance, while maintaining reasonable modulation requirements?

Prior to addressing the question regarding angular-momentum-biasing bandwidth, it is helpful to consider other microwave structures with similar limitations. Transmission line (TL) impedance matching networks in microwave networks, for example the quarter-wave transformer, are simple, passive designs. However, these matching schemes present a tradeoff between the effectiveness of the matching (minimum reflection coefficient) and the bandwidth. Alternatively, binomial or Chebyshev cascaded matching sub-sections are utilized in an effort to improve the bandwidth performance [23]. Here, we will show that the same principles used to broaden TL matching be applied to improve the instantaneous bandwidth of an angular-momentum circulator.

Consider two angular-momentum-biased circulators with individual resonances ($\omega_{1,2}$), where the scattering parameters are (repeated from Section 3.1 for clarity)

$$\begin{aligned} S_{11}(\omega) &= \sqrt{2\gamma_c/3}\left[a_+^{(0)} + a_-^{(0)}\right] - 1, \\ S_{21}(\omega) &= \sqrt{2\gamma_c/3}\left[a_\pm^{1,2} e^{i2\pi/3} + a_\pm^{1,2} e^{-i2\pi/3}\right], \\ S_{31}(\omega) &= \sqrt{2\gamma_c/3}\left[a_\pm^{1,2} e^{i4\pi/3} + a_\pm^{1,2} e^{-i4\pi/3}\right], \end{aligned} \tag{4.3.1}$$

are found from the coupled-mode equations

$$a_{\pm}^{1,2} = \sqrt{2\gamma_c/3}\,\frac{-i(\omega-\omega_{1,2}\mp\omega_{\mathrm{m}})+\gamma}{[-i(\omega-\omega_1)+\gamma][-i(\omega-\omega_{1,2}\mp\omega_{\mathrm{m}})+\gamma]+\delta\omega_{\mathrm{m}}^2/4},$$
$$\delta\omega_{\mathrm{m}} = 2\sqrt{\frac{\gamma(\omega_{\mathrm{m}}^2+\gamma^2)}{\omega_{\mathrm{m}}\sqrt{3}-\gamma}}, \tag{4.3.2}$$

where the total decay rate is the sum of the loss and leakage coupling rates ($\gamma = \gamma_c + \gamma_l$), ω_{m} is the modulation frequency, and $\delta\omega_{\mathrm{m}}$ is the optimum coupling coefficient. If we assume two circulators are translated about a center frequency (ω_0) by a fixed value $\Delta\Omega$, then the resonant poles of each circulator may be found as $\omega_{1,2} = \omega_0 \mp \Delta\Omega$.

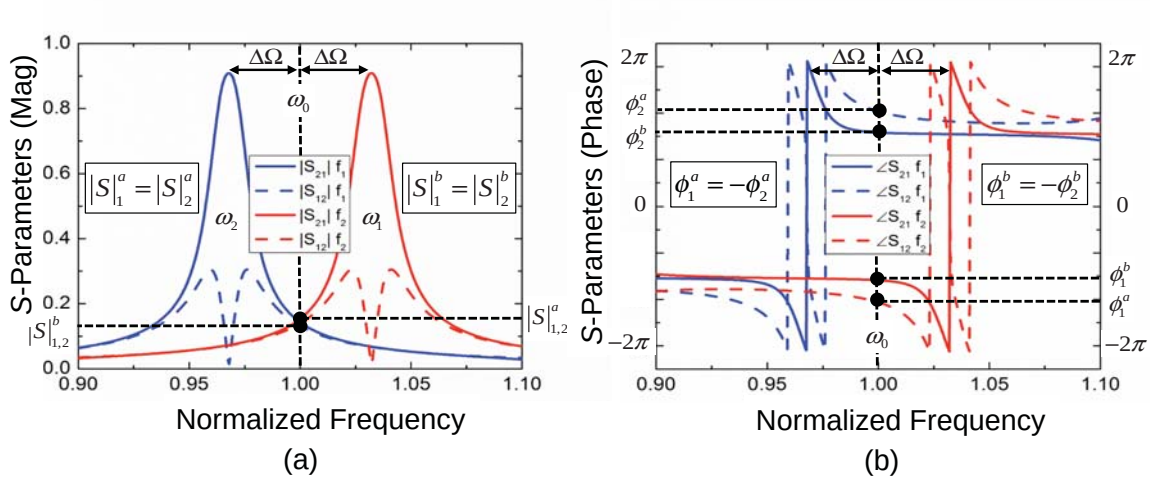

Figure 58: Scattering response for two, non-reciprocal resonators tailored for a symmetric response around a desired frequency. When evenly spaced about the desired center frequency (ω_0), the transmitted (S_{21}) and isolated (S_{12}) signals are identical, but translated about the center by a frequency shift, $\Delta\Omega$. (a) The magnitude response is equal and (b) the phase is opposite for the lower (ω_1) and higher (ω_2) frequency resonators. In order to provide cancellation of the isolated signal, and thus expand the breadth of the device's performance, one must subtract the individual ports for each resonator.

The scattering response of such as system is shown in Fig. 58, where the isolated (transmitted) path is shown as S_{12} (S_{21}) in dashed lines (solid), and the higher (lower) resonant circulator at ω_1 (ω_2) is shown in red (blue). From this figure, it is clear that the magnitude for each circulator is identical, for both signal paths, at ω_0 with even symmetry. Alternatively, the two-way response for the two circulators is completely out of phase, with odd symmetry about ω_0. In order to expand the instantaneous bandwidth of the complete structure, alignment notwithstanding, one must cancel the isolated signal paths, and therefore subtract the signal paths of the two circulators.

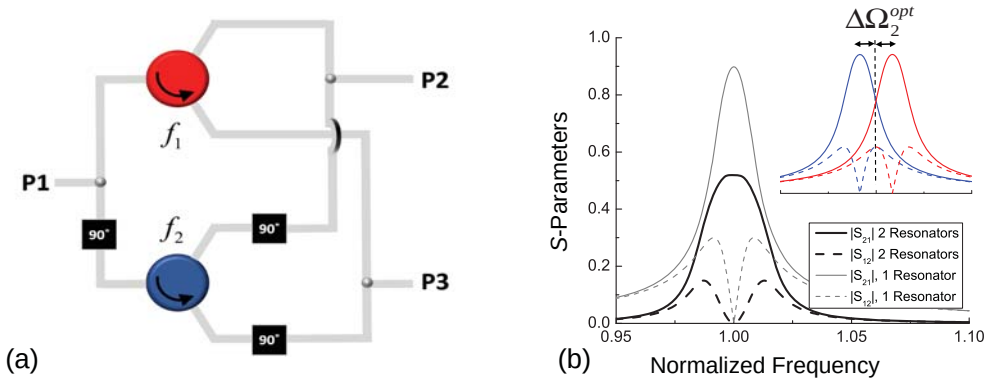

Figure 59: Bandwidth enhancement with two resonators at optimum spacing. (a) Abstract layout for macro-circulator based on two independent circulators, with 90˚ phase blocks for the necessary signal cancellation. (b) Combined (single resonator) scattering response, shown in black (grey), as calculated from the coupled-mode theory expressions for the angular-momentum circulator. When the frequency separation is optimum ($\Delta\Omega_2^{opt}$) for two resonators (shown in inset), we obtain a complete null at ω_0, but with a less pronounced side-bands offsetting the null. Alternatively, the combined transmission signal no longer achieves the maximum due to the matching of the side bands, which is located outside the maximum transmission for the individual resonator.

An abstract electrical schematic tailored for bandwidth enhancement is pictured in Fig. 59(a). Here, we have two circulators, symmetrically resonating about a center frequency with the color scheme matching the response presented in Fig 58. In order to provide the signal cancellation required, three 90° hybrids are connected to the signal lines of lower resonant circulator (ω_2). One may consider replacing the three 90° hybrids with two 180° hybrids, but the symmetry of the system will be broken and a full circulator scattering response will be lost.

The expression in (4.3.2) is under the condition of optimum isolation at the center of the resonance, leading to the null found in the scattering plots. When we invoke the scattering cancellation technique for two angular-momentum circulators, the conditions for isolation are not only related to the device parameters ($\omega_m, \delta\omega_m, \gamma$), but the frequency separation of the two resonators, $\Delta\Omega$. One would expect the cancellation of the sidebands found in the isolated signal paths is related to the quality factor, Q, of the resonator ($Q = \omega_0 / (2\gamma)$). A closer investigation of the scattering for the macro-circulator will validate the relationship between the quality factor and frequency separation.

The scattering response for an angular-momentum-biased circulator is based on the mixing of modes, where hybrid sub-states consists of primary and secondary states, leading to the complex expressions in (4.3.1) and (4.3.2). Assuming the modulation frequency (ω_m) is large enough, the energy distributed in secondary states is negligible, and the scattering may be approximated by a simple, two state system. Then, the scattering expressions for the primary states may be described as

$$S_{21} = \frac{2}{3}\left(\frac{e^{i4\pi/3}}{\left(1 + i\frac{\omega - \omega_1}{\gamma_1}\right)} + \frac{e^{i2\pi/3}}{\left(1 + i\frac{\omega - \omega_2}{\gamma_2}\right)} \right)$$
$$S_{12} = \frac{2}{3}\left(\frac{e^{i2\pi/3}}{\left(1 + i\frac{\omega - \omega_1}{\gamma_1}\right)} + \frac{e^{i4\pi/3}}{\left(1 + i\frac{\omega - \omega_2}{\gamma_2}\right)} \right), \quad (4.3.3)$$

where the frequency split in the degenerate modes is introduced by the resonant frequencies and decay rates, $\omega_{1,2}$ and $\gamma_{1,2}$. The expressions in (4.3.3) are commonly used to describe magnetic-biased circulators [79], where the resonant frequencies are satisfied by the condition, $\omega_{\pm} = \omega_0 \pm \gamma_{\pm}/\sqrt{3}$. For simplification, we will assume the decay rates, and thus quality factors, are identical for both circulators.

Assuming two non-reciprocal resonators are equally offset from the center resonance by $\Delta\Omega$, as shown in Fig. 58, then the total scattering response may be found by the difference of the two signals, $S_{21}^T = S_{21}^1 - S_{21}^2$ and $S_{12}^T = S_{12}^1 - S_{12}^2$. The introduction of the frequency shift $\Delta\Omega$ leads to a change of variable, where the resonant frequencies are now described as $\omega_{\pm}^1 = \omega_0 - \Delta\Omega \pm \gamma/\sqrt{3}$ and $\omega_{\pm}^2 = \omega_0 + \Delta\Omega \pm \gamma/\sqrt{3}$. The combination of the two isolated ports leads to the power expression

$$\left|S_{21}^T\right|^2 = \frac{-j6Q^3\Delta\Omega^3\omega_0^3\left(3Q^2\Delta\Omega^2 - \omega_0^2\right)}{\left(9Q^4\Delta\Omega^4 + 3Q^2\Delta\Omega^2\omega_0^2 + \omega_0^4\right)^2}. \quad (4.3.4)$$

Assuming complete cancellation at the center of the band ω_0, and thus infinite isolation ($S_{21}{}^T \rightarrow 0$) and normalized frequency, then the relationship between the quality factor and the optimum frequency shift for ideal signal cancellation of the isolated port is

$$\Delta\Omega_2^{opt} = \frac{1}{\sqrt{3}Q}. \tag{4.3.5}$$

The simple expression in (4.3.5) is merely an approximation for angular-momentum-biased circulators, yet provides a close representation useful for physical implementation of the signal cancellation technique.

The combined scattering response for two combined angular-momentum circulators is shown in Fig. 59(b). The circulator parameters closely resemble the design presented in Section 4.1 and 4.2, where the operation is customized for Wi-Fi operation (f_0 = 2.4 GHz, f_m = 450 MHz, Q = 68). The results are based on the expressions in (4.3.1) and (4.3.2), as developed from the complete coupled-mode theory. A frequency separation of $\Delta\Omega_2^{opt} = 0.0088$ resulted in a broadened null in the isolation port (black dashed); within 4% of the approximate expression developed in (4.3.5). For clarity, the individual scattering response at $\Delta\Omega_2^{opt} = 0.0088$ is displayed in the inset of Fig. 59(b). Compared to the scattering of a single circulator (grey), the side bands are less pronounced, with a gradual null at ω_0. Whereas the isolation has been improved, the combined transmission suffers some attenuation due to the signal cancellation. Since the optimum cancellation occurs where the sidebands are aligned, the main transmission peaks no longer overlap, leading to a reduction in transmission.

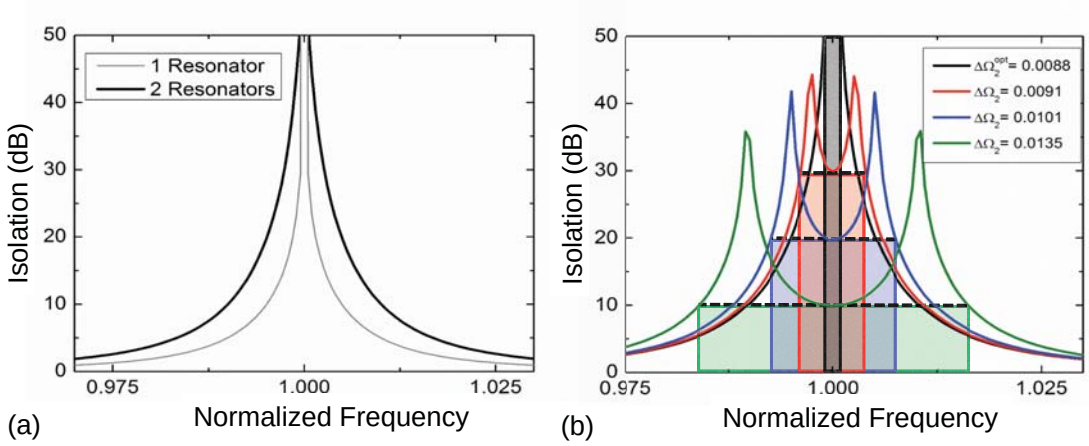

Figure 60: Isolation for a two resonator, macro-circulator. (a) Combined (single resonator) isolation response, shown in black (grey), as calculated from the coupled-mode theory expressions for the angular-momentum circulator at optimum frequency separation ($\Delta\Omega_2^{opt}$). (b) Various frequency spacing with their respective isolation response. By reducing the requirement for infinite isolation at ω_0, we may extend the instantaneous bandwidth. As the frequency spacing is increased, the local minima becomes more pronounced, thus limiting the maximum isolation across the operating band.

For a design based on two circulator, the corresponding isolation for optimum separation is shown in Fig. 60(a). The isolation for two resonators (black) follows the same Lorentzian form as a single resonance (grey) circulator, but with a broad pole at ω_0. The improvement in bandwidth is evident, with 366% increase for 30 dB and 230% for 20 dB. If the requirements for ideal isolation are reduced (maximum isolation at ω_0), then improvement in instantaneous bandwidth will be even larger. In Fig. 60(b), performance is shown for various isolation thresholds: ideal (black), 30 dB (red), 20 dB (blue), and 10 dB (green). As previously presented, the optimum frequency spacing $\Delta\Omega_2^{opt}$ generates a single isolation peak at ω_0. As the frequency spacing increases, a local minima is introduced, which grows with an increased $\Delta\Omega$. In this circumstance, the sidebands are

no longer aligned, with maximum cancellation occurring further away from the center point. The bottom of the local minima, determined by the amount of shifting past the optimum operating point, determines the maximum isolation within the band. For example, we obtain five times the bandwidth for 30 dB isolation, as highlighted by the shaded red region in Fig. 60(b), and a 226% improvement in bandwidth for a constraint of 10 dB isolation, as shown in green.

To validate the concept, signal cancellation of two angular-momentum circulators was simulated in Agilent ADS. The angular-momentum circulator consists of three microstrip transmission line stub resonators, each loaded with Skyworks SMV1234 varactor diodes at the center, and connected to the external lines though coupling capacitors. Three 90° hybrids, each designed to operate at ω_0, were included in the design simulation. A detailed presentation of the angular-momentum transmission line circulator is found in Section 4.2. By adjusting the DC biasing conditions of two identical circulators, we may tune the location of each resonance. Once the static biasing is identified, each circulator must be optimized to provide an optimum and congruent response. For simplicity, we fixed the modulation frequency for both resonators (here, f_m = 350 MHz) and only adjusted the modulation amplitude (related to $\delta\omega_m$) in order to tune each circulator at a given resonance.

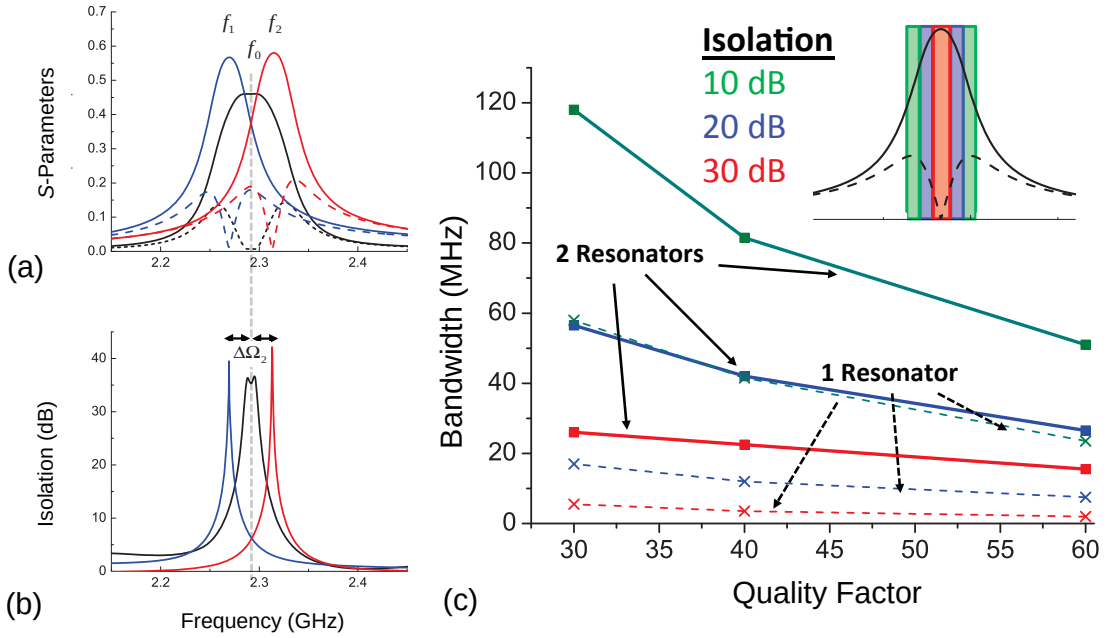

Figure 61: Simulated results for a two resonator, macro-circulator. (a) Simulated scattering response and (b) isolation for the two resonator, combined (two individual resonator) circulator, shown in black (blue and red). The results are in good agreement with the theory predicted from the coupled-mode expressions. (c) Simulation illustrating the bandwidth for various quality factors, for 10, 20 and 30 dB of isolation. Naturally, the instantaneous bandwidth will increase as the quality factor for the resonators is reduced, especially for lower isolation thresholds.

The combined circulator scattering response (black), along with the individual resonator (red and blue), is shown in Fig. 61(a). Here, the coupling capacitors are 0.22 pF, culminating in a quality factor of 60. As predicted from the coupled-mode theory, the signal cancellation, when circulators are properly spaced, creates a broadened null at the center of the two resonances. The isolation performance, seen in Fig. 61(b), is also broadened, with over 35 dB centered at 2.292 GHz. The isolation may be optimized at the center, but in an effort to maximize bandwidth, isolation of 35 dB was chosen as the

threshold. For isolation above 30 dB, the simulations illustrated a bandwidth improvement from 2.4 MHz to 15 MHz; over five times as large as a single circulator. The frequency spacing of the simulation is 0.009, which closely matches the coupled-mode theory predictions ($\Delta\Omega_2 = 0.0091$) and the expression in (4.3.5) ($\Delta\Omega_2 = 0.0096$). Due to the non-linearity of the varactor diodes, each circulator will not be completely symmetric in the scattering response for different DC biasing conditions, in particular the sidebands of the isolation, thus limiting the effectiveness of the cancellation process. This may be improved, which will be discussed in Section 4.4.

By adjusting the coupling capacitance, we may manipulate the quality factor and related bandwidth. In Fig. 61(c), the operational bandwidth for lower Q circulators is shown, for both a single circulator (dashed lines) and the combined, two-resonator structure (solid lines). Depending on the requirements of a given application, this process is translatable for a desired quality factor. It should be noted, however, that phase cancellation with a passive, 90° hybrid will break down for significantly low Q-factors. For significant bandwidth, the signal cancellation will fall out gradually, unless other phase cancellation processes are considered.

It is reasonable to expand the signal cancellation process to more resonators, as the case with higher order multi-section matching, if there is some tangible benefit. If the process is expanded to four resonators, centered about a center frequency f_0, then the signal summation may be expressed as $S_{21}^{T} = (S_{21}^{1} + S_{21}^{3}) - (S_{21}^{2} + S_{21}^{4})$ and $S_{12}^{T} = (S_{12}^{1} + S_{12}^{3}) - (S_{12}^{2} + S_{12}^{4})$, as depicted in Fig 62(a). With the same approach developed for the two-resonator cancellation process, the scattering parameters for four angular-momentum circulators are combined to provide the total response (black) seen in Fig. 62(b). For

comparison, the scattering for a single resonator is shown in grey and the optimum spacing between resonators is shown in the inset. Here, we assume equal spacing between all four resonators. Alternative, more complex shifting may lead to more efficient scattering response, but not considered in the scope of the presented research.

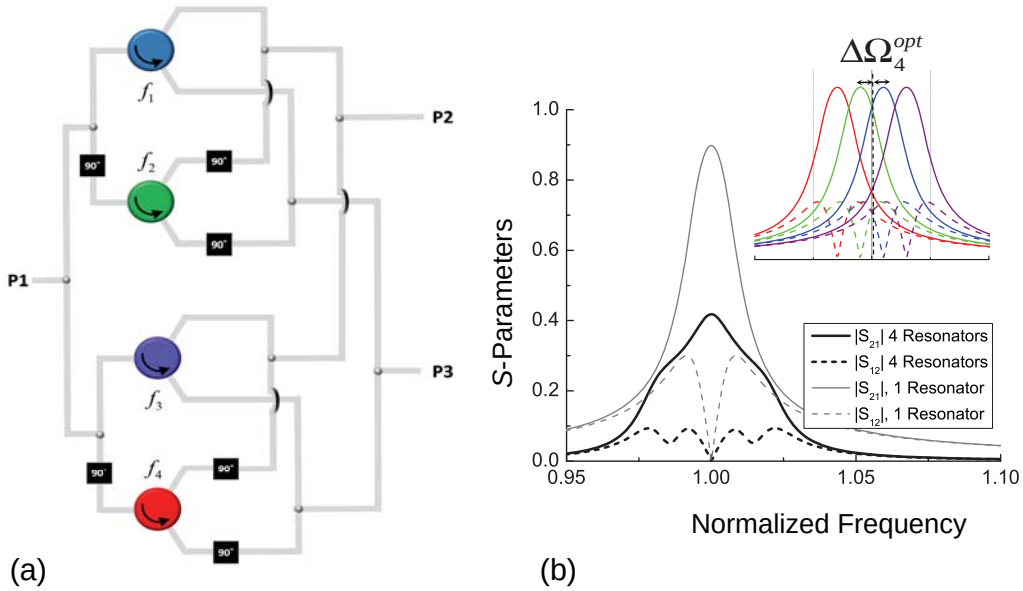

Figure 62: Bandwidth enhancement with four resonators at optimum spacing. (a) Abstract layout for macro-circulator based on four independent circulators, with 90˚ phase blocks for the necessary signal cancellation. (b) Combined (single resonator) scattering response, shown in black (grey), as calculated from the coupled-mode theory expressions for the angular-momentum circulator. When the frequency separation is optimum ($\Delta\Omega_4^{opt}$) for four resonators (shown in inset), we obtain a complete null at ω_0. Similar to the two resonant circulator, there is a reduction in the total transmission (S_{21}) and rippling is observed in the isolation signal (S_{12}).

The maximum transmission is reduced, as in the case with two resonators, due to the separation of the combined signals from the center. The effect is more pronounced

than the two-circulator combined; here, the spacing between subtracted signals is greater at the optimal operational condition $\Delta\Omega_4^{opt} = 0.0026$. The isolation improvement, displayed in Fig. 63(a), is minimal for values over 30 dB; however, two local minima, symmetric about the center frequency, provide enhanced performance for lower isolation tolerance. For 10 dB of isolation, the four combined resonators lead to a 280% increase in bandwidth. By reducing the frequency spacing from the optimal condition (red trace in Fig. 63(b)), the rippling in the isolation response is reduced, resulting in a smooth, 15 dB isolation across the band. The local minima continue to grow past the optimum spacing, eventually leading to discrete, isolation regions, which is not desired.

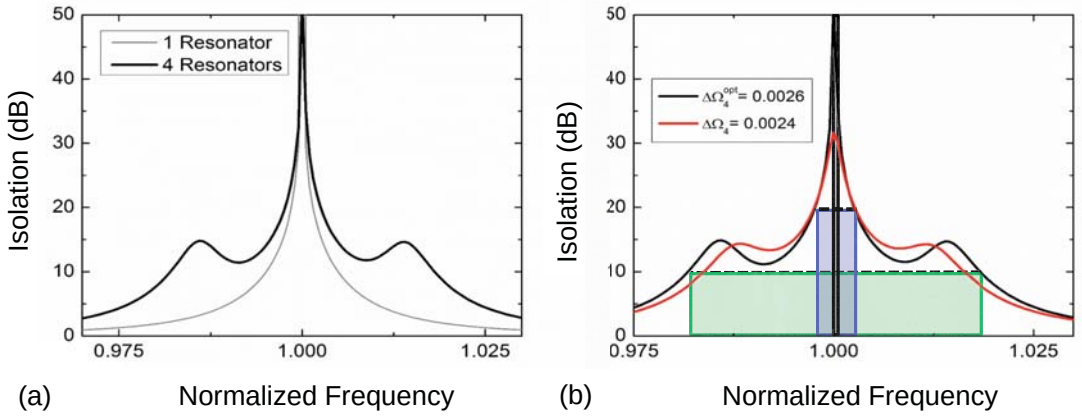

Figure 63: Isolation for a four resonator, macro-circulator**.** (a) Combined (single resonator) isolation response, shown in black (grey), as calculated from the coupled-mode theory expressions for the angular-momentum circulator at optimum frequency separation ($\Delta\Omega_4^{opt}$). (b) Various frequency spacing with their respective isolation response. If minimal rippling (local minima) is desired (red curve), then the $\Delta\Omega$ should be smaller than the optimum case (black). However, the optimum frequency spacing results in the largest bandwidth for a 10 dB isolation threshold and peak isolation at ω_0.

4.4 IMPROVING LINEARITY

The angular-momentum-biasing technique requires a form of modulation, which may be accomplished with variable capacitors. Varactors are non-linear elements and, as such, they are also expected to affect the maximum power that can be handled by the device. Fig. 64 presents the output power and third-order intermodulation distortion versus the input power for an input signal consisting of two tones centered at 200 MHz for the lumped element device of Fig. 50, for which isolation is maximum.

The capacitance for a two-port varactor is expressed as

$$C(V) = \frac{K}{\left(\phi + V_{DC}\right)^n}, \tag{4.4.1}$$

where K is the capacitance constant, n is the power law exponent, ϕ the built-in junction potential, and V_{DC} is the applied voltage. As in any non-linear circuit, power saturation and intermodulation distortion are second-order non-linear effects, related to the third power of the excitation signal or, in the case of varactors, to the coefficient C_2 in the polynomial expansion $C = C_0 + C_1 v + C_2 v^2 + \ldots$ of the varactor capacitance around the DC biasing point, V_{dc}. C_2 depends on V_{dc}, but not on the modulation signal, showing that modulation does not affect the non-linear properties of the structure. Ideally, we would like to completely cancel C_2, which is however impossible with simple varactors, like the ones used here. Nevertheless, C_2 decreases as V_{dc} increases, making possible to reduce non-linear distortion by increasing V_{dc}.

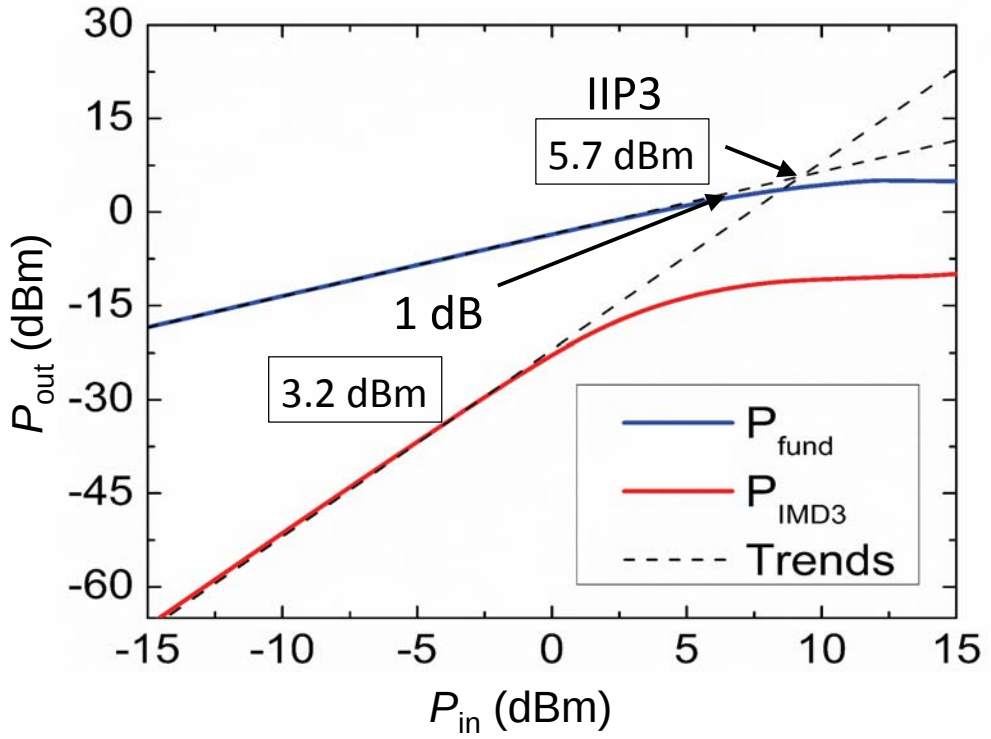

Figure 64: Non-linear distortion in the case of the lumped-element wye resonator of Fig. 50(a) for excitation with a dual-tone signal, with frequencies centered at 200 MHz and separated by 1.5 kHz [29]. The results correspond to full-wave simulations.

In order to understand this property better, we consider a particular example of a silicon hyperabrupt varactor, like the ones used in our design, with C-V relation $C_0 = C_{J0}/\sqrt{1+V/V_0}$, where C_{J0} is the junction capacitance and V_0 the built-in voltage. In such scenario, $C_2 = 3C_0/[8(V_0+V_{dc})^2]$, implying that, if V_0+V_{dc} is increased by a factor of four and C_{J0} by a factor of two (the area of the varactor junction is increased by the same factor), C_2 is reduced by a factor of 16, implying an improvement of 12 dB for the maximum power handled by the device. A drawback of this approach is that C_1, which

determines the capacitance modulation, also decreases as V_{dc} increases, making necessary the use of a larger modulation voltage. In the previous example, $C_1 = -C_0/[2(V_0 + V_{dc})]$, implying that for an increase of $V_0 + V_{dc}$ by a factor of four the modulation voltage also is required to increase by the same factor. This trade-off between modulation voltage and maximum input power may be overcome through more advanced varactor topologies, such as the ones recently proposed in [80], where non-linear distortion and capacitance modulation can be independently controlled.

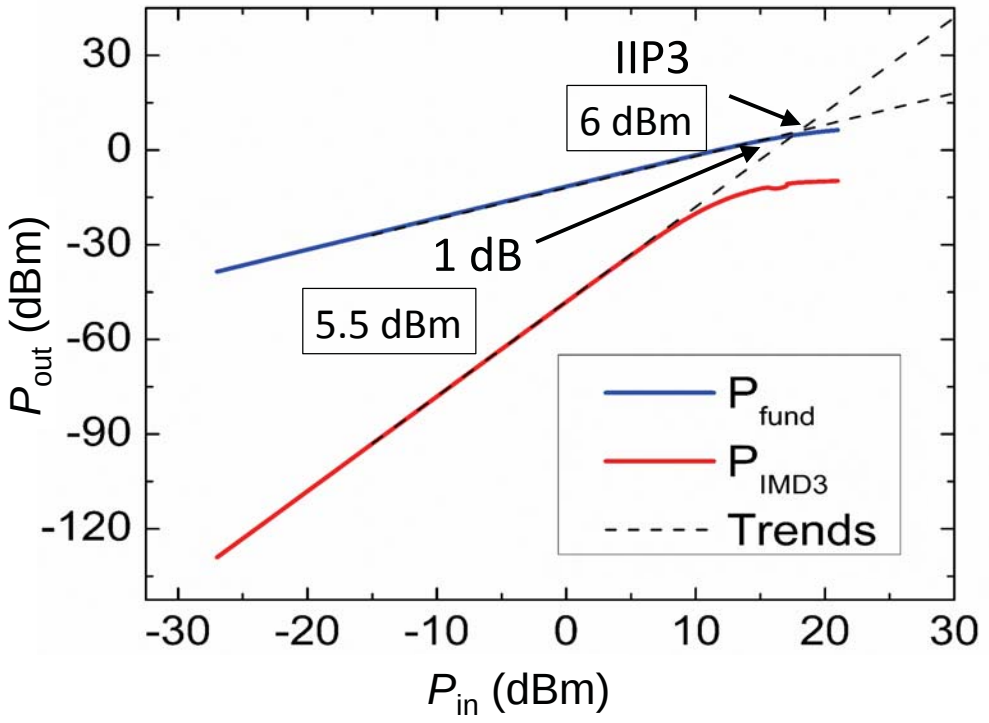

Figure 65: Non-linear distortion in the case of the distributed wye resonator for excitation with a dual-tone signal, with frequencies centered at 2.2 GHz and separated by 15 kHz [29]. The results correspond to full-wave simulations.

Fig. 65 shows non-linear distortion for excitation by a pair of tones centered at 2.2 GHz for a transmission-line based circulator. Fig. 65 shows the non-linear distortion for excitation by a pair of tones centered at 2.2 GHz. The maximum input power is slightly larger than in the lumped-element case, which is attributed to the larger V_{DC} (V_{DC} = 4 V) and the smaller Q-factor in the distributed design.

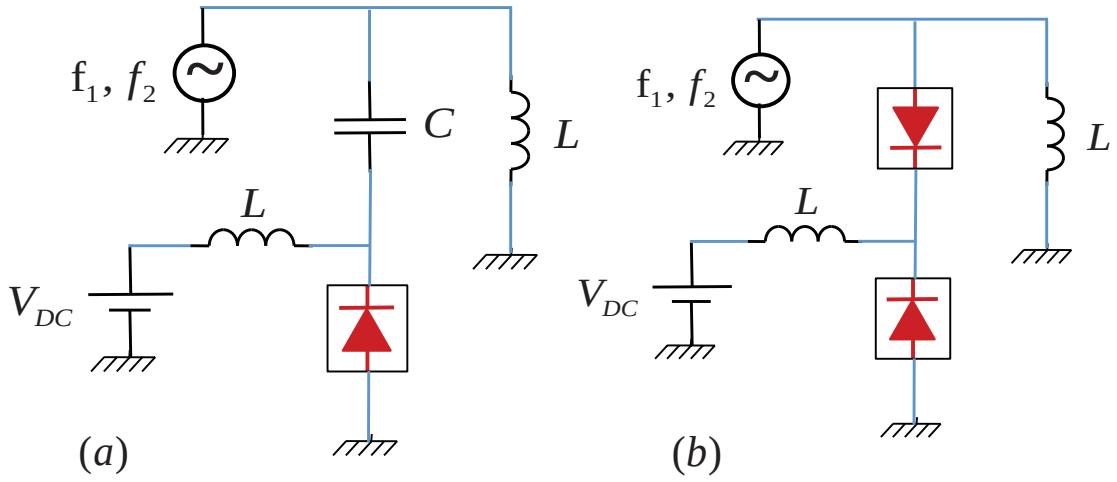

Figure 66: Modulation topologies. (a) Single and (b) anti-series varactor modulation schemes.

The trade-off between modulation voltage and maximum input power may be overcome through more advanced varactor topologies, such as the ones recently proposed in [80],[81], where non-linear distortion and capacitance modulation can be independently controlled. Instead of using a single varactor to provide the modulation, an anti-series topology is used, where two varactor diodes are mirrored with a center tap biasing. The two varactor topologies are illustrated in Fig. 66. With the anti-series topology, all higher order distortion terms (C_1, C_2, …) vanish under ideal circumstances,

when the power law exponent is $n = 0.5$. If an alternative value for n is required, then the opposing diodes must be scaled appropriately in order to minimize C_2.

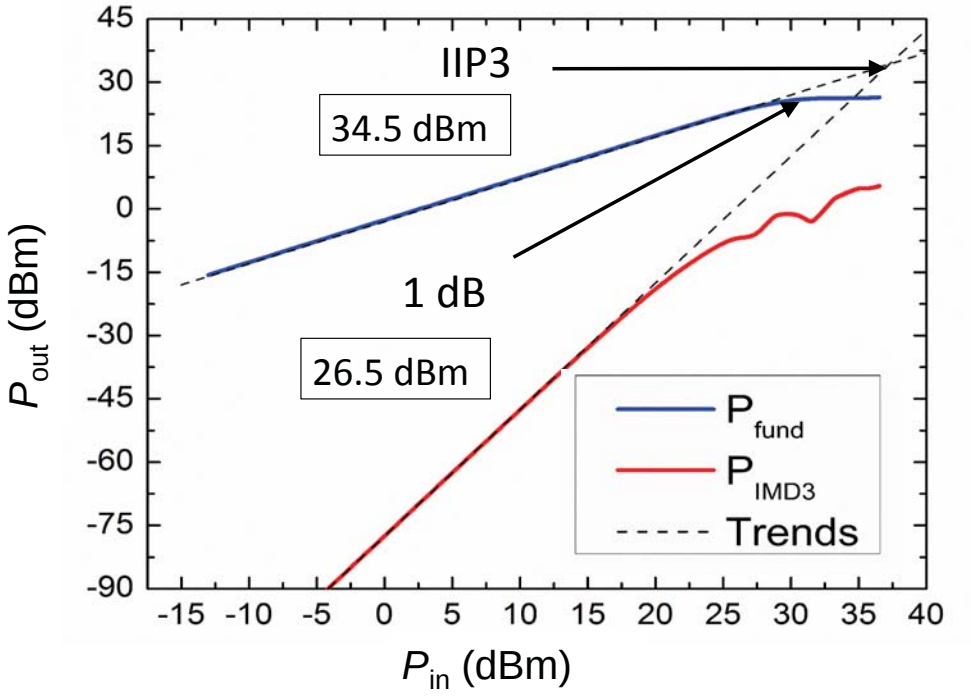

Figure 67: Non-linear distortion in the case of the anti-series distributed wye resonator for excitation with a dual-tone signal, with frequencies centered at 2.13 GHz and separated by 15 kHz. The results correspond to full-wave simulations.

In order to validate the linearity improvement principles descried in this section, an anti-series transmission line circulator was designed. The same physical stub resonator layout from Fig. 55 was applied, but with the new varactor scheme and larger biasing conditions. Here, the diodes were selected for a junction capacitance of 4.2 pF, DC bias of 11 V, and modulation amplitude of 12 V, in order to maintain a similar frequency response as the TL circulator in Fig. 56 ($f_0 \sim 2.2$ GHz). The resulting linearity plot for maximum isolation in Fig. 67 presented a substantial improvement in linearity, where the

1 dB compression point is now approximately 30 dBm input power. It is evident that operating a higher biasing conditions, along with more complex modulation topologies, significantly improve linear performance of the angular-momentum-biased circulator.

Chapter 5 Tunability for Angular-Momentum-Biased Circulators and RADAR Pulse Tracking

5.1 Tunability for Angular-Momentum-Biased Circulator

Another unique property of the proposed device consists in its real-time tunability features. The biasing voltage V_{dc}, which provides the reverse biasing condition for the varactor diodes, determines their static capacitance, as pictured in Fig. 68(a). Therefore, V_{dc} can be used to actively control the static resonance frequency of the *L*-*C* tanks, and consequently the frequency band over which non-reciprocity occurs.

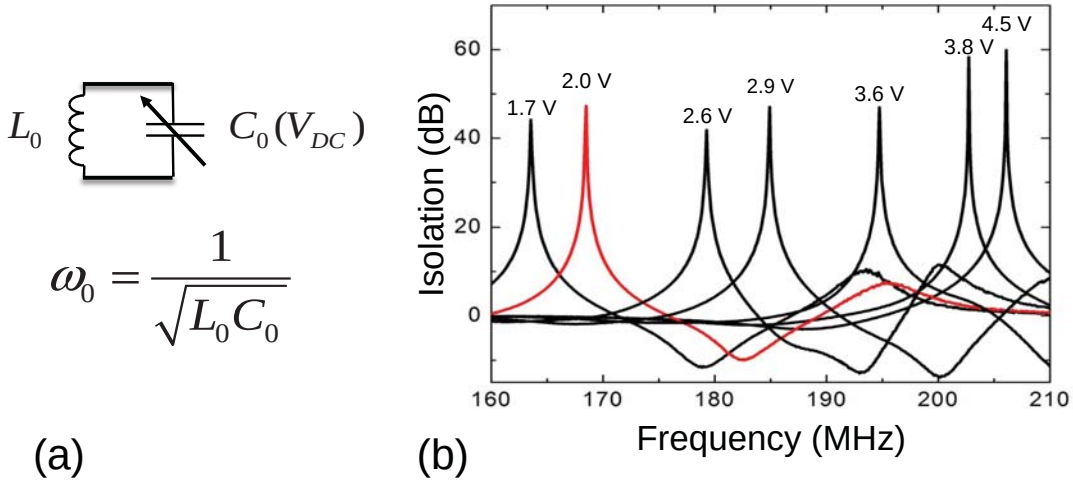

Figure 68: Response versus static voltage [75]. (a) Changing L-C resonator due to applied bias and (b) measured isolation in logarithmic scale versus frequency for different values of V_{dc}. In all cases, V_m is selected, based on our theory, so that isolation at resonance is maximum.

Fig. 68(b) shows the measured isolation versus frequency for the lumped element circulator of Fig. 43, for V_{dc} varied between 1.73 V and 4.5 V. The non-reciprocal

response of the device can be efficiently tuned between 150 MHz and 210 MHz, corresponding to a relative bandwidth of over 30%. Across all this range, our measured isolation is above 40 dB. This strong tuning capability is an additional advantage of the proposed device compared to conventional magnetic-based microwave circulators, and it may be exploited in scenarios requiring dynamic tuning to balance changes in temperature or in the environment. The electronic spin applied to the proposed coupled-resonator loop realizes the equivalent of a dynamically tunable, strongly biased ferromagnetic metamaterial substrate.

5.2 CHIRP TRACKING WITH ANGULAR-MOMENTUM-BIASED CIRCULATORS

Due to the electrical tunability of the presented angular-momentum-biased circulator, it is an ideal circuit for RADAR systems. Certain RADAR applications, such as automotive Doppler [82], use a transient waveform that increases in frequency though the duration of the pulse, also known as a chirp [83]. The chirp time domain waveform, along with the spectrogram, are shown in Fig. 69. This type of waveform is used as a pulse compression technique, which increases range resolution while improving the signal to noise ratio [84]. Current chirp systems use conventional ferromagnetic circulators, where isolation ranges between 10 to 20 dB throughout the chirp frequency spectrum [85]. In order to demonstrate the principle operation in this environment, a lumped-element AM circulator, similar to Fig. 54, was designed for the VHF band (f_0 ~ 255 MHz, f_m ~ 67 MHz), which included the anti-series topology described in Section 4.4.

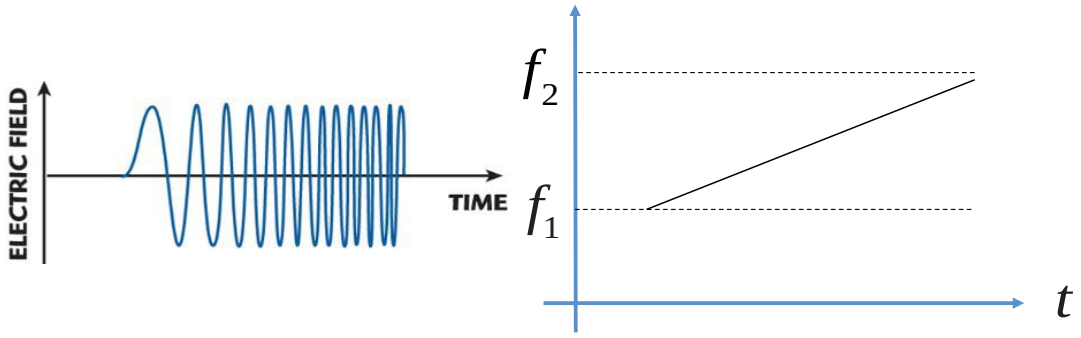

Figure 69: Chirp waveform commonly found in RADAR and Doppler applications. The frequency of the waveform increases/decreases with time, which is advantageous for determining distance and speed of a target.

In order to evaluate the circulator in this transient domain, we must make minor additions to the circuit. In the time domain, the isolated signal port will be comprised of all frequency content, to include the inter-modulation products. In order to reduce the effects of these signals, we must incorporate additional filters to the circulator. In addition to a multi-stage Chebyshev band-pass filter [23], one may apply two cascaded diplexers. A diplexer is a reciprocal filter, with separates signals though low and high pass filters. Here, we cascade two diplexers, where each is tuned to maximize isolation of both inter-modulation signals ($f_0 \pm f_m$) while allowing the main band to propagate unimpeded (f_0).

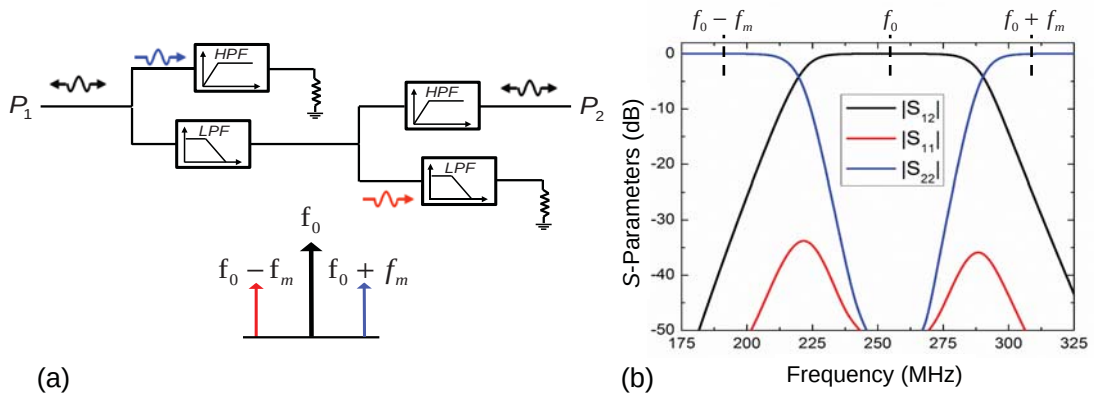

Figure 70: Cascaded diplexers. (a) Electrical schematic illustrating the isolation of the inter-modulation products while allowing propagation of the main band and (b) scattering parameters for the Chirp simulation.

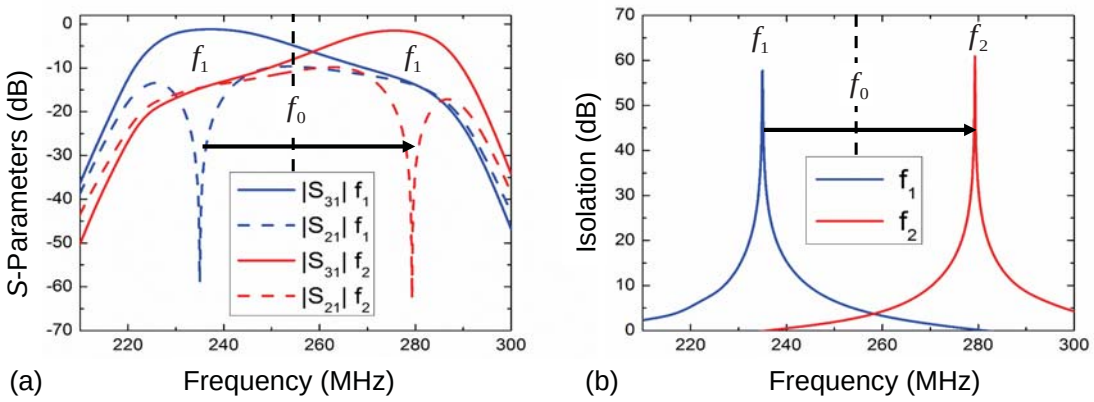

Figure 71: Circulator performance at the boundary of the chirp waveform. (a) Scattering parameters and (b) isolation at f_1 (235 MHz) and f_2 (281 MHz).

Fig. 70 illustrates the diplexer design, along with the scattering response. Here, we used the ADS filter designer, which automates the Butterworth multi-stage low and pass filters. It is designed for the 3dB rolloff to occur halfway between the center

frequency and the inter-modulation products. Based on the center band (f_0), the device provides roughly 30 dB of isolation for the two inter-modulation bands. It should be noted that there is a tradeoff between the level of inter-modulation isolation and the dynamic range in tunability, which will be presented shortly.

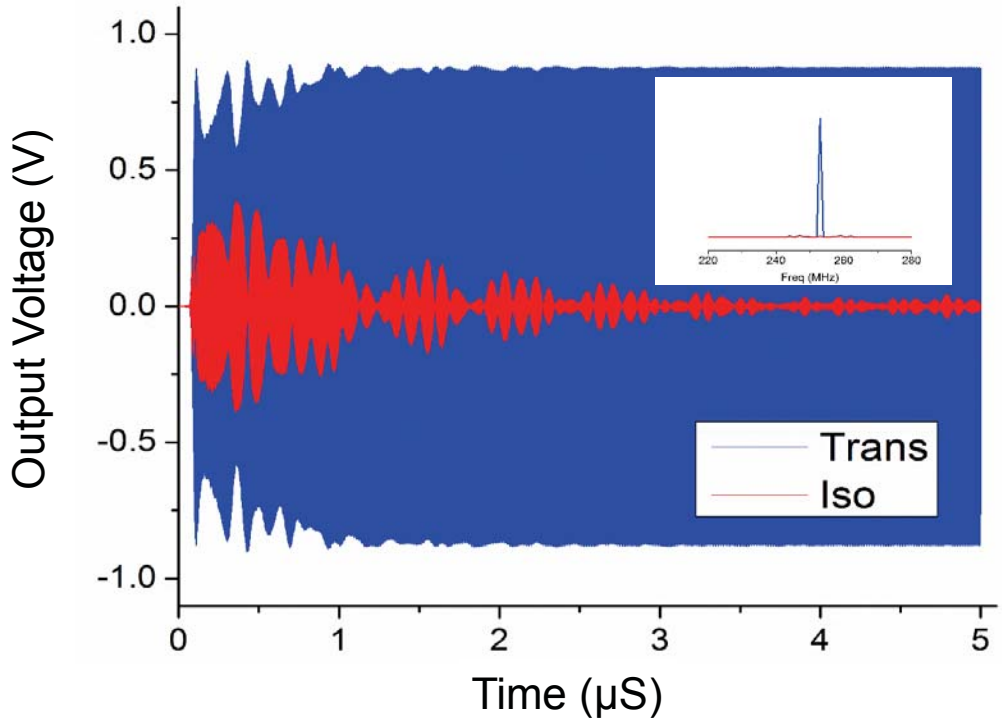

Figure 72: Time domain simulation of circulator at the center of the operational band ($f_0 \sim 255$ MHz). Here the conditions are: $V_{DC} = 9.5$ V, $V_m = 7.7$ V. The Fourier transform is shown in the inset.

Before progressing to a scenario with a chirp waveform, it is beneficial to investigate the performance at the boundaries for the time harmonic case, i.e., isolation at f_1 and f_2 in the steady state. As seen in Fig. 71, the circulator provides significant isolation; over 50 dB at 235 and 280 MHz. For these conditions, merely the biasing (V_{DC}

= 7 to 12.5 V) and modulation amplitude (V_m = 6 to 10 V) were altered. As seen in Fig. 71(a), the scattering response is asymmetric on the exterior side-band (lower frequency for f_1 and higher for f_2) for both operating points. This is due to the close operation at the roll-off of the diplexers (seen in Fig. 70), which limits the spectrum of tunability for the circulator. We will use these operating points as the range for the following chirp demonstration, which corresponds to a normalized range of approximately 20%. An example of the time domain simulation at the center of the band (f_0 ~ 255 MHz) is shown in Fig. 72, with the Fourier transform shown in the inset.

For signal transition between the boundary of f_1 and f_2, we must alter the circulator control signals. Here, we assign a sequence window of 10 μs. The modulation and carrier signals may then be represented as,

$$\begin{aligned} V_{rf} &= V_{rf}^0 \sin\left(2\pi f_1 t + \frac{1}{2}k_{rf}t^2 + \phi_{rf}\right), \\ V_m &= \left(V_m^0 + k_m t\right)\sin\left(2\pi f_m t + \phi_m\right) \end{aligned} \tag{5.2.1}$$

where V_{rf}^0 $\left(V_m^0\right)$ is the starting amplitude, k_{rf} $\left(k_m\right)$ is the chirp (modulation) rate, and ϕ_{rf} $\left(\phi_m\right)$ is the phase offset. The phase offset for the modulation will be 0˚, 120˚ and 240˚ for each of the three sources, as described in the experimental demonstration. The modulation rate, as opposed to the chirp rate, is for the growth in the modulation amplitude and not an increase in oscillation over time. The modulation frequency remains constant during the course of the chirp pulse. The representation of the control signals can be found in Fig. 73. The chirp input pulse, with a chirp rate of 39 MHz/μs, is shown in the time and frequency domain (Figs. 73(a) and (b)). The DC biasing is a smooth step function, rising from 7.2 to 12.5 V in 10 μs. The modulation signal (f_m ~ 67

MHz) increases from 6.2 to 10 V in the same interval. These sources were selected based on the optimum operating conditions for isolation, as seen in Fig. 71.

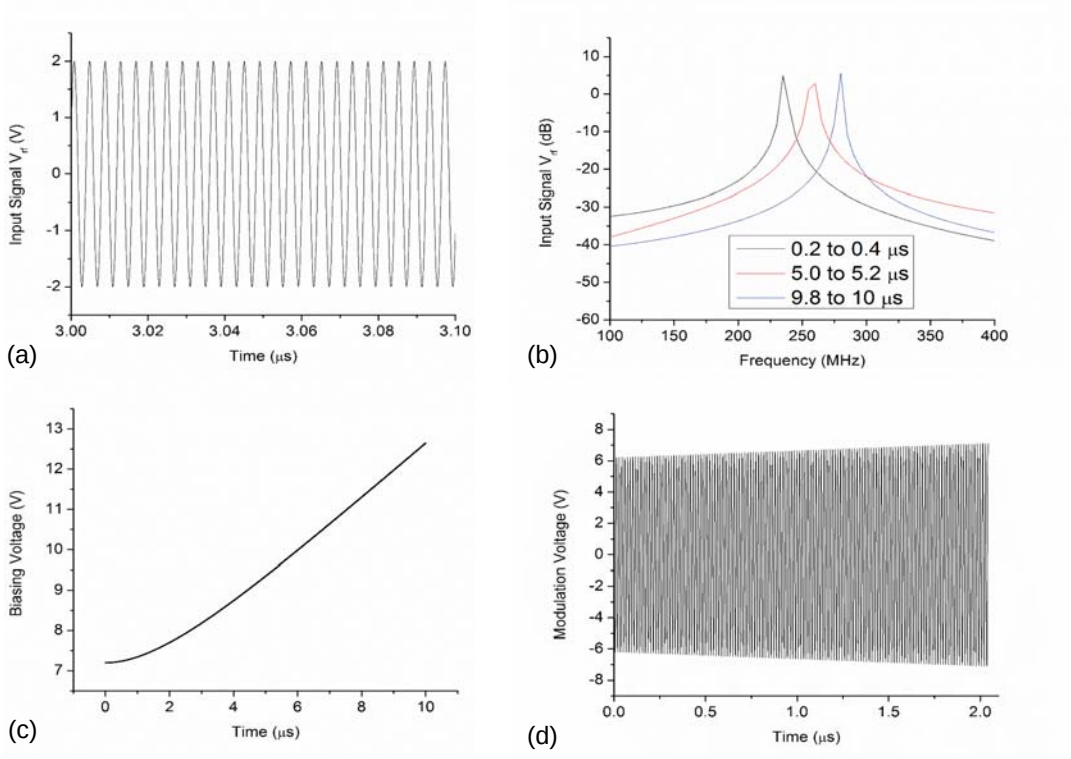

Figure 73: Circulator control signals for chirp scenario. (a) Time domain and (b) Fourier transform of the input chirp signal, illustrating the increasing oscillations in time. (c) DC biasing and (d) modulation signals. The modulation signal increases in time, from 6.2 to 10 V (partial time sequence shown).

With the control signals shown in Fig. 73, we are able to maintain significant isolation throughout the time window, validating isolation from f_1 to f_2. The time domain voltage output for the transmission (blue trace) and isolation (red trace) ports is shown in Fig. 74. The Fourier transform at different time intervals is shown in Fig. 75. Fig. 75(a) is the transmission port, and demonstrates a strong output signal that follows the chirp rate,

as expected. The isolated port, shown in Fig. 75(b), also follows the chirp change in time, but at much lower power levels. The results show that the circulator provides more than 20 dB isolation throughout the pulse interval. Here, we also see leakage of the inter-modulation products, when they are within the passband of the cascaded diplexers. In order to avoid these signals, one must increase the rate of attenuation, or rolloff, which will reduce the range of tunability. Other filter networks may be incorporated, which could eliminate the inter-modulation signals without limiting the range of circulator operation.

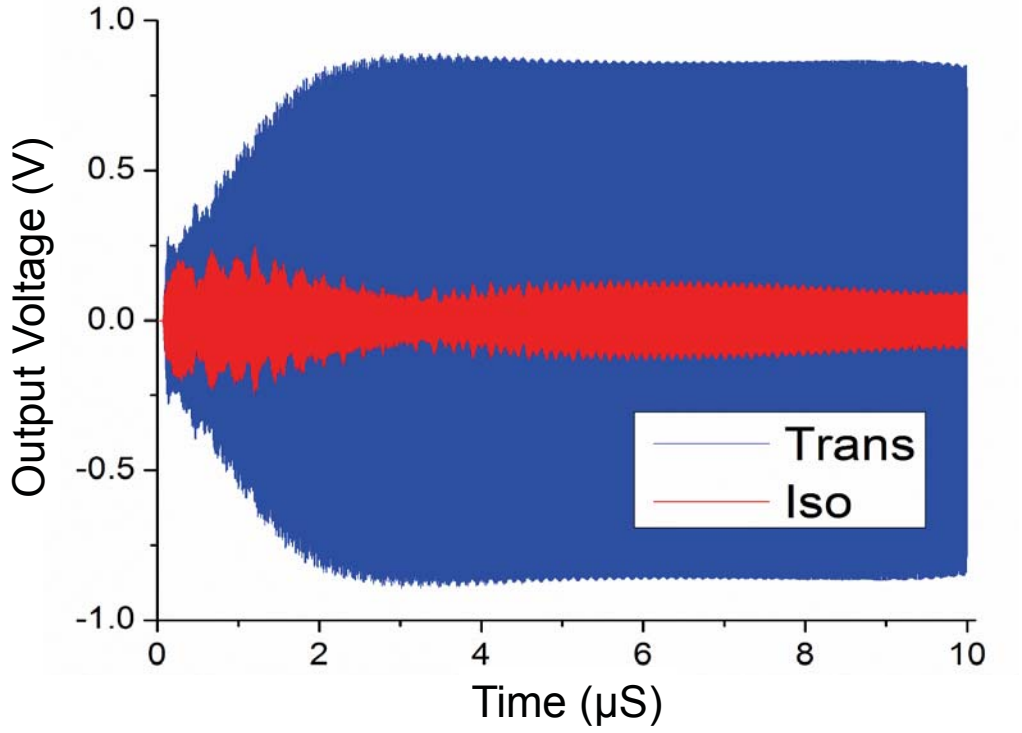

Figure 74: Transient response for angular-momentum-biased circulator to chirp pulse. Control signals based on Fig. 73.

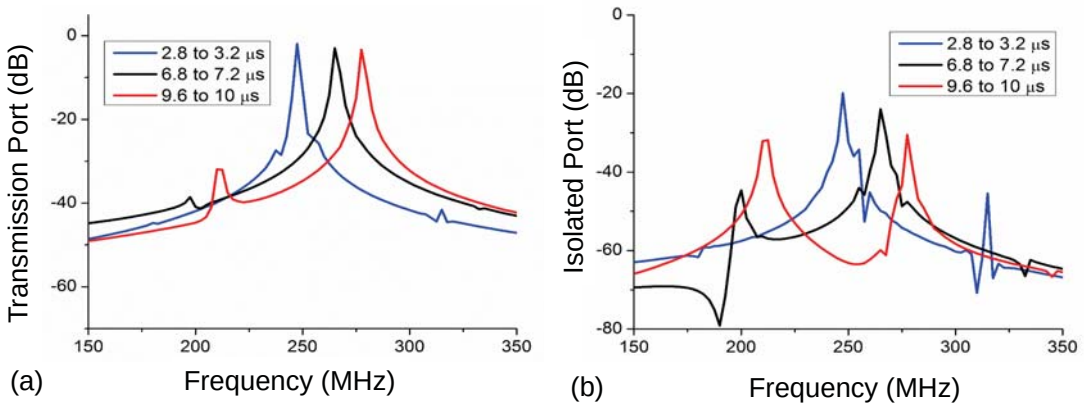

Figure 75: Fourier transform of time domain signal in Fig. 74. This simulation demonstrates the circulator's ability to track a chirp pulse, providing over 20 dB of isolation throughout.

Note that this simulation is not optimized to take advantage of the angular-momentum's instantaneous tunability, but merely an extrapolation of the control parameters at the boundary, as shown in Fig. 73. A more appropriate solution would be a more extensive calibration of the control signals, at many frequency points within the tunable range. While this is more challenging from a simulation perspective, a calibration table would allow for optimization of isolation as the circulator tracks the chirp pulse.

These simulations show that the angular-momentum-biased circulator is able to track a time variant, oscillating signal. However, a RADAR system based on chirp pulse compression functions by analyzing the delay in the transmit and backscatter chirp signals. The change in frequency between these two pulses, which are functions of the backscattering object distance and the chirp rate, must be simultaneously processed by the circulator, regardless of technology (ferrite or angular-momentum-biased). Therefore, the operation of the angular-momentum-biased circulator in these RADAR systems may

be restricted to round trip delays that are within the instantaneous operating band of the circulator. The tunability of the circulator may be utilized for given operating regions, where the maximum delay is still within the instantaneous operating region.

Chapter 6 Conclusions and Future Work

In this dissertation, we introduced two general concepts based on microwave metamaterials that can drastically improve the performance and reduce the dimensions of current devices aimed at microwave generation, detection, and isolation. First, we presented the analysis of an NIMW constructed of stacked, patterned parallel plates based on a TL model. The periodic structure supports a TM NI band, due to the effects of the loading resonators and confinement of the TM mode below cut-off. We developed a homogenized metamaterial model that predicts negative permittivity and permeability, as well as a non-zero magneto-electric coupling coefficient within the NI propagation band. The developed TL model accurately describes the propagation properties of this NI mode and can be used to demonstrate the generation of a bandpass, typical of NI materials, to properly describe the mutual coupling in the metamaterial, and to provide circuital insights into its behavior for optimization and design purposes. Next, we analyzed how a small modification in the unit cell can suppress the bi-anisotropy while maintaining the NI mode of interest, realizing a low-permeability metamaterial. Finally, we discussed the optimal configuration for the excitation of this metamaterial from free-space. We believe that these results may open important venues in the design, optimization and realization of metamaterials for high-power, electron-beam applications, as well as active metamaterial technology.

Then, we investigated the concept of spatiotemporally modulated coupled resonator networks for the realization of magnet-less microwave circulators. A rigorous analytical model was developed, through which the exact condition for obtaining infinite isolation was derived. The derived model, validated with numerical simulations, allows

determining in closed form the required modulation parameters for given lossy Q-factor, desired insertion loss and intermodulation products. Achieving low insertion loss generally requires large modulation parameters, while low intermodulation products can be achieved by increasing only the modulation frequency, irrespective of the modulation amplitude. Based on the analytical model, two circulators were designed for VHF and wireless communications bands. Both designs were based on wye resonators, which were shown to be easier to realize and lead to better performance than ring resonators. Lumped and distributed elements were used for the low- and high-frequency designs, respectively. Both designs exhibit remarkable performance in terms of insertion loss and isolation, very close to commercial standards for magnetic circulators. In addition to obvious advantages in terms of cost, weight and size reduction, an important advantage of the proposed magnet-less circulators is their tunability and noise performance. Power handling is limited by the varactors through which modulation is achieved, but it can be improved by either increasing the DC bias of the varactors or using more advanced varactor configurations. The proposed designs offer a large degree of flexibility in the selection of the modulation frequency, which can be made substantially lower than the signal frequency, significantly simplifying the design of the modulation networks. However, the modulation frequency should not be very low, in order to achieve enough distance between the input and intermodulation frequencies, which is important for the efficient rejection of intermodulation products using suitable filters. The research to-date constitute an important step towards the realization of integrated circulators, which may allow achieving full-duplex operation in wireless communications systems. We also point out that the proposed designs are well suited to push these concepts to very low and very

high frequencies, up to ranges in which magnetic circulators are not practical, respectively for the lumped and distributed-element designs. We also envision the realization of the proposed rotating modulation of coupled-resonator loops in photonic crystal technology, for which high-Q-factor coupled cavities may be implemented and efficiently modulated. Our research also represents a new demonstration of the exciting possibilities offered by dynamic modulation of coupled-resonator networks, with unique control over the flow of light, in the context of recently presented concepts of photonic topological edge states and effective magnetic field for photons.

Angular-momentum-biasing and reverse Cherenkov radiation concepts may be independently utilized, but for specific circumstances, they may coalesce into a single, microwave system. Consider a coherent microwave generator, complete with source, energy extraction ports, waveguides, and finally an antenna. We may replace a conventional source, such as a magnetron, with NI structure tailored for reverse Cherenkov radiation, similar to backward wave oscillators (BWOs). Once the wave energy is extracted, a non-reciprocal device is always present to protect the source from reflected energy. Generally, the isolator or circulator is in the form of a magnetically biased ferromagnetic waveguide. Here, one may replace this component with a magnet-less angular-momentum-biased device, reducing cost while limiting the constraints of ferromagnetic materials. One important limitation of conventional magnetic-based circulators is power handling, which is inherently limited. Waveguide-based angular-momentum-biased isolators may be able to handle significantly larger power levels than in ferrite materials, opening an ideal venue for the implementation and integration of the two concepts put forward in this work.

References

[1] R.A. Shelby, D.R. Smith, and S. Schultz, "Experimental verification of a negative index of refraction", *Science*, vol. 292, no. 5514, pp. 77–79, 2001.

[2] A.K. Iyer, P.C. Kremer, and G.V. Eleftheriades, "Experimental and theoretical verification of focusing in a large, periodically loaded transmission line negative refractive index mertamaterial". *Optics Express*, vol. 11, no. 7, pp. 696-708, 2003.

[3] G. Eleftheriades, A.K. Iyer, and P.C. Kremer, "Planar negative refractive index media using periodically L-C loaded transmission lines", *IEEE Trans. on Microwave Theory and Tech*., vol. 50, no. 12, pp. 2702–2712, 2002.

[4] T. Ueda, A. Lai, and T. Itoh, "Demonstration of Negative Refraction in a Cutoff Parallel-Plate Waveguide Loaded With 2-D Square Lattice of Dielectric Resonators", *IEEE Trans. on Microwave Theory and Tech*., vol. 55, no. 6, pp. 1280–1287, 2007.

[5] V.G. Veselago, "The Electrodynamics of Substances with Simultaneously Negative Values of ε and μ", *Soviet Physics Uspekhi*, vol. 10, no. 4, pp. 509-514, 1968.

[6] J.B. Pendry, "Negative refraction makes a perfect lens", *Physical Review Letters* vol. 85, no. 18, pp. 3966–3969, 2000.

[7] I.M. Ehrenberg, S.E. Sarma, and B. Wu, "A three-dimensional self-supporting low loss microwave lens with a negative refractive index", *Journal of Applied Physics*, vol. 112, pp. 073114, 2012.

[8] T. Itoh, "Metamaterial-Based Antennas", *Proceedings of the IEEE*, vol. 100, no. 7, pp. 2271–2285, 2012.

[9] J.B. Pendry, D. Schurig, and D.R. Smith, "Controlling electromagnetic fields", *Science*, vol. 312, no. 5781, pp. 1780–1782, 2006.

[10] A. Alù, and N. Engheta, "Achieving transparency with plasmonic and metamaterial coatings", *Physical Review E*, vol. 72, no. 1, pp. 016623, 2005.

[11] D. Smith, W. Padilla, D. Vier, S. Nemat-Nasser, and S. Schultz, "Composite medium with simultaneously negative permeability and permittivity", *Physical Review Letters*, vol. 84, no. 18, pp. 4184–4187, 2000.

[12] R. Marqués, J. Martel, F. Mesa, and F. Medina, "Left-Handed-Media Simulation and Transmission of EM Waves in Subwavelength Split-Ring-Resonator-Loaded Metallic Waveguides", *Physical Review Letters*, vol. 89, no. 18, pp. 183901, 20012.

[13] R. Marqués, J. Martel, F. Mesa, and F. Medina, "A new 2D isotropic left-handed metamaterial design: Theory and experiment", *Microwave and Optical Technology Letters*, vol. 35, no. 5, pp. 405–408, 2002.

[14] N. Engheta, "An idea for thin subwavelength cavity resonators using metamaterials with negative permittivity and permeability", *IEEE Antennas and Wireless Propagation Letters*, vol. 1, no. 1, pp. 10–13, 2002.

[15] H. Chen, and M. Chen, "Flipping photons backward: reversed Cherenkov radiation", *Materials Today*, vol. 14, no. 1–2, pp. 34–41, 2011.

[16] J. Baena, J. Bonache, F. Martin, R.M. Sillero, F. Falcone, T. Lopetegi, M. Laso, J. Garcia-Garcia, I. Gil, M.F. Portillo, and M. Sorolla, "Equivalent-circuit models for split-ring resonators and complementary split-ring resonators coupled to planar transmission lines", *IEEE Transactions on Microwave Theory and Techniques*, vol. 53, no. 4, pp. 1451–1461, 2005.

[17] M. Beruete, M. Aznabet, M. Navarro-Cía, O. El Mrabet, F. Falcone, N. Aknin, M. Essaaidi, and M. Sorolla, "Electroinductive waves role in left-handed stacked complementary split rings resonators", *Optics Express*, vol. 17, no. 3, pp. 1274–1281, 2009.

[18] M. Shapiro, S. Trendafilov, Y. Urzhumov, A. Alù, R. Temkin, and G., "Active negative-index metamaterial powered by an electron beam", *Physical Review B*, vol. 86, no. 8, pp. 085132, 2012.

[19] F. Falcone, T. Lopetegi, M. Laso, J. Baena, J. Bonache, M. Beruete, R. Marqués, F. Martín, and M. Sorolla, "Babinet Principle Applied to the Design of Metasurfaces and Metamaterials", *Physical Review Letters*, vol. 93, no. 19, pp. 197401, 2004.

[20] A. Alù and N. Engheta, "Optical nanotransmission lines: synthesis of planar left-handed metamaterials in the infrared and visible regimes*", Journal of the Optical Society of America B*, vol. 23, no. 3, pp. 571, 2006.

[21] R. Marqués, F. Medina, and R. Rafii-El-Idrissi, "Role of bianisotropy in negative permeability and left-handed metamaterials", *Physical Review B*, vol. 65, no. 14, pp. 144440, 2002.

[22] Z. Li, K. Aydin, and E. Ozbay, "Determination of the effective constitutive parameters of bianisotropic metamaterials from reflection and transmission coefficients", *Physical Review E*, vol. 79, no. 2, pp. 026610, 2009.

[23] D.M. Pozar, *Microwave Engineering*. John Wiley & Sons: 2005.

[24] S. Hong, J. Brand, J. I. Choi, M. Jain, J. Mehlman, S. Katti, andP. Levis, "Applications of Self-Interference Cancellation in 5G and Beyond", *IEEE C.M.*, vol. 52, no. 2, pp. 114-121, 2014.

[25] L. Onsager, "Reciprocal relations in irreversible processes. I.," *Phys. Rev.*, vol. 37, pp. 405-426, 1931.

[26] H.B.G. Casimir, "On Onsager's principle of microscopic reversibility," *Rev. Mod. Phys.,* vol. 17, no. 6, pp. 343-350, 1945.

[27] H.B.G. Casimir, "Reciprocity theorems and irreversible processes," *Proc. IEEE*, vol. 51, no. 11, pp. 1570-1573, 1963.

[28] B. Lax and K. J. Button, *Microwave Ferrites and Ferrimagnetics*. McGraw-Hill, 1962.

[29] N. A. Estep, D. L. Sounas, and A. Alù, "Magnet-less microwave circulators based on spatiotemporally-modulated rings of coupled resonators", *Under Review.*

[30] S. Tanaka, N. Shimimura, and K. Ohtake, K., "Active circulators - The realization of circulators usings transistors," *Proc. IEEE*, vol. 53, no. 3, pp. 260-267, 1965.

[31] Y. Ayasli, "Field effect transistor circulators," *IEEE Trans. Magn.*, vol. 25, no. 5, pp. 3242-3247, 1989.

[32] T. Kodera, D. L. Sounas, and C. Caloz, "Artificial Faraday rotation using a ring metamaterial structure without static magnetic field", *Appl. Phys. Lett.*, vol. 99, pp. 03114, 2011.

[33] D. L. Sounas, T. Kodera, and C. Caloz, "Electromagnetic modeling of a magnetless nonreciprocal gyrotropic metasurface", *IEEE Trans. Antennas Propagation*, vol. 61, no. 1, pp. 221-231, 2013.

[34] T. Kodera, D. L. Sounas, and C. Caloz, "Magnetless Nonreciprocal Metamaterial (MNM) technology: Application to microwave components", *IEEE Trans. Microwave Theory and Technology*, vol. 61, no. 3, pp. 1030-1042, 2013.

[35] Z. Wang, Z. Wang, J. Wang, B. Zhang, J. Huangfu, J. D. Joannopoulos, M. Soljačić, and L. Ran, ""Gyrotropic response in the absence of a bias field", *Proc. Natl. Acad. Sci. U.S.A*., vol. 109, no. 33, pp. 13194-13197, 2012.

[36] B.-I. Popa and S. A. Cummer, "Nonreciprocal active metamaterials," *Phys. Rev. B*, vol. 85, pp. 205101, 2012.

[37] K. Gallo and G. Assanto, "All-optical diode in a periodically poled lithium niobate waveguide", *Appl. Phys. Lett*., vol. 79, no. 3, pp. 314-316, 2001.

[38] S. Manipatruni, J. T. Robinson, and M. Lipson, "Optical nonreciprocity in optomechanical structures", *Phys. Rev. Lett.*, vol. 102, pp. 213903, 2009.

[39] L. Fan, J. Wang, L. T. Varghese, H. Shen, B. Niu, Y. Xuan, A. M. Weiner, and Q. Minghao, "An all-silicon passive optical diode", *Science*, vol. 335, pp. 447-450, 2012.

[40] B. Peng, Ş. K. Özdemir, F. Lei, F. Monifi, M. Gianfreda, G. L. Long, S. Fan, F. Nori, C.M. Bender, and L. Yang, "Parity-time-symmetric whispering-gallery microcavities", *Nature Physics*, vol. 10, pp. 394-398, 2014.

[41] Z. Yu and S. Fan, "Complete optical isolation created by indirect interband photonic transitions", *Nature Photon*., vol. 3, pp. 91-94, 2009.

[42] M. S. Kang, A. Butsch, and P. St. J. Russell, "Reconfigurable light-driven opto-acoustic isolaters in photonic crystal fibre", *Nature Photon*., vol. 5, pp. 549-553, 2011.

[43] X. Huang and S. Fan, "Complete all-optical silica fiber isolator via stimulated Brillouin scattering", *J. Lightwave Technol*., vol. 29, no. 15, pp. 2267-2275, 2011.

[44] H. Lira, Z. Yu, S. Fan, and M. Lipson, "Electrically driven nonreciprocity induced by interband photonic transition on a silicon chip", *Phys. Rev. Lett*., vol. 109, pp. 033901, 2012.

[45] K. Fang, Z. Yu, and S. Fan, "Photonic Aharonov-Bohm effect based on dynamic modulation", *Phys. Rev. Lett*., vol. 108, pp. 153901, 2012.

[46] D.-W. Wang, H.-T. Zhou, M.-J. Guo, J.-X. Zhang, J. Evers, and S.-Y. Zhu, "Optical diode made from a moving photonic crystal", *Phys. Rev. Lett.*, vol. 110, pp. 093901, 2013.

[47] I. K. Hwang, S. H. Yun, and B. Y. Kim, "All-fiber-optic nonreciprocal modulator", *Opt. Lett.*, vol. 22, no. 8, pp. 507-509, 1997.

[48] C. R. Doerr, N. Dupuis, and L. Zhang, "Optical isolator using two tandem phase modulators", *Opt. Lett.*, vol. 36, no. 21, 2011.

[49] C. Galland, R. Ding, N. C. Harris, T. Baehr-Jones, and M. Hochberg, "Broadband on-chip optical non-reciprocity using phase modulators", *Opt. Express*, vol. 21, no. 12, pp. 14500-14511, 2013.

[50] S. Qin, Q. Xu, and Y. E. Wang, "Nonreciprocal components with distributedly modulated capacitors", *IEEE Trans. Micro. Theory Techn*., vol. 62, no. 10, pp. 2260-2272, 2014.

[51] D. L. Sounas, C. Caloz, and A. Alù, "Giant non-reciprocity at the subwavelength scale using angular momentum-biased metamaterials", *Nat. Commun*., vol. 4, pp. 2407, 2013.

[52] R. Fleury, D. L. Sounas, C. F. Sieck, M. R. Haberman, and A. Alù, "Sound isolation and giant linear nonreciprocity in a compact acoustic circulator", *Science*, vol. 343, pp. 516-519, 2014.

[53] N.A. Estep, A.N. Askarpour, S. Trendafilov, G. Shvets, and A. Alù, "Transmission-Line Model and Propagation in a Negative-Index, Parallel-Plate Metamaterial to Boost Electron-Beam Interaction", *IEEE Trans. on Antennas and Propagation*, vol. 62, no. 6, pp. 3212-3221, 2014.

[54] X. Chen, T. Grzegorczyk, B. Wu, J. Pacheco, and J. Kong, "Robust method to retrieve the constitutive effective parameters of metamaterials", *Physical Review E*, vol. 70, no. 1, pp. 016608, 2004.

[55] A. Alù, F. Bilotti, and L. Vegni, "Analysis of L–L transmission line metamaterials with coupled inductances", *Microwave and Optical Technology Letters*, vol. 49, no. 1, pp. 94–97, 2007.

[56] A.K. Iyer and G.V. Eleftheriades, "Volumetric layered transmission-line metamaterial exhibiting a negative refractive index", *Journal of the Optical Society of America B*, vol. 23, no. 3, pp. 553, 2006.

[57] A. Alu and N. Engheta, "Pairing an epsilon-negative slab with a mu-negative slab: Resonance, tunneling and transparency", *IEEE Transactions on Antennas and Propagation*, vol. 51, no. 10, pp. 2558–2571, 2003.

[58] C. Caloz and T.Itoh, *Electromagnetic Metamaterials: Transmission Lines Theory and Microwave Applications*, John Wiley and Sons: 2005.

[59] L. Solymar and E. Shamonina, *Waves in Metamaterials*, Oxford University Press: 2009.

[60] R. Marqués, F. Martin, and M. Sorolla, *Metamaterials with Negative Parameters*, John Wiley and Sons: 2008.

[61] N.A. Estep, A.N. Askarpour, and A. Alù, "Design and Operation of a Negative-Index Parallel-Plate Metamaterial", *7th International Metamaterials Conference,* Bordeaux, France, 2013.

[62] R. S. Elliott, *Electromagnetics*, IEEE Press: 1993.

[63] S. Chaimool, C. Rakluea, and P. Akkaraekthalin, "Mu-near-zero metasurface for microstrip-fed slot antennas", *Applied Physics A,* vol. 112, no. 3, pp. 669-675, 2013.

[64] A.A. Lagarkov, A.N. Semenenko, V.N. Chistyaev, V.A. Krasnolobov, and I.I. Basharin, "Mu and epsilon-near-zero metamaterial-assisted horn antenna", *Proceedings of the Fourth European Conference on Antennas and Propagation (EuCAP)*, pp. 1–5, 2010.

[65] N.A. Estep, A.N. Askarpour, and A. Alù, "Experimental Demonstration of Negative-Index Propagation in a Rectangular Waveguide Loaded with Complementary Split-Ring Resonators", *IEEE Ant. And Wireless Propagation Lett.*, vol. 14, no. 6, pp. 119-122, 2015.

[66] P.M. Bellan, *Fundamentals of Plasma Physics*, Cambridge University Press: 2006.

[67] D. L. Sounas and A. Alù, "Angular-momentum-biased nanorings to realize magnetic-free integrated optical isolation", *ACS Photonics*, vol. 1, pp. 198-201, 2014.

[68] M. Soljačić, C. Luo, J.D. Joannopoulos,ans S. Fan, "Nonlinear photonic crystal microdevices for optical integration", *Opt. Lett.,* vol. 28, pp. 637, 2003.

[69] I.V. Shadrivov, V.A. Fedotov, D.A. Powell, Y.S. Kivshar, and N.I. Zheludev, "Electromagnetic Wave Analogue of an Electronic Diode", *New Journal of Physics*, vol. 13, pp. 033025, 2011.

[70] M. Hafezi and P. Rabl, "Optomechanically Induced Non-reciprocity in Microring Resonators", *Opt. Express,* vol. 20, pp. 7672-7684, 2012.

[71] C.G. Poulton, "Design for Broadband On-chip Isolater Using Stimulated Brillouin Scattering in Dispersion-Engineered Chalcogenide Waveguides", *Opt. Express,* vol. 20, pp. 21235-21246, 2012.

[72] A. Kamal, J. Clarke, and M.H. Devoret, "Noiseless Non-reciprocity in a Parametric Active Device", *Nature Physics,* vol. 7, pp. 311-315, 2011.

[73] Q. Xu, B. Schmidt, S. Pradhan, and M. Lipson, "Micrometer-scale Silicon Electro-optic Modulator", *Nature,* vol. 435, pp. 325-327, 2005.

[74] Q. Xu, S. Manipatruni, B. Schmidt, J. Shakya and M. Lipson, "12.5 GBits/s Carrier-injection-based Silicon Micro-ring Silicon Modulators", *Optics Express,* vol. 15, pp. 430-436, 2007.

[75] N. A. Estep, D. L. Sounas, J. Soric, and A. Alù, "Magnetic-free non-reciprocity and and isolation based on parametrically modulated coupled-resonator loops", *Nature Physics*, vol. 10, pp. 923-927, 2014.

[76] W. Suh, Z. Wang, and S. Fan, "Temporal coupled-mode theory and the presence of non-orthogonal modes in lossless multimode cavities", *IEEE J. Quant. Electron*., vol. 40, no. 10, pp. 1511-1518, 2004.

[77] D.J. Griffiths, *Introduction to quantum mechanics*, Prentice Hall: 1995.

[78] H. A. Haus and W. Huang, "Coupled-Mode Theory," *Proc. IEEE,* vol. 79, pp. 1505-1518, 1991.

[79] Z. Wang and S. Fan, "Magneto-optical defects in two-dimensional photonic crystals", *App. Phy. B,* vol. 81, pp. 369-375, 2005.

[80] K. Buisman, L. C. N. de Vreede, L. E. Larson, M. Spirito, A. Akhnoukh, T. L. M. Scholtes, and L. K. Nanver, "Distortion-free varactor diode topologies for RF adaptivity," in *Proc. 2005 IEEE MTT-S International Microwave Symposium*, Long Beach, CA, U.S.A., June 12-17, 2005.

[81] K. Buisman, C. Huang, P.J. Zampardi, and L. C. N. de Vreede, "RF Power Insensitive Varactors," *IEEE Microwave and Wireless Comp. Lett.*, vol. 22, no. 8, pp. 418 – 420, 2012.

[82] S. Lutz, D. Ellenrieder, and T. Walter, "On Fast Chirp Modulations and Compressed Sensing for Automotive Radar Applications," *in RADAR Symposium*, 2014.

[83] S.J. Orfanidis, *Electromagnetic Waves and Antennas*, Rutgers University: Piscataway, NJ, 2008.

[84] J. R. Klauder, A. C, Price, S. Darlington and W. J. Albersheim, "The Theory and Design of Chirp Radars," Bell System Technical Journal 39, 745 (1960).

[85] D. Cruickshank and B. Hartnett, 'Selecting Ferrite Circulators for Radar Applications," Skyworks Technical Documents, 2011.

Vita

Capt. Nicholas A. Estep is an active duty officer in the Air Force and is currently a graduate student at the University of Texas at Austin. He is seeking a PhD in electrical engineering, with a focus on electromagnetics. His assignment as a graduate student is sponsored by a government organization in the Washington, D.C. area. Previously, Capt. Estep was the High Power Microwave (HPM) Effects Test Director, HPM Division, Directed Energy Directorate, Air Force Research Laboratory, Kirtland AFB, NM. He was responsible for the planning and execution of electromagnetic and high-energy radiation effects research within the division. Capt. Estep was commissioned in 2006 after graduating from The University of Texas at Austin, with a Bachelor of Science degree in electrical engineering. He has served in diverse technical positions in the field of electromagnetic propagation and effects. He directed the life cycle sustainment planning of the Joint Threat Emitter (JTE) from 2006-2008, a joint service aircrew training system valued at $500 M. Capt. Estep holds a master's degree in electrical engineering from the Air Force Institute of Technology (AFIT), with a focus of antenna analysis and electromagnetic and radiation effects on electronics.

This dissertation was typed by Nicholas Aaron Estep.

Author may be reached at NAEstep@utexas.edu.